

2008

# Investigations of the $R_5(\text{Si}_x\text{Ge}_{1-x})_4$ intermetallic compounds by X-ray resonant magnetic scattering

Lizhi Tan  
*Iowa State University*

Follow this and additional works at: <http://lib.dr.iastate.edu/rtd>

 Part of the [Condensed Matter Physics Commons](#)

---

## Recommended Citation

Tan, Lizhi, "Investigations of the  $R_5(\text{Si}_x\text{Ge}_{1-x})_4$  intermetallic compounds by X-ray resonant magnetic scattering" (2008). *Retrospective Theses and Dissertations*. 15734.  
<http://lib.dr.iastate.edu/rtd/15734>

This Dissertation is brought to you for free and open access by Iowa State University Digital Repository. It has been accepted for inclusion in Retrospective Theses and Dissertations by an authorized administrator of Iowa State University Digital Repository. For more information, please contact [digirep@iastate.edu](mailto:digirep@iastate.edu).

Investigations of the  $R_5(\text{Si}_x\text{Ge}_{1-x})_4$  intermetallic compounds by X-ray  
resonant magnetic scattering

by

Lizhi Tan

A dissertation submitted to the graduate faculty  
in partial fulfillment of the requirements for the degree of  
DOCTOR OF PHILOSOPHY

Major: Condensed Matter Physics

Program of Study Committee:  
Alan I. Goldman, Co-major Professor  
Robert J. McQueeney, Co-major Professor  
Bruce N. Harmon  
Patricia A. Thiel  
Soeren A. Prell

Iowa State University

Ames, Iowa

2008

UMI Number: 3323720

### INFORMATION TO USERS

The quality of this reproduction is dependent upon the quality of the copy submitted. Broken or indistinct print, colored or poor quality illustrations and photographs, print bleed-through, substandard margins, and improper alignment can adversely affect reproduction.

In the unlikely event that the author did not send a complete manuscript and there are missing pages, these will be noted. Also, if unauthorized copyright material had to be removed, a note will indicate the deletion.



---

UMI Microform 3323720  
Copyright 2008 by ProQuest LLC  
All rights reserved. This microform edition is protected against  
unauthorized copying under Title 17, United States Code.

---

ProQuest LLC  
789 East Eisenhower Parkway  
P.O. Box 1346  
Ann Arbor, MI 48106-1346

## TABLE OF CONTENTS

<b>LIST OF TABLES</b> . . . . .	v
<b>LIST OF FIGURES</b> . . . . .	viii
<b>CHAPTER 1. Introduction and Overview of the Work in this Thesis</b>	1
<b>CHAPTER 2. Survey of <math>R_5(Si_xGe_{1-x})_4</math></b> . . . . .	6
Discovery of $Gd_5(Si_xGe_{1-x})_4$ . . . . .	6
Properties of $Gd_5(Si_xGe_{1-x})_4$ . . . . .	8
Magnetocaloric Effect . . . . .	8
Giant Magnetoresistance . . . . .	9
Crystallographic Structures in $R_5(Si_xGe_{1-x})_4$ . . . . .	11
Properties of $Gd_5Ge_4$ . . . . .	16
<b>CHAPTER 3. X-ray Resonant Scattering and Symmetry Analysis</b> . .	23
Overview of X-Ray Scattering Techniques . . . . .	23
Resonant Magnetic Scattering . . . . .	25
Resonant Scattering Amplitude and Polarization Dependence . . . . .	27
Symmetry Analysis . . . . .	32
The Independent Symmetry Elements . . . . .	35
Construction of Irreducible Representations . . . . .	36
Transformation Properties . . . . .	38
Invariants . . . . .	38
Application . . . . .	41

Multiple Diffraction . . . . .	42
Geometry Condition . . . . .	43
An Example from Three-Wave Diffraction . . . . .	43
Azimuth and Wavelength Dependence . . . . .	46
Polarization Factors in Multiple Diffraction . . . . .	48
Application . . . . .	49
<b>CHAPTER 4. The Magnetic Structure of <math>\text{Gd}_5\text{Ge}_4</math> in Zero Field . . .</b>	<b>52</b>
Introduction . . . . .	52
Experimental Details . . . . .	53
Magnetic Structure in Zero Field . . . . .	57
The Unusual Order Parameter in $\text{Gd}_5\text{Ge}_4$ in Zero Field . . . . .	65
Spin Reorientation in $\text{Tb}_5\text{Ge}_4$ in Zero Field . . . . .	66
Spin Reorientation in $\text{Gd}_5\text{Ge}_4$ in Zero Field . . . . .	72
Discussion . . . . .	78
Magnetic Structure of $\text{Gd}_5\text{Si}_{0.33}\text{Ge}_{3.67}$ in Zero Field . . . . .	79
Magnetization . . . . .	80
Magnetic Structure in Zero Field . . . . .	81
Discussion . . . . .	87
<b>CHAPTER 5. Spin-Flop Transition in <math>\text{Gd}_5\text{Ge}_4</math> . . . . .</b>	<b>89</b>
Introduction . . . . .	89
Experimental Details . . . . .	93
Results and Discussion . . . . .	95
Magnetization Measurements . . . . .	96
Magnetic Structure in Zero Field . . . . .	97
Observation of the Spin-Flop Transition . . . . .	99
Magnetic Structure in the Spin-Flop Phase . . . . .	104

Discussion . . . . .	108
Magnetic Anisotropy Related to Antiferromagnetic Order . . . . .	108
Conclusions . . . . .	111
<b>CHAPTER 6. Short-Range Order in <math>\text{Gd}_5\text{Ge}_4</math> . . . . .</b>	<b>113</b>
Magnetization Measurements . . . . .	113
The Estimation of Scattering Intensity from Possible Short-Range Order	114
The XRMS Experiment Setup . . . . .	121
XRMS Results . . . . .	123
<b>CHAPTER 7. Summary . . . . .</b>	<b>129</b>
<b>ACKNOWLEDGEMENTS . . . . .</b>	<b>132</b>
<b>BIBLIOGRAPHY . . . . .</b>	<b>133</b>

## LIST OF TABLES

Table 3.1	$\hat{k}$ and $\hat{k}'$ denote unit vectors in the directions of the primary and secondary photon beams and $\hat{k} \cdot \hat{k}' = \cos\theta$ where $\theta$ is the angle of scattering. The vector $\boldsymbol{\mu}$ is a unit vector, which defines the magnetic quantization axis, and $\mu_{\perp}$ , is the projection of $\boldsymbol{\mu}$ perpendicular to the plane of scattering. Polarization vectors parallel and perpendicular to the plane are denoted by $\boldsymbol{\epsilon}_{\perp}$ and $\boldsymbol{\epsilon}_{\parallel}$ , with $\mu_{\perp} = (\boldsymbol{\epsilon}_{\perp} \cdot \boldsymbol{\mu}) = (\boldsymbol{\epsilon}'_{\perp} \cdot \boldsymbol{\mu})$ . Note $\hat{k} = \boldsymbol{\epsilon}_{\perp} \times \boldsymbol{\epsilon}_{\parallel}$ and a similar relation for the secondary beam. . . . .	31
Table 3.2	Transformation properties of the basis vectors for $8d$ site . . . . .	39
Table 3.3	Transformation properties of the basis vectors . . . . .	39
Table 3.4	The magnetic modes of the $4c$ and $8d$ Wyckoff sites for the 8 possible magnetic space groups of the crystallographic space group $Pnma$ associated with a magnetic unit cell that is the same as the crystallographic unit cell (based on Reference 17 with a modified sequence of the atomic positions according to Reference 18). The basis vectors ( $A, C, F, G$ for a $4c$ site, $A_B, C_B, F_B, G_B, L, P, Q, R$ for an $8d$ site) are characterized by the sign sequence for the magnetic moment components along the three crystallographic axes. . . . .	40

Table 4.1	Magnetic modes for the $4c$ and $8d$ Wyckoff sites, and their corresponding structure factors for the $(h\ 0\ 0)$ , $(0\ k\ 0)$ and $(0\ 0\ l)$ reflections ( $h, k, l$ are odd). $x^{4c}$ , $y^{4c}$ , $z^{4c}$ and $x^{8d}$ , $y^{8d}$ , and $z^{8d}$ are the atomic positions and $\mu_j^{4c}$ and $\mu_j^{8d}$ are the magnetic moment components along the corresponding $j$ -axis ( $j = a, b, c$ ) at the $4c$ site and the $8d$ sites respectively.) . . . . .	61
Table 4.2	The measured and calculated (from Eqn. 4.1) values of the integrated intensity of $(0\ k\ 0)$ reflections at $T = 6$ K. . . . .	63
Table 4.3	Components of the Tb magnetic moments for all of the studied $\text{Tb}_5\text{Ge}_4$ compounds as determined from the Rietveld refinements of the D2B neutron powder diffraction data. (From Table III in Ref. [RMA <sup>+</sup> 02]) . . . . .	72
Table 4.4	The measured and calculated values of the integrated intensity of $\text{Gd}_5\text{Ge}_4$ $(0\ k\ 0)$ reflections at $T = 90$ K. . . . .	77
Table 4.5	<b>c</b> -component of the Gd magnetic moments as determined from $(0\ k\ 0)$ reflections at $T = 6$ K and $T = 90$ K. . . . .	78
Table 4.6	The measured and calculated values of the integrated intensity of $\text{Gd}_5\text{Si}_{0.33}\text{Ge}_{3.67}$ $(0\ k\ 0)$ reflections at $T = 80$ K. . . . .	87
Table 5.1	The measured and calculated values of the integrated intensity of $(0\ k\ 0)$ reflections in $\pi$ - $\pi$ geometry at $T = 9$ K in zero field. The calculated values are based upon the model presented in Ref. [TKK <sup>+</sup> 05] . . . . .	97
Table 5.2	The measured and calculated values of the integrated intensity of $(0\ k\ 0)$ reflections in $\pi$ - $\sigma$ geometry at $T = 9$ K with $H = 10$ kOe. The calculated values are based on the magnetic space group $Pn'm'a'$ . . . . .	105

Table 5.3	The magnetic anisotropy energies for $\text{Gd}_5\text{Ge}_4$ from two different interactions. The calculations were made for AFM components along three crystallographic axes. The moments along <b>a</b> , <b>b</b> , and <b>c</b> correspond to magnetic space groups $Pn'm'a'$ , $Pnma'$ , and $Pnm'a$ , respectively. The moment size is assumed as $7\mu_{\text{B}}/\text{Gd}$ . SO represents the spin-orbit interaction. Y.B. Lee calculated the MAE from SO in 5d bands. . . . .	110
Table 6.1	Estimated intensity for magnetic short-range order using a pyrolytic graphite analyzer. We take $p = 0.5$ . $I_1^{\text{Max}}$ is the magnetic diffuse scattering intensity from the model with magnetic long-range order along two dimensions and short-range order along the other dimension. $I_2^{\text{Max}}$ is the intensity from the model with magnetic long-range order along one dimension and short-range order along the other two dimensions. $I_3^{\text{Max}}$ is the intensity from the model with short-range order along all three dimensions. . .	120
Table 6.2	Estimated intensity for magnetic short-range order using a Ge analyzer. We take $p = 0.5$ . $I_1^{\text{Max}}$ is the magnetic diffuse scattering intensity from the model with magnetic long-range order along two dimensions and short-range order along the other dimension. $I_2^{\text{Max}}$ is the intensity from the model with magnetic long-range order along one dimension and short-range order along the other two dimensions. $I_3^{\text{Max}}$ is the intensity from the model with short-range order along all three dimensions. . . . .	124

## LIST OF FIGURES

- Figure 2.1 Magnetic and crystallographic phase diagram in zero applied magnetic field for  $\text{Gd}_5(\text{Si}_x\text{Ge}_{1-x})_4$  alloys. Spontaneous magnetic ordering temperatures of  $\text{Gd}_5(\text{Si}_x\text{Ge}_{1-x})_4$  compounds are described as functions of silicon concentration,  $x$ . O(I) for  $\text{Gd}_5\text{Si}_4$ -type orthorhombic structure and O(II) for  $\text{Gd}_5\text{Ge}_4$ -type orthorhombic structure. The thick solid lines delineate boundaries of the second order phase transitions, and the thick dash-dotted lines delineate the same for the first order phase transformations. The first order transition line doesn't reach the stoichiometry of  $\text{Gd}_5\text{Ge}_4$ , which represents no AFM-FM transition for  $\text{Gd}_5\text{Ge}_4$ . The Curie temperature of pure Gd metal (thin dashed line) is shown for reference purposes. (From Pecharsky and Gschneidner [PG97d, PG97c, PG98]) . . . . . 7
- Figure 2.2 MCE curves comparing  $\text{Gd}_5\text{Si}_2\text{Ge}_2$  and Gd. (Left)  $\Delta S_m(T, \Delta H = 5 \text{ Tesla})$  curves; and (right)  $\Delta T_{ad}(T, \Delta H = 5 \text{ Tesla})$  curves. The Curie temperatures of 276 and 294 K, respectively, for  $\text{Gd}_5\text{Si}_2\text{Ge}_2$  and Gd are noted on the MCE curves. The figure is taken from Ref. [Mil06]. Data for these curves were taken from Ref. [PG97b] 10

- Figure 2.3 The crystal structure of  $\text{Gd}_5\text{Ge}_4$ . Shaded regions indicate the “slabs” stacked along the  $\mathbf{b}$  direction. The slabs are infinite in the  $ac$  plane but they are limited to  $\sim 7 \text{ \AA}$  along the  $\mathbf{b}$ -axis. It is interesting to note that each slab consists of five monolayers (ABCBA) stacked along the  $\mathbf{b}$ -axis, originally used by Smith et al [SJT67] to describe the crystallography of the  $\text{Sm}_5\text{Ge}_4$ -type structure. . . . . 13
- Figure 2.4 Four different types of layered structures found among  $\text{R}_5\text{T}_4$  compounds: (a) the  $\text{Gd}_5\text{Si}_4$ -type; (b) the  $\text{Gd}_5\text{Si}_2\text{Ge}_2$ -type; (c) the  $\text{Sm}_5\text{Ge}_4$ -type; (d) the  $\text{Tm}_5\text{Si}_2\text{Sb}_2$ -type. See the text for a description of differences and relationships among these four structure types. (From Ref. [PG]) . . . . . 15
- Figure 2.5 The magnetic phase diagram of  $\text{Gd}_5\text{Ge}_4$ , which was constructed from the heat capacity and magnetization data, delineates the phase fields observed in the system during iso-field heating or isothermal magnetizing. The inset shows the magnetization of  $\text{Gd}_5\text{Ge}_4$  cooled in zero magnetic field. During the first magnetic field increase, which is shown by open squares in the inset, a metamagnetic like transition occurs at  $\sim 18 \text{ kOe}$ . During the first magnetic-field reduction (closed circles) and during the second and following magnetic-field increases (opened triangles), the magnetization behavior is typical of a soft ferromagnet. (Taken from Ref. [LPGM01]) . . . . . 19

- Figure 2.6 Schematic representation of the crystallographic and proposed magnetic structures of  $\text{Gd}_5\text{Ge}_4$  in the (a, b) plane at low temperature. Only the Ge atoms participating in the Ge-Ge covalent like bonds are depicted as solid spheres. A solid line linking the Ge atoms represents a formed bond [O(I)], whereas a dashed line is used for a broken one [O(II)]. Gray arrows are used to illustrate the change in the magnetic coupling induced by magnetic field, hydrostatic pressure or temperature. (From Ref. [MAM<sup>+</sup>03]) . . . 21
- Figure 3.1 A schematic view of the XRMS process. Only a few core states are displayed, and the conduction bands are shown without the rich structure that exists in results from a realistic model. The figure shows the states when the core hole electron is excited above the Fermi level. The excitation and decay processes of the core electron happen within the core hole life time ( $\Gamma$ ). The offset in energy between spin up and down states results from the intra-atomic magnetic exchange interaction between  $4f$  and  $5d$  orbitals. . . . . 26
- Figure 3.2 The coordinate system used for the polarization dependence of the resonant scattering amplitudes described in the text.  $\mathbf{k}$  and  $\mathbf{k}'$  are the incident and scattered wave vectors.  $\epsilon_\sigma$  and  $\epsilon_\pi$  are the components of the polarization perpendicular and parallel to the scattering plane. The  $e_2$  axis is perpendicular to the plane of scattering. The  $e_3$  axis is parallel to the scattering vector. . . . 30

- Figure 3.3 Geometry of one specific example of multiple diffraction formed by three wave vectors.  $C$  denotes the center of the Ewald sphere;  $O$  is the origin of reciprocal lattice space.  $G$  and  $L$  are the points on the surface of Ewald sphere.  $\psi$  is azimuthal angle.  $\mathbf{K}_O$ ,  $\mathbf{K}_G$ , and  $\mathbf{K}_L$  stand for incident, primary diffracted and secondary diffracted wave vectors, respectively. When both  $G$  and  $L$  are located on the surface of the Ewald sphere, a third beam diffraction condition is satisfied, for which  $\mathbf{K}_G - \mathbf{K}_L$  is the wave vector. . . . . 45
- Figure 3.4 (a) Contour map of the intensity of  $\text{Gd}_5\text{Ge}_4$  (5 0 0) reflection as a function of energy and azimuth angle  $\psi$  at  $T = 8$  K. Discontinuities in the bands of multiple scattering across the energy range are artifacts from steps in mesh scans and (b) Single energy scan at the azimuth angle  $\psi = 59.9^\circ$ , which is depicted as a horizontal dashed line in (a). In (b), the vertical dashed line represents the position of the Gd  $L_{\text{II}}$  absorption edge. The maximum intensity at  $E = 7.934$  keV is a resonant signal, which is unchanged with the azimuth rotation. . . . . 47
- Figure 3.5 Choice of unit polarization vectors  $\sigma$  and  $\pi$  for symmetrical configuration.  $C$  denotes the center of the Ewald sphere;  $C'$  denotes the center of the optional circle;  $\mathbf{Q}$ ,  $\mathbf{Q}_L$ , and  $\mathbf{Q}_G$  represent scattering vectors. The wave-vectors  $\mathbf{K}_O$ ,  $\mathbf{K}_G$ , and  $\mathbf{K}_L$  lie in a section of Ewald sphere. . . . . 50

Figure 4.1	Magnetic susceptibility $M/H$ of the $\text{Gd}_5\text{Ge}_4$ single crystal. The temperature dependence of the susceptibility was measured on heating of the zero-field cooled sample in a field of 100 Oe applied parallel to the three crystallographic axes. . . . .	54
Figure 4.2	(a) $\theta$ scan through the (0 3 0) magnetic peak at 10 K (filled circles) and 145 K (open circles) and (b) energy scans at 10 K (filled circles) and 145 K (open circles) through the magnetic peak. The data were measured at an azimuth angle of $\psi = 30^\circ$ using aluminum attenuator with 0.41 transmission. The dashed line represents the position of the Gd $L_{\text{II}}$ absorption edge. . . . .	56
Figure 4.3	(a) Integrated intensity of the (0 7 0) magnetic peak measured upon heating the sample, at an azimuth angle of $\psi = 30^\circ$ , using an aluminum attenuator with 0.41 transmission. (b) Integrated intensity of the (5 0 0) resonant peak measured during heating at an azimuth angle of $\psi = 60^\circ$ without attenuator. . . . .	58
Figure 4.4	The integrated intensity of the (0 3 0) magnetic peak normalized by the (0 4 0) charge peak at $T = 8$ K. The solid curve represents the variation expected for magnetic moments along the <b>c</b> -axis. . . . .	60
Figure 4.5	Magnetic susceptibility $M/H$ of the $\text{Tb}_5\text{Ge}_4$ single crystal. The temperature dependence of the susceptibility was measured on heating of the zero-field cooled sample in a field of 1000 Oe applied parallel to the three crystallographic axes. . . . .	67
Figure 4.6	The temperature dependence of the electrical resistivity of the $\text{Tb}_5\text{Ge}_4$ single crystal measured on heating up the sample with a current applied parallel to the <b>b</b> axis. The solid lines are drawn to guide the eyes. . . . .	69

Figure 4.7	Integrated intensity of the (0 7 0) magnetic reflection measured upon heating the Tb <sub>5</sub> Ge <sub>4</sub> sample. . . . .	71
Figure 4.8	The temperature dependence of the electrical resistivity of the Gd <sub>5</sub> Ge <sub>4</sub> single crystal measured on heating up the sample with a current applied parallel to the <b>a</b> axis and <b>b</b> axis respectively. The solid lines are drawn to guide the eyes. . . . .	74
Figure 4.9	Integrated intensity of the (0 10 -1) magnetic reflection measured upon heating the Gd <sub>5</sub> Ge <sub>4</sub> sample. . . . .	76
Figure 4.10	The field cooling of the single crystal of Gd <sub>5</sub> Si <sub>0.33</sub> Ge <sub>3.67</sub> measured with the magnetic field vector parallel to the a-axis, $H = 100$ Oe. Inset shows the magnetisation around the Néel temperature (labeled with an arrow). . . . .	82
Figure 4.11	The magnetic field dependencies of the magnetization of the zero-field cooled single crystal of Gd <sub>5</sub> Si <sub>0.33</sub> Ge <sub>3.67</sub> measured at $T = 70$ K when the magnetic field vector is parallel to the a-axis. The dashed lines show the extrapolated magnetic behavior without the magnetic field-induced AFM-FM transition during the second field-increasing measurement. . . . .	83
Figure 4.12	Integrated intensity of the (0 7 0) magnetic reflection measured upon heating the Gd <sub>5</sub> Ge <sub>4</sub> sample. The data is normalized by the (0 8 0) charge reflection. The dotted lines are drawn to guide the eyes. . . . .	85
Figure 4.13	The peak position of the rocking scans of the (0 8 0) charge reflection measured upon heating the Gd <sub>5</sub> Ge <sub>4</sub> sample. . . . .	86

- Figure 5.1 Field dependence of the magnetization of a zero-field cooled  $\text{Gd}_5\text{Ge}_4$  single crystal measured at  $T = 10$  K with the magnetic field parallel to the  $\mathbf{c}$  axis. . . . . 91
- Figure 5.2 Temperature dependence of the spin-flop field,  $H_{\text{sf}}$ , derived from the field dependence of the magnetization measured at different temperatures. (From Ref. [OPG<sup>+</sup>06]) PM, SF, and ZFAFM represent the paramagnetic phase, the spin-flop phase, and the zero-field antiferromagnetic phase, respectively. The dashed lines represent the two field-dependence measurements and two temperature dependence measurements using XRMS in the present experiment. . . . . 92
- Figure 5.3 The experimental arrangement consisting of the sample, analyzer and detector.  $\mathbf{k}$  and  $\mathbf{k}'$  are the incident and scattered x-ray wave vectors respectively. The magnetic field  $\mathbf{H}$  was applied along the vertical direction. The switch between  $\pi$ - $\sigma$  geometry (the detector arm in the horizontal plane) and  $\pi$ - $\pi$  geometry (the detector arm along the vertical direction) was accomplished by a motor-driven analyzer angle,  $\chi_{\text{an}}$ . . . . . 94
- Figure 5.4 (a) Energy scan of the charge Bragg reflection,  $(0\ 8\ 0)$ , across the Gd  $L_2$  absorption edge. The dashed line indicates the inflection point and is taken to be the absorption edge energy. (b) Energy scans at the nominally charge forbidden  $(0\ 7\ 0)$  reflection across the Gd  $L_2$  absorption edge in  $\pi$ - $\pi$  geometry at  $T = 7$  K (filled circles) and  $T = 140$  K (open circles). The peak approximately 0.002 keV above the absorption edge is the dipole resonance while the sharp peak approximately 0.02 keV higher arises from multiple charge scattering. . . . . 98

Figure 5.5	The (0 7 0) magnetic reflection measured with increasing magnetic field (along the $\mathbf{c}$ direction) in both $\pi$ - $\pi$ and $\pi$ - $\sigma$ geometries at $T = 9$ K. Integrated intensity normalized by the (0 8 0) charge reflection. . . . .	101
Figure 5.6	The (0 7 0) magnetic reflection measured with increasing magnetic field (perpendicular to the scattering plane) in both $\pi$ - $\pi$ and $\pi$ - $\sigma$ geometries at $T = 80$ K. Integrated intensity normalized by the (0 8 0) charge reflection. . . . .	102
Figure 5.7	The longitudinal scans of the (0 8 0) charge reflections measured in the reciprocal space with increasing field at $T = 9$ K. . . . .	103
Figure 5.8	Integrated intensity of the (0 7 0) magnetic reflection measured when the sample was warmed up. The open circles represent the measurement in the $\pi$ - $\pi$ scattering geometry in zero field. The closed circles represent the measurement in the $\pi$ - $\sigma$ geometry in a vertical magnetic field, $H = 13$ kOe (the spin-flop phase). Both are normalized by the integrated intensity of the (0 8 0) reflection measured in $\pi$ - $\sigma$ . For comparison, the data in $\pi$ - $\pi$ are divided by the geometric factor, $(\sin 2\theta / \cos \theta)^2$ . . . . .	107
Figure 5.9	Integrated intensity of the (0 7 0) magnetic reflection measured when the sample was warmed up in a vertical magnetic field, $H = 13$ kOe. The data in both scattering channels are normalized by the integrated intensity of the (0 8 0) reflection measured in $\pi$ - $\sigma$ . For comparison, the data in $\pi$ - $\pi$ are divided by the geometric factor, $(\sin 2\theta / \cos \theta)^2$ . The straight line is drawn to guide the eyes.	109

- Figure 6.1 The field cooling inverse dc magnetic susceptibility of a single crystal  $\text{Gd}_5\text{Ge}_4$  measured along the **a** (a) , **b** (b) , and **c** axes (c) in magnetic fields ranging from 0.01 to 5 kOe. Panel (d) illustrates  $\log(H/M)$  vs  $\log(T/T_C - 1)$  for the three axes measured in a 10 Oe magnetic field and the same for the 5 kOe data along the **b** axis. ( $T_C$  is the critical temperature) Thick solid lines in (a)-(c) represent Curie-Weiss fits of the 5 kOe data. Solid lines in (d) are linear fits of  $\log(H/M)$  vs  $\log(T/T_C - 1)$  to establish  $\lambda$  in  $\chi(T) \propto (T - T_C)^{-(1-\lambda)}$ , with the dashed vertical line indicating the maximum slope of the curve for  $\mathbf{H} \parallel \mathbf{b}$ . Taken from Ref. [OPKAG+06] . . . . . 115
- Figure 6.2 Ferromagnetic (left side, high probability when  $0 < p < 0.5$ ) and antiferromagnetic (right side, high probability when  $0.5 < p < 1$ ) correlations between neighboring slabs in the Hendricks-Teller partial order. . . . . 117
- Figure 6.3 The intensity,  $I = f(q)^2$  v.s. the scattering vector,  $q = (0k0)$  generated from 400 layers stacking along **b** axis based on the Hendricks-Teller partial order model [HT42]. The model is described in the text. The step size is  $k = 0.2$  for data point generation. The colors represent different probabilities:  $p = 1$  (black), 0 (red), 0.05 (blue), and 0.95 (light blue). AFM is antiferromagnetic. FM is ferromagnetic. LRO is long-range order. SRO is short-range order. . . . . 122
- Figure 6.4 The longitudinal K scans,  $(0 \text{ K } -0.2)$ , of  $\text{Gd}_5\text{Ge}_4$  at three different temperatures 6 K (black), 130 K (blue) and 240 K (red) using the analyzer  $\text{Ge}(3 \ 3 \ 3)$ . The counting time for each data point is 20 seconds. . . . . 125

Figure 6.5	The transverse L scans, ( $0\ 7.35\ L$ ), of $Gd_5Ge_4$ at three different temperatures 6 K (black), 130 K (blue) and 240 K (red) using analyzer $Ge(3\ 3\ 3)$ . . . . .	127
Figure 6.6	The transverse L scans, ( $0\ 8.65\ L$ ), of $Gd_5Ge_4$ at three different temperatures 6 K (black), 130 K (blue) and 240 K (red) using analyzer $Ge(3\ 3\ 3)$ . . . . .	128

## CHAPTER 1. Introduction and Overview of the Work in this Thesis

The rare earth compounds,  $R_5T_4$  (T is Si or Ge) have been extensively studied since the discovery of a giant magnetocaloric effect (MCE) in  $Gd_5(Si_xGe_{1-x})_4$  in 1997 [PG97b, PG97d, PG97c, PG97a]. Modern magnetic refrigeration is based on the MCE: by exposing a working material to a changing magnetic field, the temperature of the material, which is in an adiabatic environment, changes monotonically with the external field. In contrast to the conventional gas cycle refrigeration driven by a compressor, the magnetic refrigeration is considered to be more environmentally friendly due to the use of solid refrigerants rather than Chloro-Flouro-Carbon gases that are known pollutants. Additionally, the magnetic refrigeration driven by magnetic field offers higher thermodynamic efficiencies. After 1997, a wide range of interesting magnetic phenomena, such as magnetoresistance and magnetostriction, were also found in mixed solid solutions,  $Gd_5(Si_xGe_{1-x})_4$  [MAI<sup>+</sup>98, MSG<sup>L</sup>+98, LPG99].  $Gd_5(Si_xGe_{1-x})_4$  alloys have received great attention recently not only because of their potential applications [PG97d, PG98, Mil06], but also because of the intriguing underlying physics.

The origin of the observed phenomena lies in the large entropy change associated with the first-order magnetostructural transition. This unusual transformation of the crystal structure causes a considerable change of specific interatomic and magnetic interactions [PG97c]. The alloys have a distinct slab-structure, where each slab is formed by more than one monolayer of atoms. The interatomic interactions between the monolayers

belonging to the same slab are strong and the interactions between the slabs are weak, which lead to the relative movement between neighbor slabs in the first order transition. These compounds have been studied with respect to their basic structural and, for some of them, their magnetic properties over the past four decades. However, the magnetic structures of  $\text{Gd}_5(\text{Si}_x\text{Ge}_{1-x})_4$  alloys had not been determined, which hampered our understanding of the magnetoelastic coupling between the magnetic structure and the crystallographic structure.

The high intrinsic resolution of synchrotron radiation provides a very sensitive probe of magnetism and magnetoelastic effects. The magneto-structural transition was investigated by measuring both crystallographic and magnetic diffractions simultaneously in  $\text{Gd}_5\text{Si}_{0.33}\text{Ge}_{3.67}$ . The antiferromagnetic phase is determined to have coupled layered structures, which can be compared to the artificial magnetic multilayer systems where magnetic layers are separated by nonmagnetic spacers. The giant magnetoresistance found in these materials can be explained as the consequence of nontrivial interlayer coupling from magnetoelastic interactions [TSP00]. For the ferromagnetic phase, 2D slabs are interconnected through Ge(Si)-Ge(Si) covalent-like bonds [CPP<sup>+</sup>00]. (see Fig. 2.4) The interslab bonds are broken when the distance between all Ge(Si) atoms increases during the transformation to the O(II) phase [PG97c], leading to AFM ordering.

$\text{Gd}_5\text{Ge}_4$  is believed to play a key role in advancing our understanding of the underlying physics for the  $\text{Gd}_5(\text{Si}_x\text{Ge}_{1-x})_4$  system. As we will mention in Chapter 2, the rich magnetic properties of  $\text{Gd}_5\text{Ge}_4$ , which has the representative crystallographic structure, but different magnetic phase diagram from that of other Ge-rich  $\text{Gd}_5(\text{Si}_x\text{Ge}_{1-x})_4$  alloys, motivated the first X-ray Resonant Magnetic Scattering (XRMS) study on this compound. Though a large number of publications had reported the novel magnetic properties of the  $\text{Gd}_5(\text{Si}_x\text{Ge}_{1-x})_4$  series before our study, no magnetic structure measurement had been done. Generally speaking, the magnetic properties of materials can not be fully understood without the detailed knowledge of the magnetic structure. Scat-

tering techniques are invaluable tools for such investigations. X-ray resonant magnetic scattering is ideal for the study of  $\text{Gd}_5(\text{Si}_x\text{Ge}_{1-x})_4$  compounds, in which naturally occurring Gd has a large neutron absorption cross section.

This study has revealed that below the Néel temperature,  $T_N = 127$  K, the antiferromagnetic order is described by a magnetic unit cell which is the same as the crystallographic unit cell. The magnetic interactions between all three Gd sublattices yield a commensurate magnetic structure with a propagation vector,  $q = 0$ . The magnetic moments are ferromagnetically aligned within the slabs, while their stacking in the **b**-direction is antiferromagnetic. Furthermore, all Gd sites order within the same magnetic space group,  $Pnm'a$ . The magnetic moments are primarily aligned along the **c**-axis and the **c**-components of the magnetic moments at the 3 different sites are the same within the error. (see the right part in Fig. 6.2)

Generally, spin reorientation transitions arise from the competition between different favorable orientations of the moments in a crystal. An understanding of the spin reorientation transitions can be related to the magnetic anisotropy. The magnetic structure of  $\text{Tb}_5\text{Ge}_4$  has been investigated by neutron scattering experiments and the spin-reorientation transition was reported [RMA<sup>+</sup>02]. Through the comparison between  $\text{Tb}_5\text{Ge}_4$  and  $\text{Gd}_5\text{Ge}_4$ , the subtle concave feature, found in the temperature dependence of magnetic order parameter in  $\text{Gd}_5\text{Ge}_4$ , is also interpreted as the result of spin reorientation. The possible origins of the magnetic anisotropies which trigger the spin reorientation are discussed.

Magnetic torque method is commonly used to measure the anisotropy energy in ferromagnet. Unfortunately, the magnetic anisotropy energy of antiferromagnets is not accessible through magnetic torque measurements and must instead be estimated from microscopic magnetic structure measurements. The spin-flop transition in FM/AFM slabbed (FM slabs stack antiferromagnetically)  $\text{Gd}_5\text{Ge}_4$  has been reported based on the magnetization measurements [LGL<sup>+</sup>04, OPG<sup>+</sup>06]. However, these measurements

provided no direct information regarding the arrangement of Gd moments on the three inequivalent sites in the spin-flop phase. The general interest in the origin of the magnetic anisotropy in Gd compounds also motivates the study of the spin-flop transition in  $\text{Gd}_5\text{Ge}_4$ . The experimental setup described in Fig. 5.3 offers the ability to measure the rotation of magnetic moments in a spin-flop transition with polarization analysis. The XRMS experiments on  $\text{Gd}_5\text{Ge}_4$  have shown that the antiferromagnetically aligned moments at the three Gd sites flop from the  $\mathbf{c}$  axis to  $\mathbf{a}$  axis at  $T = 10$  K with a critical field,  $H_{\text{sf}} = 9$  kOe, along the  $\mathbf{c}$  axis. The magnetic space group changes from  $Pnm'a$  to  $Pn'm'a'$  at all three sublattices. Both phases have intraslab FM correlations and interslab AFM correlations, which are unchanged in both phases below  $T_N = 125$  K. We conclude that this field induced transition is a pure spin-flop transition, since the antiferromagnetically ordered moments at the three Gd sites flop from the  $\mathbf{c}$  direction to the  $\mathbf{a}$  direction by the applied field along the  $\mathbf{c}$  axis at the transition. Though  $\text{Gd}^{3+}$  ions have negligible single ion anisotropy, the easy plane anisotropy of the ordered state in  $\text{Gd}_5\text{Ge}_4$  originates from the combination of both the magnetic dipolar interactions and to a lesser extent the SO coupling of the conduction electrons via  $4f$ - $5d$  exchange interaction.

Studies of the magnetization, heat capacity, and neutron scattering of  $\text{R}_5(\text{Si,Ge})_4$  indicate that significant magnetic short-range order (SRO) is retained above Néel temperature. These results have recently been interpreted as evidence of a Griffiths phase based on Small-Angle Neutron Scattering (SANS) measurements of polycrystalline  $\text{Tb}_5\text{Si}_2\text{Ge}_2$  [MAM<sup>+</sup>06]. A Griffiths phase is a nanoscale magnetic clustering phenomenon that is driven by randomness in magnetic interactions and can be induced by chemical disorder or competing magnetic interactions. Interestingly, a ferromagnetic (FM) Griffiths-like phase has also been proposed to exist above the Néel transition in antiferromagnetic (AFM)  $\text{Gd}_5\text{Ge}_4$  (based on magnetization studies) [OPKAG<sup>+</sup>06]. This is possible due to the nature of the AFM ordering in  $\text{Gd}_5\text{Ge}_4$ , which consists of strongly ferromagnetic

block layers that have a weak AFM inter-block coupling. Our diffraction studies on single-crystal specimens provided no direct evidence of the magnetic SRO in the compound, which may be due to the low signal to background ratio. However, the calculation of the experimental error excludes the possibility of the model of ferromagnetically coupled slabs with random orientation along  $\mathbf{b}$  axis above  $T_N$  in zero field.

## CHAPTER 2. Survey of $\mathbf{R}_5(\text{Si}_x\text{Ge}_{1-x})_4$

### Discovery of $\text{Gd}_5(\text{Si}_x\text{Ge}_{1-x})_4$

In 1967,  $\text{Gd}_5(\text{Si}_x\text{Ge}_{1-x})_4$  alloys were first found by Smith et al [STJ67] and Holtzberg et al [HGM67]. Smith et al reported that both  $\text{Gd}_5\text{Ge}_4$  and  $\text{Gd}_5\text{Si}_4$  have  $\text{Sm}_5\text{Ge}_4$ -type crystallographic structure, in which  $\text{Gd}_5\text{Si}_4$  orders ferromagnetically at  $T_C = 336$  K. Holtzberg et al used Ge as substitution for Si in the silicide structure and found that the diluted compounds maintain the magnetic properties and the O(I)-type orthorhombic structure for Si concentration above 50% ( $0.5 < x \leq 1$ ). The other parent compound,  $\text{Gd}_5\text{Ge}_4$ , has an O(II)-type orthorhombic structure which is different from  $\text{Gd}_5\text{Si}_4$ . The difference will be described in a later section. Different magnetic properties were found in the O(II)-type  $\text{Gd}_5(\text{Si}_x\text{Ge}_{1-x})_4$  ( $0 \leq x \leq 0.3$ ), which presents a low ordering temperature.  $\text{Gd}_5\text{Ge}_4$  orders antiferromagnetically in the low temperature region, while the addition of small amounts of Si orders first antiferromagnetically, then ferromagnetically, with decreasing temperature. The compounds  $\text{Gd}_5(\text{Si}_x\text{Ge}_{1-x})_4$  with  $0.3 < x < 0.5$  were not characterized but acknowledged as a ternary intermediate phases [STJ67, SJT67], since the end members of the solid solution are not isostructural.

In 1997, a giant magnetocaloric effect was reported by Pecharsky and Gschneidner in  $\text{Gd}_5(\text{Si}_x\text{Ge}_{1-x})_4$  alloys [PG97b, PG97d, PG97c, PG97a, PG98]. Subsequently, the first phase diagram (see Fig. 2.1) at zero field of the  $\text{Gd}_5(\text{Si}_x\text{Ge}_{1-x})_4$  system was determined by Pecharsky and Gschneidner due to interest in the relationship between the magnetic properties and crystallographic structures in the systems [PG97d, PG97c, PG98].

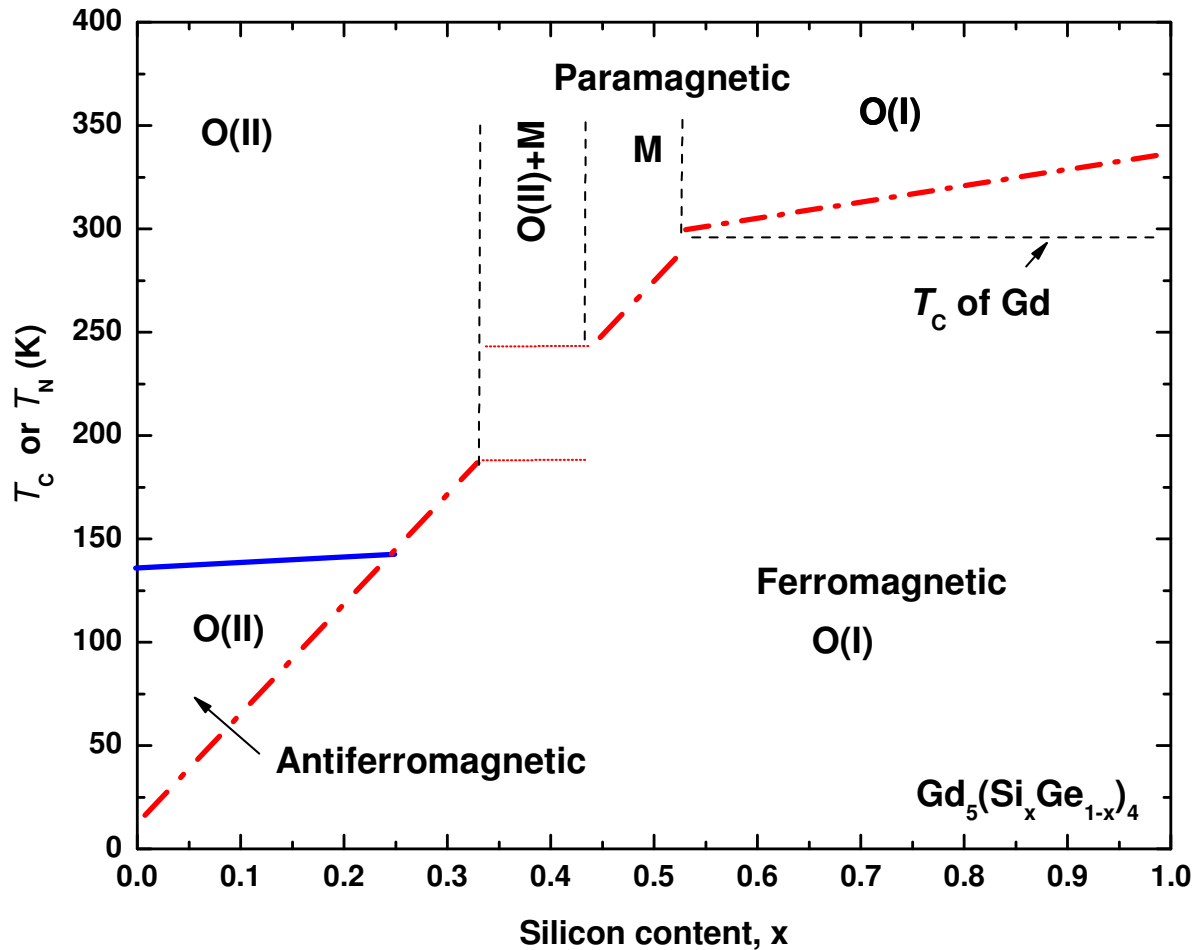


Figure 2.1 Magnetic and crystallographic phase diagram in zero applied magnetic field for  $Gd_5(Si_xGe_{1-x})_4$  alloys. Spontaneous magnetic ordering temperatures of  $Gd_5(Si_xGe_{1-x})_4$  compounds are described as functions of silicon concentration,  $x$ . O(I) for  $Gd_5Si_4$ -type orthorhombic structure and O(II) for  $Gd_5Ge_4$ -type orthorhombic structure. The thick solid lines delineate boundaries of the second order phase transitions, and the thick dash-dotted lines delineate the same for the first order phase transformations. The first order transition line doesn't reach the stoichiometry of  $Gd_5Ge_4$ , which represents no AFM-FM transition for  $Gd_5Ge_4$ . The Curie temperature of pure Gd metal (thin dashed line) is shown for reference purposes. (From Pecharsky and Gschneidner [PG97d, PG97c, PG98])

Samples over the whole composition range,  $0 < x < 1$ , were grown and characterized. The intermediate phase ( $0.3 < x < 0.5$ ) was identified as monoclinic [PG97c], which is labeled as the M-type structure. The low temperature transitions, which lead to the giant magnetocaloric effect in both the Ge-rich O(I)-type and the intermediate M-type compounds, were found to be first-order and reversible [PG97d].

### Properties of $\text{Gd}_5(\text{Si}_x\text{Ge}_{1-x})_4$

There are many novel properties found in the series of  $\text{Gd}_5(\text{Si}_x\text{Ge}_{1-x})_4$  that can be tuned by varying external parameters.  $\text{Gd}_5(\text{Si}_x\text{Ge}_{1-x})_4$  alloys, for  $x \leq 0.5$ , are most interesting, in which magnetocaloric effect [PG97b, PG97a, PG98, TBBdB02], colossal magnetostriction [MBAI00, MAI<sup>+</sup>98, HJS<sup>+</sup>04], giant magnetoresistance [MSGL<sup>+</sup>98, LPG99, LPGT00, MAMI01], unusual Hall effect [SMAI00], and spontaneous generation of voltage [LPG01, SBC<sup>+</sup>02]. were reported. The following is a short summary.

#### Magnetocaloric Effect

The magnetocaloric effect (MCE) can be exploited for magnetic refrigeration. Beyond its application in cryogenics, thermomagnetic cooling in refrigeration also is considered environmentally friendly in contrast to conventional vapor cycle cooling and has generated interest in both scientific and engineering fields. Furthermore, it was reported that magnetic refrigeration has the potential for higher efficiencies [TBBdB02], which can create savings in cost and energy consumption. The MCE is a magneto-thermodynamic phenomenon: by exposing a working material to a changing magnetic field, the temperature of the material, which is in an adiabatic environment, changes monotonically with the external field. This process is reversible. Physicists in the field of cryogenics often call MCE as adiabatic demagnetization. Nevertheless the MCE is an intrinsic property of a magnetic solid used as working materials in magnetic refrigeration.

One of the most used materials is gadolinium, which is the one with the previous best MCE at room temperature before the discovery of  $R_5(\text{Si}_x\text{Ge}_{1-x})_4$ . The magnetic entropy change,  $\Delta S_m$ , which can be calculated from the data obtained in magnetization measurements, is an important parameter for evaluation of MCE. By applying similar experimental conditions, the magnetic entropy change of  $\text{Gd}_5\text{Si}_2\text{Ge}_2$  [TBBdB02] is twice larger than that of Gd. This result was also confirmed by the heat capacity measurements with varying temperature and magnetic field. The magnetic entropy change,  $\Delta S_m$ , and the adiabatic temperature change,  $\Delta T_{ad}$ , was evaluated as a function of temperature from the magnetization measurements as shown in Fig. 2.2. The peak of  $\text{Gd}_5\text{Si}_2\text{Ge}_2$  is narrower and higher ( $\geq 30\%$ ) than that of pure Gd.

### Giant Magnetoresistance

In addition to a giant MCE, another remarkable phenomenon in  $\text{Gd}_5(\text{Si}_x\text{Ge}_{1-x})_4$  compounds, is the extraordinary magnetoresistance, in both  $0.24 \leq x \leq 0.5$  [MSGGL<sup>+</sup>98, LPG99, LPGT00] and in the  $0 \leq x \leq 0.2$  alloys [MAMI01]. Magnetoresistance is the change of electrical resistivity of a material under the application of an external magnetic field. The sign of the magnetoresistance found in  $\text{Gd}_5(\text{Si}_x\text{Ge}_{1-x})_4$  is negative, which is also found in multilayered structures composed of alternating layers of magnetic and non-magnetic metals, such as iron/chromium or cobalt/copper. In  $\text{Gd}_5(\text{Si}_x\text{Ge}_{1-x})_4$ , the field induced ferromagnetic phases show a low resistivity compared to the antiferromagnetic or paramagnetic phases. By exposing the samples to a changing magnetic field at selected temperatures, a negative but small magnetoresistance was observed from the O(I)/FM phase [MSGGL<sup>+</sup>98]. However, the drastic changes of the resistivity,  $\Delta\rho/\rho \simeq -50\%$ , occur at the magnetostructural first-order transition, which is reversible by the application of an external magnetic field above the Curie temperature. The temperatures required for triggering the giant magnetoresistance in  $\text{Gd}_5(\text{Si}_x\text{Ge}_{1-x})_4$  ( $x \leq 0.5$ ) can vary from  $\sim 20$  to  $\sim 290$  K with different  $x$  values.

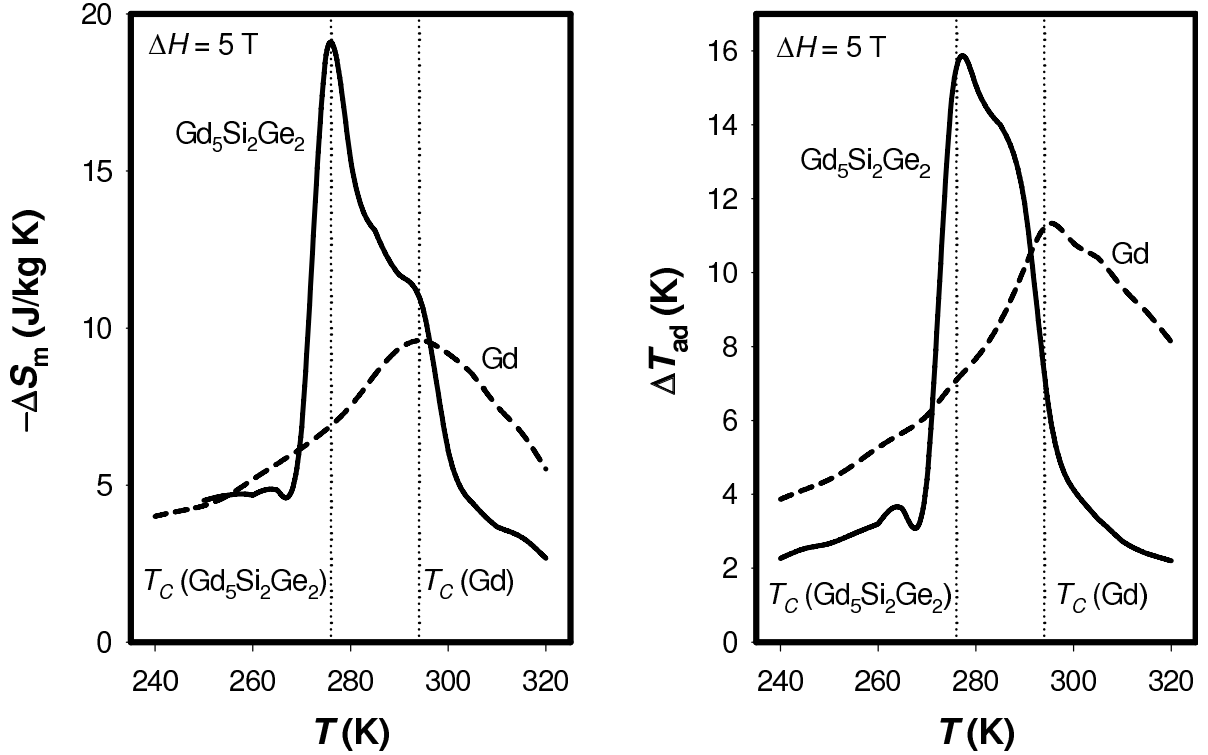


Figure 2.2 MCE curves comparing  $\text{Gd}_5\text{Si}_2\text{Ge}_2$  and Gd. (Left)  $\Delta S_m(T, \Delta H = 5$  Tesla) curves; and (right)  $\Delta T_{ad}(T, \Delta H = 5$  Tesla) curves. The Curie temperatures of 276 and 294 K, respectively, for  $\text{Gd}_5\text{Si}_2\text{Ge}_2$  and Gd are noted on the MCE curves. The figure is taken from Ref. [Mil06]. Data for these curves were taken from Ref. [PG97b]

Another interesting behavior was also found in the temperature dependence of the electrical resistivity in the alloys with  $0 \leq x \leq 0.2$ , which present a metal-insulator-like transition concomitant with the second order AFM-PM transition [LPGM01, SS99, MAMI01, SBC<sup>+</sup>03]. The electrical resistivity increases with temperature like a normal metal in the AFM phase and smoothly decreases with temperature in the PM phase. (see Fig. 4.8)

### Colossal Magnetostriction

Magnetostriction is a phenomenon in which the change in shape and volume of a material due to the application of magnetic field. In  $\text{Gd}_5(\text{Si}_x\text{Ge}_{1-x})_4$ , the magnetostriction effect also arises from the first order magnetostructural transition. Thermal expansions as large as  $\Delta l/l \simeq 0.16\%$  for  $0 \leq x \leq 0.2$  (i.e., a relative volume change  $\Delta V/V \simeq 0.48\%$ ) [MBAI00, MMA<sup>+</sup>03] and  $\Delta l/l \simeq 0.13\%$  ( $\Delta V/V \simeq 0.4\%$ ) for  $0.24 \leq x \leq 0.5$  [MAI<sup>+</sup>98] were observed at the Curie temperatures. Nazih et al reported that the single crystal with  $x = 0.43$  expanded along the **a** axis by as much as  $\Delta l/l = +0.68\%$  and shrank along the **b** and **c** axes as much as  $-0.20\%$  and  $-0.21\%$ , respectively [NdVZ<sup>+</sup>03]. Similar results were obtained by Hanet et al with an  $x \simeq 0.5$  single crystal [HPS<sup>+</sup>02]. Since the transition is also field-induced,  $\text{Gd}_5(\text{Si}_x\text{Ge}_{1-x})_4$  compounds for  $x \simeq 0.5$  can be used as magnetostrictive transducers, which convert magnetic energy into kinetic energy or the reverse.

### Crystallographic Structures in $\text{R}_5(\text{Si}_x\text{Ge}_{1-x})_4$

In 1967, Smith et al. found that the majority of silicides and all the germanides crystallized in the  $\text{Sm}_5\text{Ge}_4$ -type structure [STJ66, STJ67]. The  $\text{Sm}_5\text{Ge}_4$ -type structure was described as a five-layered sequence of monolayers stacked along the longest unit cell edge [SJT67]. Today, the view of the crystallography of the  $\text{R}_5(\text{Si}_x\text{Ge}_{1-x})_4$  compounds

has been changed since the further studies on the series of compounds reported that the apparently isostructural  $R_5Si_4$  and  $R_5Ge_4$  compounds have very different magnetic properties [HGM67, EZO<sup>+</sup>91]. In 1997, Pecharsky and Gschneidner studied samples over the entire composition range  $0 < x < 1$ , leading to the first phase diagram at zero field of the  $Gd_5(Si_xGe_{1-x})_4$  system [PG97d, PG97c, PG98]. (see Fig. 2.1) In all, three types of structures were found (O(I), O(II), M). The  $R_5(Si_xGe_{1-x})_4$  compounds are more appropriately described in terms of strongly interacting monolayers forming tightly bound [CPP<sup>+</sup>00], nearly two dimensional slabs stacking along **b** axis, as shown in Fig. 2.3. The features of rigidity inside the slab and flexibility between neighbor slabs were observed upon the first order structural transformation from one kind of slabbed structure to another, which provided the proof of much greater interactions within slabs than those between slabs. The neighbor slabs, stacking along the **b**-axis, may slide easily with different lateral displacements along the **a**-axis. The variation of one or more of the external thermodynamic parameters can motivate such martensitic-like structural changes.

Four distinctly layered structures were found in the  $R_5T_4$  compounds, where R represents rare earth metals and T represents the Group IVA elements, as shown in Fig. 2.4. (see Pecharsky's review [PG])

- The O(I): $Gd_5Si_4$ -type structure is illustrated in Fig. 2.4 (a). The distinct character in this type is the strong T-T bonds, where the T-atoms are located on the surfaces of the slabs. In consequence, strong interslab interactions are transferred along the **b**-axis. There are two types of T-T bonds: the short one  $\sim 2.6$  Å and the long one  $\sim 5.4$  Å shown as thick solid lines and dashed lines in Fig. 2.4, respectively. The crystal structure for such type is  $Pnma$  and known in the literature as the O(I)-type structure [PG97c]. A ferromagnetic state is coupled to the O(I)-type structure in the magneto-structural transition of PM/M-to-FM/O(I) or

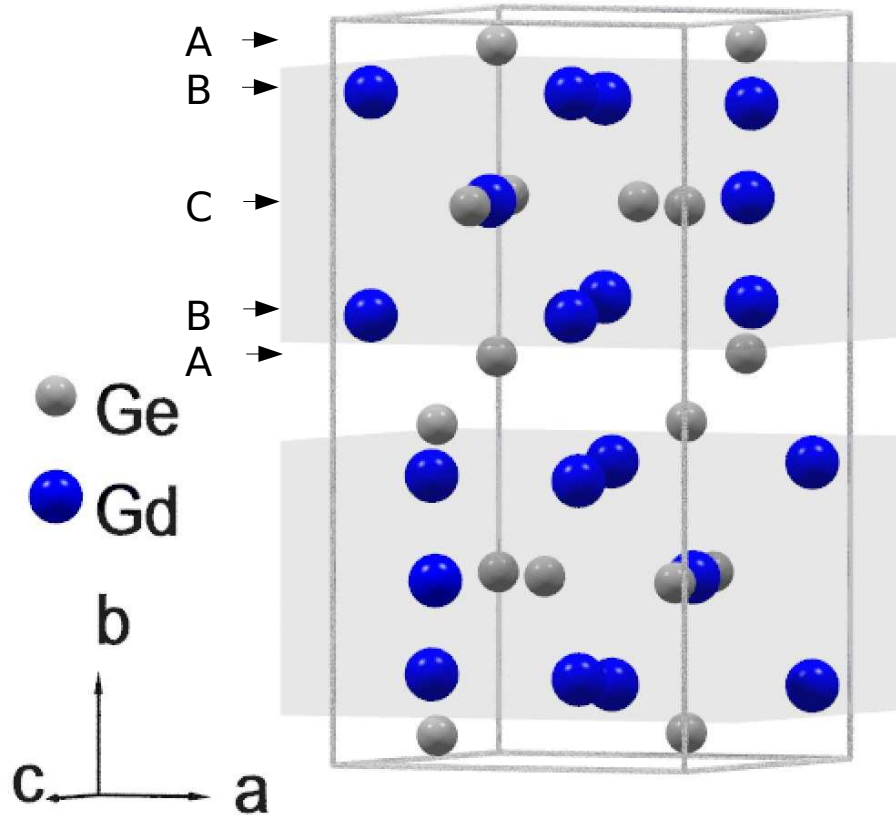


Figure 2.3 The crystal structure of  $Gd_5Ge_4$ . Shaded regions indicate the “slabs” stacked along the  $b$  direction. The slabs are infinite in the  $ac$  plane but they are limited to  $\sim 7 \text{ \AA}$  along the  $b$ -axis. It is interesting to note that each slab consists of five monolayers (ABCBA) stacked along the  $b$ -axis, originally used by Smith et al [SJT67] to describe the crystallography of the  $Sm_5Ge_4$ -type structure.

AFM/O(II)-to-FM/O(I).

- The M:Gd<sub>5</sub>Si<sub>2</sub>Ge<sub>2</sub>-type structure belongs to the  $P112_1/a$  space group symmetry and is shown in Fig. 2.4 (b). In such structure, the strongly bonded T-T dimers are only found between every other slab. Therefore only half populations of interslab interactions are formed strongly to be the short T-T bonds. The other half populations present relatively weak interslab interactions. The characterized distances for such weak ones are  $\sim 3.5$  and  $4.5$  Å for the short and long interslab T-T connections, respectively. Thus, the interslab magnetic interactions are much different [PG97c, CPP<sup>+</sup>00]. The Gd<sub>5</sub>Si<sub>2</sub>Ge<sub>2</sub>-type structure is associated with a paramagnetic state in the magneto-structural transition of PM/M-to-FM/O(I).
- The O(II):Sm<sub>5</sub>Ge<sub>4</sub>-type is illustrated in Fig. 2.4 (c). This type compounds crystallize in the space group  $Pnma$  and are known in the literature as the O(II)-type structure. Now, only weak interacting interslab T-T contacts are present with  $\sim 3.5$  Å short T-T pairs and the  $\sim 4.5$  Å long ones. No strongly bonded interslab T-T dimer is present. Such structure is associated with an antiferromagnetic state in the magneto-structural transition of AFM/O(II)-to-FM/O(I).
- The Tm<sub>5</sub>Si<sub>2</sub>Sb<sub>2</sub>-type [KPD04] is shown in Fig. 2.4 (d). The space group for this type structure is  $Ccmb$ , which has higher symmetry than all the other three structures. In the Tm<sub>5</sub>Si<sub>2</sub>Sb<sub>2</sub>-type structure, all interslab interactions are also uniform, which is similar to both the O(I) and O(II) type structures. Furthermore, all the interslab T-T distances are same, i.e.  $\sim 4.1$  Å.

In summary, the relations among the four crystal structures discussed above would be described in this way: one type structure can be generated by another by sliding neighboring slabs in opposite directions along the  $\mathbf{a}$ -axis. From the symmetry point of

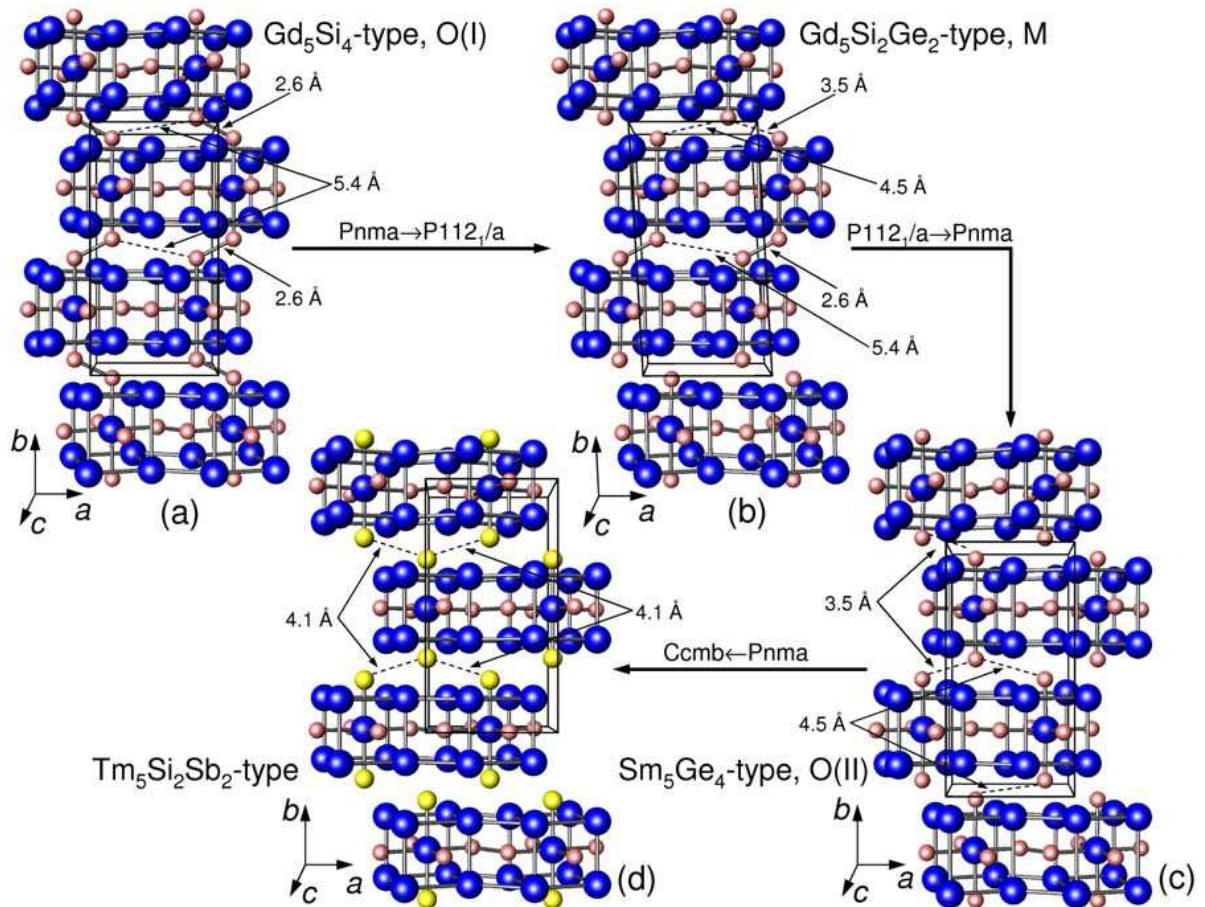


Figure 2.4 Four different types of layered structures found among  $R_5T_4$  compounds: (a) the  $Gd_5Si_4$ -type; (b) the  $Gd_5Si_2Ge_2$ -type; (c) the  $Sm_5Ge_4$ -type; (d) the  $Tm_5Si_2Sb_2$ -type. See the text for a description of differences and relationships among these four structure types. (From Ref. [PG])

view, the space group  $P112_1/a$  is a subgroup of  $Pnma$ , while the later is a subgroup of  $Ccmb$  [PG].

## Properties of $Gd_5Ge_4$

One end member in the  $Gd_5(Si_xGe_{1-x})_4$  system,  $Gd_5Ge_4$ , shows magnetocaloric effect, magnetoresistance, and magnetostriction related to the first order magnetostructural transition which result from the instability of its slab-formed chemical structure. Such instability arises from the role of T-site atoms which are located at the interslab locations. In  $Gd_5(Si_xGe_{1-x})_4$ , the positions of both Si and Ge atoms at T-sites are not randomly generated according to the ratio of their populations, but arranged with preference. Si atoms prefer the intraslab positions while Ge atoms favor the interslab positions [CPP<sup>+</sup>00, MM06]. In  $Gd_5Ge_4$ , the intrinsic disorder, due to the Si/Ge substitution on the T-sites, does not appear to exist. Thus the electronic structure of conduction bands, where exchange interactions are transferred, is expected to be influenced by the ratio of Si/Ge populations.

In zero field, the magnetic ground state of  $Gd_5Ge_4$  is AFM [LPGM01, LGP02, HMC<sup>+</sup>04, MMA<sup>+</sup>03, CLB<sup>+</sup>04]. No FM phase is observed when cooling from Néel temperature to 2 K, while the crystallographic structure remains in the O(II) phase [LPGM01, PHGR03], as shown in Fig. 2.5. The application of a magnetic field exceeding 18 kOe at 4.3 K transforms the AFM state in  $Gd_5Ge_4$  into a ferromagnetic FM state in a similar fashion to that usually observed during metamagnetic transitions (see the inset in Fig. 2.5). This observation is different from the behavior of the Ge-rich compounds ( $0 < x \leq 0.2$ ), which order AFM at  $\sim 125$ - $135$  K and undergo a first-order AFM/O(II)-to-FM/O(I) transition upon further cooling in zero field. However both the temperature and the applied magnetic field can induce the first order transition from AFM state into the FM state by exposing the  $Gd_5(Si_xGe_{1-x})_4$  sample ( $0 \leq x \leq 0.2$ ) to

a magnetic field exceeding  $\sim 10$  kOe. Again, the crystallographic transformation from the O(II)-type to the T-T bond rich O(I)-type polymorph occurs simultaneously with the magnetic transition [PHGR03, MHKAGP05].

The coupling between magnetic and crystallographic structures at the first order transition has led to the speculation that the restoration of strong T-T bonds between the slabs will considerably strengthen interslab magnetic exchange interactions. Haskel et al [HLH<sup>+</sup>07] applied X-ray magnetic circular dichroism (XMCD) measurements and density functional theory (DFT) to study the electronic conduction states in  $\text{Gd}_5(\text{Si}_x\text{Ge}_{1-x})_4$  materials through the first-order transition. The long-range Ruderman-Kittel-Kasuya-Yosida (RKKY) ferromagnetic interactions between the localized Gd  $4f$  moments in neighbor slabs, is communicated by the  $4p$  band of the Ge atoms at interslab positions, which is hybridized with Gd  $5d$  spin-dependent conduction states. The magnetic polarization of electrons in Gd  $5d$  conduction band is communicated to the Ge sites through the orbital hybridization. The Ge(Si) bond-breaking transition, which destroys 3D ferromagnetic order, act as a trigger regulating the strength of interslab RKKY exchange coupling [HLH<sup>+</sup>07].

The magnetization measurements show reversibility of the magnetostructural transformation induced by a magnetic field at low temperatures in  $\text{Gd}_5\text{Ge}_4$ , which is not presented in the measurement of any other member of the  $\text{R}_5(\text{Si}_x\text{Ge}_{1-x})_4$  family. There are three regions separated by  $\sim 10$  K and  $\sim 20$  K in the temperature dependent phase diagram. In the low and high temperature regions, the magnetic field-induced AFM-FM transition in a polycrystalline  $\text{Gd}_5\text{Ge}_4$  is irreversible and completely reversible, respectively. The intermediate region represents a mixture of states [CALB05, LGP02, TPGP04]. The magnetic phase diagram for  $x=0$  is displayed in Fig. 2.5. By regulating the sample temperature under a proper constant magnetic field, the first order reversible transitions were observed. The inverse FM/O(I)-to-AFM/O(II) transition can be induced by heating the sample to above 25 K. Above 25 K, the critical magnetic field

for the first order reversible transition response linearly with temperature [TPGP04]. A similar phase diagram with the first-order AFM/O(II)-to-FM/O(I) transition was reported if external hydrostatic pressure was applied as the alternative of magnetic field [MAM<sup>+</sup>03].

In addition to the interplay between reversibility and irreversibility of the magnetostructural transition, another interesting feature in  $\text{Gd}_5\text{Ge}_4$  is the possibility of magnetic short range order above the Néel temperature indicated by the low field magnetization measurement of a single crystal [OPKAG<sup>+</sup>06]. Beside  $\text{Gd}_5\text{Ge}_4$ , studies of the magnetization, heat capacity, and neutron scattering of  $\text{Tb}_5\text{Si}_2\text{Ge}_2$  indicate that magnetic short-range order is also retained. These results have recently been interpreted as evidence of a Griffiths phase based on Small-Angle Neutron Scattering (SANS) measurements of polycrystalline sample [MAM<sup>+</sup>06]. Above  $T_N = 127$  K but below  $T_G = 240$  K, the deviation of magnetization from Curie-Weiss behavior in  $\text{Gd}_5\text{Ge}_4$ , which is quite similar to that reported in polycrystalline  $\text{Tb}_5\text{Si}_2\text{Ge}_2$  [MAM<sup>+</sup>06], is also attributed to the Griffiths-like phase [Gri69]. Such deviations can be easily suppressed by magnetic fields above  $\sim 5$  kOe. Unlike the negligible anisotropy of the true paramagnetic state above 240 K, the Griffiths-like phase in  $\text{Gd}_5\text{Ge}_4$  exhibits strong magnetic anisotropy. In the measurements along all three axes, the magnetization along **b**-axis shows the largest value between 127 K and 240 K. Such magnetic anisotropy is consistent with the anisotropy found in the long range ordered FM  $\text{Gd}_5\text{Ge}_4$  phase, in which the easy magnetization direction is also along **b**-axis [OPG<sup>+</sup>06]. Ouyang et al believed that the dynamic FM clusters maintain the O(II)-type crystal structure in the AFM long range order state, which results from the competition between the AFM and FM interactions.

It seems that all magnetic properties mentioned above are related to the AFM/O(II) structure in  $\text{Gd}_5\text{Ge}_4$ . The magnetic structure of  $\text{Gd}_5\text{Ge}_4$  in AFM phase is expected to be similar to that of  $\text{Tb}_5\text{Ge}_4$  because of similarities in both chemical structure and magnetic phase diagram. Neutron powder experiments showed that  $\text{Tb}_5\text{Ge}_4$  has a com-

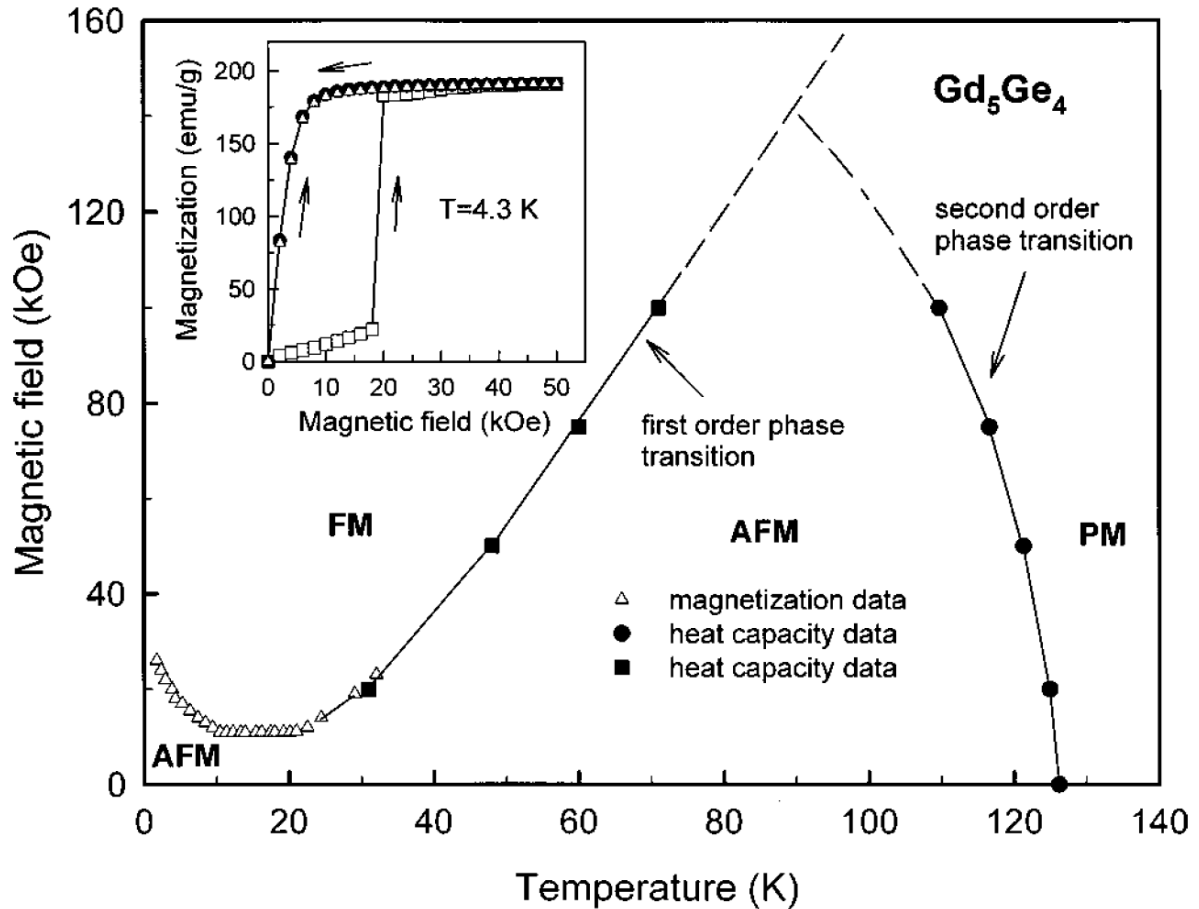


Figure 2.5 The magnetic phase diagram of  $Gd_5Ge_4$ , which was constructed from the heat capacity and magnetization data, delineates the phase fields observed in the system during iso-field heating or isothermal magnetizing. The inset shows the magnetization of  $Gd_5Ge_4$  cooled in zero magnetic field. During the first magnetic field increase, which is shown by open squares in the inset, a metamagnetic like transition occurs at  $\sim 18$  kOe. During the first magnetic-field reduction (closed circles) and during the second and following magnetic-field increases (opened triangles), the magnetization behavior is typical of a soft ferromagnet. (Taken from Ref. [LPGM01])

plex structure in the magnetic ordered state: the magnetic ordered slabs are coupled to each other with a commensurate antiferromagnetic modulation vector along the **b**-axis. Each slab has internal canted magnetic moments with all three components, in which the ferromagnetically coupled **c** component is the major one [SP78, RMA<sup>+</sup>02]. Ritter et al pointed out that a spin reorientation, which only affects the intraslab ferromagnetic canting without influence on the antiferromagnetic modulation, occurs below the Néel temperature in Tb<sub>5</sub>Ge<sub>4</sub> [RMA<sup>+</sup>02]. Though no scattering experiment had been done, the AFM structure of Gd<sub>5</sub>Ge<sub>4</sub> was proposed by Magen et al [MAM<sup>+</sup>03] as shown in Fig. 2.6. Due to the fact that the extrapolated Curie-Weiss temperature is positive in Gd<sub>5</sub>Ge<sub>4</sub> [HGM67, PG98, LGP02], which is even higher than that in Tb<sub>5</sub>Ge<sub>4</sub>, strong ferromagnetic exchange interactions is believed to be present in the AFM phase. A collinear structure was proposed for the antiferromagnetic phase (see Fig. 2.6) due to the high value of the Curie-Weiss temperature. However, Levin et al claimed that a small non-collinearity exists in Gd<sub>5</sub>Ge<sub>4</sub>, which originates from the exchange anisotropies from different Gd intraslab and interslab interactions [LGP02].

In summary, the magnetocaloric, magnetoelastic, and magnetoresistive effects in Gd<sub>5</sub>(Si<sub>*x*</sub>Ge<sub>1-*x*</sub>)<sub>4</sub> were believed to have their origins in an unusual transformation of the crystal structure causing a considerable change of specific interatomic and magnetic interactions. Before our XRMS studies, no detailed information about the magnetic structures of the materials existed, which hampered our understanding of the coupling between the magnetic structure and the crystallographic structure. In antiferromagnetic materials, the overall magnetization is zero. However, this is not necessarily achieved by a simple antiferromagnetic modulation. More complicated magnetic structures can arise in the Sm<sub>5</sub>Ge<sub>4</sub>-type orthorhombic crystal. We had applied the XRMS technique and used magnetic symmetry analysis to elucidate the antiferromagnetic structures of Gd<sub>5</sub>Ge<sub>4</sub> and Gd<sub>5</sub>(Si<sub>*x*</sub>Ge<sub>1-*x*</sub>)<sub>4</sub>. The first order magneto-structural transition was confirmed by measuring both crystallographic and magnetic diffraction simultaneously in Gd<sub>5</sub>(Si<sub>*x*</sub>Ge<sub>1-*x*</sub>)<sub>4</sub>.

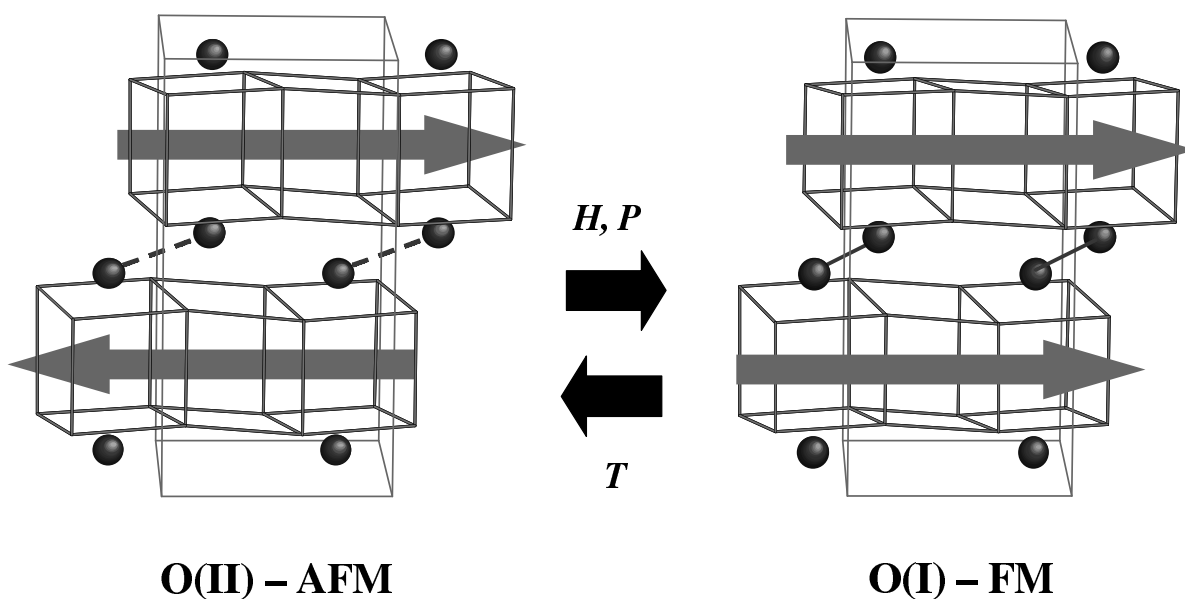


Figure 2.6 Schematic representation of the crystallographic and proposed magnetic structures of  $\text{Gd}_5\text{Ge}_4$  in the (a, b) plane at low temperature. Only the Ge atoms participating in the Ge-Ge covalent like bonds are depicted as solid spheres. A solid line linking the Ge atoms represents a formed bond [O(I)], whereas a dashed line is used for a broken one [O(II)]. Gray arrows are used to illustrate the change in the magnetic coupling induced by magnetic field, hydrostatic pressure or temperature. (From Ref. [MAM<sup>+</sup>03])

The antiferromagnetic phase is completely transformed into the ferromagnetic phase with a concomitant crystallographic structural change. The slab-formed layered magnetic order is naturally related to the slab shift in the structural changeover. The unusual order parameter found in  $\text{Gd}_5\text{Ge}_4$  motivated us to study the possible spin-reorientation in zero-field, which is related to the delicate competition between the magneto-crystalline anisotropies. The investigations of the spin-flop transition, which is induced by external magnetic field, provided insight into the magnetic anisotropy. Though  $\text{Gd}^{3+}$  ions have negligible single ion anisotropy, the easy plane anisotropy of the ordered state in  $\text{Gd}_5\text{Ge}_4$  originates from the combination of both the magnetic dipolar interactions and to a lesser extent the SO coupling of the conduction electrons via 4f-5d exchange interaction. Studies of the magnetization of  $\text{Gd}_5\text{Ge}_4$  indicate that magnetic short-range order (SRO) is retained above Néel temperature. However, our XRMS study could not find any significant evidence of SRO. The reason could be that the magnetic diffuse signal is below our sensitivity limit. Though no detailed information about the magnetic SRO can be concluded, the simple model with magnetic short-range order along **b**-axis and long-range order along **a** and **c** axes, which we proposed for the magnetic SRO in  $\text{Gd}_5\text{Ge}_4$ , is excluded.

## CHAPTER 3. X-ray Resonant Scattering and Symmetry Analysis

### Overview of X-Ray Scattering Techniques

X-ray diffraction by magnetic materials was first demonstrated by de Bergevin and Brunel [dB72] using an x-ray tube source. The effects induced by magnetic properties of the sample are usually very small compared with charge induced effects, e.g. Thomson scattering. In the past two decades there has been much new activity in the study of the magnetic properties of materials using x-rays. The fast recent developments in photon sources, based on synchrotron radiation and improved optics, have led to the fruitful results gained in X-ray studies of magnetic materials [Mar88]. Compared to conventional x-ray generators, there are some exciting advantages from the synchrotron radiation with the help of modern optics, which include: a high brightness with the option of superior resolution, a high degree of linear polarization, tunability of the primary photon energy, and the provision of good beams of circularly polarized photons [LC96].

X-ray scattering and neutron scattering are two invaluable methods in the study of magnetic structures in condensed matter. They are often complementary to each other. Each method has its own advantages and disadvantages for specific situations. When compared with the well-established technique of neutron magnetic diffraction, synchrotron-based photon diffraction has several intrinsic advantages:

First, the angular resolution obtained in photon diffraction is much better than that in a neutron diffraction experiment under similar experimental conditions. A direct

comparison can be found in some applications such as critical scattering from holmium [THH<sup>+</sup>94].

Second, relatively small samples are adequate for photon scattering experiments since the beam size can be quite small from highly collimated radiation and the photon flux is high from third generation of synchrotron sources.

Third, in non-resonant x-ray magnetic scattering, the ratio of spin and orbital components of the magnetic moment can be derived from polarization analysis [GGH<sup>+</sup>91]. Polarization analysis is a useful tool and utilized in both x-ray scattering and neutron scattering. The cross-sections for different magnetic components can be analyzed from the polarization of both the incoming and outgoing beam, and therefore provides information concerning the magnetic moment direction. Further, photon beams from a synchrotron source naturally have a high degree of linear polarization while neutron beams from reactor and spallation sources are unpolarized. The neutrons can only be polarized through a polarimeter with a reduced intensity.

Fourth, x-ray magnetic diffraction is a useful tool for scattering studies of the compounds which contain Gd, Eu, and Sm. In contrast, thermal neutron scattering is not applicable for these compounds unless an expensive isotopic substitution is used, since the naturally occurring Gd, Eu, Sm have large neutron absorption cross sections. Nevertheless, some compounds that contain the Gd, Eu, and Sm rare earth elements are very interesting. The first choice for microscopic measurements of these compounds would be X-ray magnetic scattering. For instance, in our case, the study of the magnetic properties of  $\text{Gd}_5(\text{Si}_x\text{Ge}_{1-x})_4$  alloys is feasible by applying x-ray magnetic scattering.

Finally, by tuning the energy of incoming x-ray beam close to the absorption edge of the atoms of interest, the resonant signal from scattering process is element specific which, for example, enables it to be used as a method of atomic labeling or to separate the magnetic contributions from different types magnetic ions. This is a very attractive feature in the study of complex magnetic materials containing different magnetic atoms.

## Resonant Magnetic Scattering

When the incident photon energy is tuned near an absorption edge of the target atom, large resonant enhancements of the scattering, which is related to a quantum-mechanical process, may be observed. The incoming photon first excites an inner shell electron from the ground state to a high energy state above the Fermi level in a photon-absorption transition. Subsequently, an inverse, photon-emitting, transition occurs and an elastic scattered photon is released, as depicted in Fig. 3.1. The cross section of resonant scattering depends on the specific absorption edge, photon polarization states, and the magnetic state of the sample since the scattered photon transfers the polarization information from the excitation state of the transition electron. Since the scattered photon acts as the carrier of the polarization state, resonant scattering technique is applicable for the investigation of magnetic materials, as first suggested by Blume [Blu85]. Experimentally, resonant scattering was first observed by Gibbs et al in 1988 in a study of the magnetic spiral structure of metallic holmium. [GHI<sup>+</sup>88] Subsequently the theoretical interpretation followed from Hannon et al in 1988 by using the model of electric multipole transitions [HTBG88].

Resonant scattering, as illustrated above, is considered a coherent elastic process. There are four parts to the total coherent elastic scattering amplitude: pure charge Thompson scattering and pure non-resonant magnetic scattering, and contributions from absorptive and dispersive processes. The latter two contributions can be understood on the basis of multipole transitions, which lead to both charge and magnetic scattering. The latter arises from the magnetic interactions of the electrons involved in the electric multipole transitions. For example in  $\text{Gd}_5\text{Ge}_4$ , the magnetic resonant scattering results from electric dipole transitions between  $2p$  core state and  $5d$  conduction band states, since the overlap between the radial functions of  $2p$  and  $5d$  is much larger than that of  $2p$  and  $6s$ . The largest resonant enhancements have been observed for incident photon

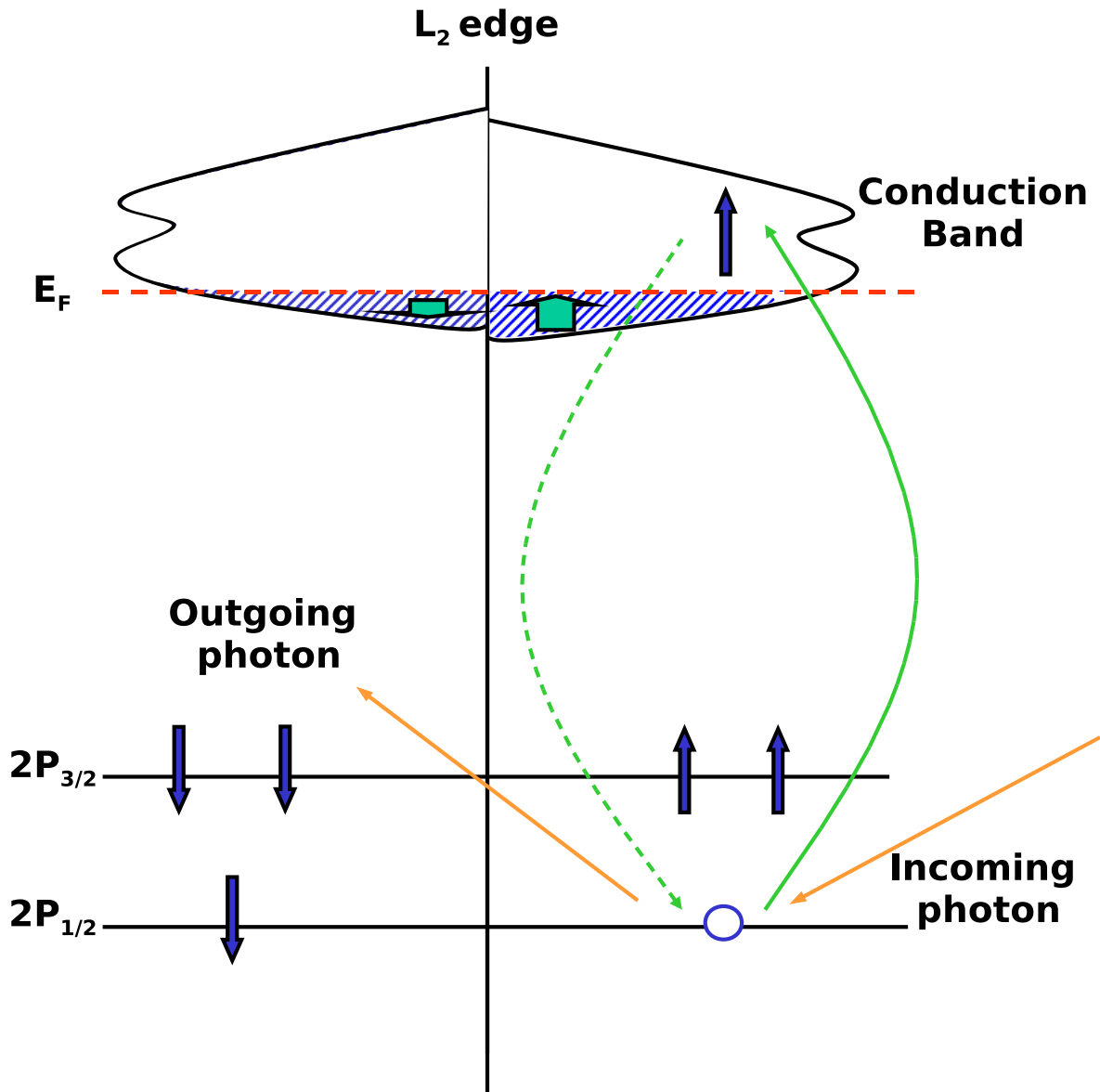


Figure 3.1 A schematic view of the XRMS process. Only a few core states are displayed, and the conduction bands are shown without the rich structure that exists in results from a realistic model. The figure shows the states when the core hole electron is excited above the Fermi level. The excitation and decay processes of the core electron happen within the core hole life time ( $\Gamma$ ). The offset in energy between spin up and down states results from the intra-atomic magnetic exchange interaction between  $4f$  and  $5d$  orbitals.

energies near the M absorption edges in actinides, and near the L absorption edges in rare earth and transition metals. For some resonances, the magnetic scattering is comparable to the charge scattering [MVI<sup>+</sup>90, TSL<sup>+</sup>92].

## Resonant Scattering Amplitude and Polarization Dependence

In the resonant scattering process, an inner shell electron is promoted by the incident photon into an unoccupied state above the Fermi energy, which subsequently decays through the emission of an elastically scattered photon. The amplitude for magnetic resonant scattering then depends on the matrix elements which couple the final state and the intermediate states allowed by the Pauli exclusion principle. Multipole operators of dipole, quadrupole, . . . , are generated by Taylor expansion of the exponential in the momentum operator.

Here, the details of the derivation for the magnetic scattering amplitude are not presented. The interested readers can read the relevant papers [Blu85, HTBG88, HM96]. From Eq. (13) in Blume's paper [Blu85], the cross section for scattering from an initial state,  $|a, k, \epsilon\rangle$ , into a final state,  $|b, k', \epsilon'\rangle$  should be:

$$\begin{aligned}
& \frac{d^2\sigma}{d\Omega' dE'} \tag{3.1} \\
&= \left(\frac{e^2}{mc^2}\right)^2 \left| \langle b | \sum_j e^{i\mathbf{Q}\cdot\mathbf{r}_j} | a \rangle \boldsymbol{\epsilon}'^\dagger \cdot \boldsymbol{\epsilon} \right. \\
&- i \frac{\hbar\omega}{mc^2} \langle b | \sum_j e^{i\mathbf{Q}\cdot\mathbf{r}_j} \mathbf{s}_j | a \rangle \cdot (\boldsymbol{\epsilon}'^\dagger \times \boldsymbol{\epsilon}) \\
&+ \frac{\hbar^2}{m} \sum_c \sum_{i,j} \left( \frac{\langle b | [\frac{\boldsymbol{\epsilon}'^\dagger \cdot \mathbf{p}_i}{\hbar} + i(\mathbf{k}' \times \boldsymbol{\epsilon}'^\dagger) \cdot \mathbf{s}_i] e^{-i\mathbf{k}' \cdot \mathbf{r}_i} | c \rangle \langle c | [\frac{\boldsymbol{\epsilon} \cdot \mathbf{p}_j}{\hbar} + i(\mathbf{k} \times \boldsymbol{\epsilon}) \cdot \mathbf{s}_j] e^{i\mathbf{k} \cdot \mathbf{r}_j} | a \rangle}{E_a - E_c + \hbar\omega_k - i\Gamma_c/2} \right. \\
&+ \left. \frac{\langle b | [\frac{\boldsymbol{\epsilon} \cdot \mathbf{p}_j}{\hbar} + i(\mathbf{k} \times \boldsymbol{\epsilon}) \cdot \mathbf{s}_j] e^{i\mathbf{k} \cdot \mathbf{r}_j} | c \rangle \langle c | [\frac{\boldsymbol{\epsilon}'^\dagger \cdot \mathbf{p}_i}{\hbar} + i(\mathbf{k}' \times \boldsymbol{\epsilon}'^\dagger) \cdot \mathbf{s}_i] e^{-i\mathbf{k}' \cdot \mathbf{r}_i} | a \rangle}{E_a - E_c - \hbar\omega_k} \right) \Big|^2 \\
&\cdot \delta(E_a - E_b + \hbar\omega_k - \hbar\omega_{k'}). \tag{3.2}
\end{aligned}$$

$\mathbf{k}$  and  $\boldsymbol{\epsilon}$  ( $\mathbf{k}'$  and  $\boldsymbol{\epsilon}'$ ) represent the wave vector and the polarization of the incoming (outgoing) photon.  $\mathbf{Q} = \mathbf{k}' - \mathbf{k}$  is the scattering vector.  $|a\rangle$ ,  $|b\rangle$ , and  $|c\rangle$  represent

the initial, final, and intermediate electronic states, respectively.  $\Gamma_c$  is the energy level width relevant to the intermediate-state lifetime.

In Eq. 3.5, the first term is normal Thompson scattering and the second is the non-resonant spin scattering. The third and fourth terms are the second-order perturbation expansion of the resonant scattering. The physical meanings of the last two terms are different: the incoming photon has been absorbed first (the third term) and the scattered photon has been released first (the fourth term). When the incident photon energy is tuned close to the energy for excitation of electron between the initial and the intermediate states ( $\hbar\omega \simeq E_c - E_a$  for absorption or  $\hbar\omega \simeq E_a - E_c$  for dispersion), the denominators in the third and fourth terms decrease to very small numbers comparing to the corresponding numerators. As a consequence, the third and fourth terms become important. Typically, the cross-section of the resonant magnetic scattering, though still considerably smaller than that of the Thompson scattering, is about  $50 \sim 100$  times as that of the non-resonant magnetic signal. In the study of ferromagnets, the charge and magnetic Bragg reflections overlap each other, since the modulation vectors for both structures are same. As a result, the charge signal overwhelms the magnetic part even with the improved signal to background ratio obtained from polarization analysis. However, in many antiferromagnets, the charge and magnetic Bragg reflections are well separated due to the difference in the modulation vectors. Therefore, the resonant magnetic scattering technique is commonly used in the study of antiferromagnets.

The exponential,  $e^{i\mathbf{k}\cdot\mathbf{r}}$ , can be expanded to first order to include electric dipole, magnetic dipole, and electric quadrupole interactions. The electric dipole interaction is dominant in resonant scattering in  $R_5(\text{Si}_x\text{Ge}_{1-x})_4$  as we see in Fig. 4.2 (b). Here, only the electric dipole interaction is considered and the scattering amplitude is:

$$F_{\text{XRES},E1} \sim \left(\frac{e}{mc}\right)^2 \sum_c \sum_{i,j} \frac{\langle b|\boldsymbol{\epsilon}^{\dagger} \cdot \mathbf{p}_i|c\rangle \langle c|\boldsymbol{\epsilon} \cdot \mathbf{p}_j|a\rangle}{E_a - E_c + \hbar\omega_k - i\Gamma_c/2} \quad (3.3)$$

$$= \left( \frac{e^2}{mc^2} \right) (E_c - E_a)^2 \sum_c \sum_j \frac{\langle a | \boldsymbol{\epsilon}^\dagger \cdot \mathbf{r}_j | c \rangle \langle c | \boldsymbol{\epsilon} \cdot \mathbf{r}_j | a \rangle}{E_a - E_c + \hbar\omega_k - i\Gamma_c/2} \quad (3.4)$$

$$= \left( \frac{e^2}{mc^2} \right) (E_c - E_a)^2 \sum_c \sum_j \frac{\boldsymbol{\epsilon}^\dagger \cdot \mathbf{Q}^\dagger \boldsymbol{\epsilon} \cdot \mathbf{Q}}{E_a - E_c + \hbar\omega_k - i\Gamma_c/2}. \quad (3.5)$$

where,  $\mathbf{Q} = \langle c | \mathbf{r} | a \rangle$ . The indices,  $i$  and  $j$  under  $\sum$  are the labels for identification of each electron in the material. We note that the initial state and the final state are identical,  $|a \rangle \equiv |b \rangle$ , for elastic scattering. In addition, a momentum operator,  $\mathbf{p}$ , can be substituted by a position operator,  $\mathbf{r}$ , using the commutation relation  $p = \frac{im}{\hbar}[H, r]$ .

Let us consider the diagram of schematic atomic energy levels displayed in Fig. 3.1. The splitting between the spin-up and spin-down electrons represents a net magnetic moment or an induced moment in the atom. The diagram is simplified by ignoring a finite energy width of core states in reality. The matrix elements of multipole transitions can be calculated by use of Fermi's Golden Rule. The transition rates depend on the initial and final states of spin-orbit configurations. The selection rules for dipole transitions require  $l' = l \pm 1$  and  $m' = m \pm 1, m$ . Since the overlap between the radial functions of  $2p$  and  $5d$  is much larger than that of  $2p$  and  $6s$ , the matrix element of the  $l' = l + 1$  transition is dominant over that of the  $l' = l - 1$  transition. A single magnetic quantum number is used for describing the states of the initial and intermediate orbitals, since  $\mathbf{Q}_n^\dagger \mathbf{Q}_{n'} (n = 0, \pm 1)$  vanishes unless  $n = n'$ .

$$\begin{aligned} (\boldsymbol{\epsilon}^\dagger \cdot \mathbf{Q}^\dagger)(\boldsymbol{\epsilon} \cdot \mathbf{Q}) &= \sum_n \boldsymbol{\epsilon}_n^\dagger \cdot \boldsymbol{\epsilon}_n |Q_n|^2 \\ &= \frac{1}{2} \left\{ \sum_n (\boldsymbol{\epsilon}^\dagger \cdot \boldsymbol{\epsilon}) (|Q_{+1}|^2 + |Q_{-1}|^2) \right. \\ &\quad \left. + i\boldsymbol{\mu} \cdot (\boldsymbol{\epsilon}^\dagger \times \boldsymbol{\epsilon}) (|Q_{+1}|^2 - |Q_{-1}|^2) \right\} \\ &\quad + (\boldsymbol{\mu} \cdot \boldsymbol{\epsilon}^\dagger)(\boldsymbol{\mu} \cdot \boldsymbol{\epsilon}) (2|Q_0|^2 - |Q_{+1}|^2 - |Q_{-1}|^2) \end{aligned} \quad (3.6)$$

Here,  $\boldsymbol{\mu}$  is a unit vector, which defines the magnetic quantization direction.

In Eq. 3.6, all terms are arranged according to the ascending order of powers of  $\boldsymbol{\mu}$ , which is a well-known result for the resonant scattering amplitude. This expression

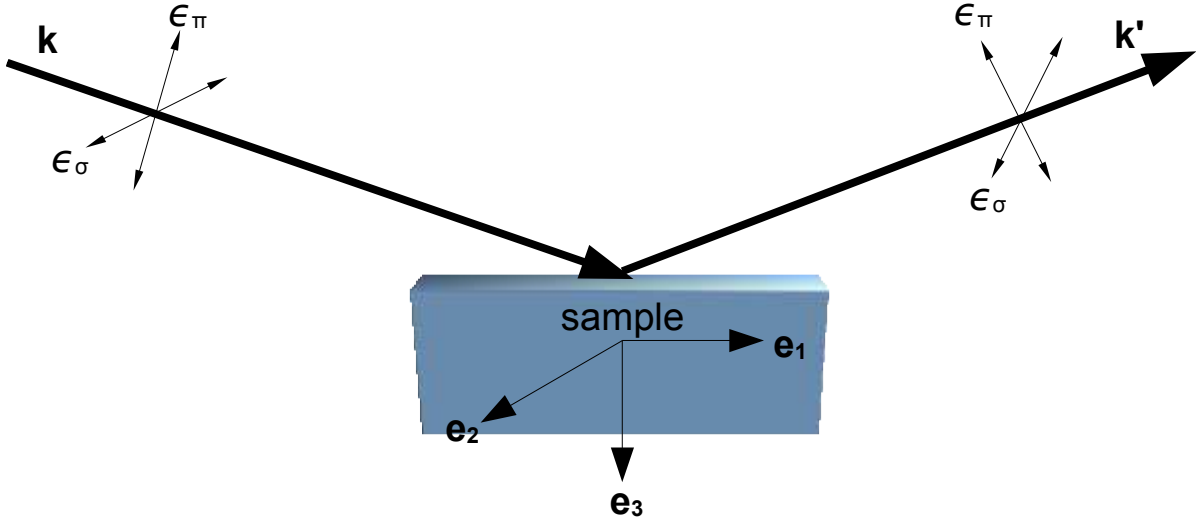


Figure 3.2 The coordinate system used for the polarization dependence of the resonant scattering amplitudes described in the text.  $\mathbf{k}$  and  $\mathbf{k}'$  are the incident and scattered wave vectors.  $\epsilon_\sigma$  and  $\epsilon_\pi$  are the components of the polarization perpendicular and parallel to the scattering plane. The  $e_2$  axis is perpendicular to the plane of scattering. The  $e_3$  axis is parallel to the scattering vector.

also provides a convenient form for polarization analysis. Fig. 3.2 shows the scattering geometry used in construction of the  $2 \times 2$  matrices according to the four different polarization channels:  $\sigma$ - $\sigma'$ ,  $\sigma$ - $\pi'$ ,  $\pi$ - $\sigma'$ , and  $\pi$ - $\pi'$ .  $\sigma$  and  $\pi$  polarizations are defined as photons polarized perpendicular to the scattering plane and polarized in the plane, respectively.

With regard to the dependence of the scattering amplitude on polarization states, a conclusive list is made based on the four polarization channels for the following terms:  $\epsilon' \cdot \epsilon$ ,  $(\epsilon' \times \epsilon) \cdot \mu$ , and  $(\epsilon' \cdot \mu)(\epsilon \cdot \mu)$ . The geometry matrices are listed in Table 3.1. There are three zero values for the scattering amplitude formed with Eq. 3.6: the two in the  $\sigma$ - $\pi'$  and  $\pi$ - $\sigma'$  channels from  $\epsilon' \cdot \epsilon$ , which is related to charge scattering, and the one in the  $\sigma$ - $\sigma$  channel from  $(\epsilon' \times \epsilon) \cdot \mu$ , which is related to magnetic scattering. Since magnetic scattering amplitude is usually much smaller than charge scattering amplitude, the  $\sigma$ - $\pi'$  and  $\pi$ - $\sigma'$  are two good choices for the measurement of magnetic resonant signal, where

Table 3.1  $\hat{k}$  and  $\hat{k}'$  denote unit vectors in the directions of the primary and secondary photon beams and  $\hat{k} \cdot \hat{k}' = \cos\theta$  where  $\theta$  is the angle of scattering. The vector  $\boldsymbol{\mu}$  is a unit vector, which defines the magnetic quantization axis, and  $\mu_{\perp}$ , is the projection of  $\boldsymbol{\mu}$  perpendicular to the plane of scattering. Polarization vectors parallel and perpendicular to the plane are denoted by  $\boldsymbol{\epsilon}_{\perp}$  and  $\boldsymbol{\epsilon}_{\parallel}$ , with  $\mu_{\perp} = (\boldsymbol{\epsilon}_{\perp} \cdot \boldsymbol{\mu}) = (\boldsymbol{\epsilon}'_{\perp} \cdot \boldsymbol{\mu})$ . Note  $\hat{k} = \boldsymbol{\epsilon}_{\perp} \times \boldsymbol{\epsilon}_{\parallel}$  and a similar relation for the secondary beam.

$\boldsymbol{\epsilon}' \cdot \boldsymbol{\epsilon}$	$\sigma$	$\pi$
$\sigma'$	1	0
$\pi'$	0	$\hat{k}' \cdot \hat{k}$

$(\boldsymbol{\epsilon}' \times \boldsymbol{\epsilon}) \cdot \boldsymbol{\mu}$	$\sigma$	$\pi$
$\sigma'$	0	$\hat{k} \cdot \hat{\boldsymbol{\mu}}$
$\pi'$	$-\hat{k}' \cdot \hat{\boldsymbol{\mu}}$	$(\hat{k}' \times \hat{k}) \cdot \hat{\boldsymbol{\mu}}$

$(\boldsymbol{\epsilon}' \cdot \boldsymbol{\mu})(\boldsymbol{\epsilon} \cdot \boldsymbol{\mu})$	$\sigma$	$\pi$
$\sigma'$	$\mu_{\perp}^2$	$\mu_{\perp}(\boldsymbol{\epsilon}_{\parallel} \cdot \boldsymbol{\mu})$
$\pi'$	$\mu_{\perp}(\boldsymbol{\epsilon}'_{\parallel} \cdot \boldsymbol{\mu})$	$(\boldsymbol{\epsilon}'_{\parallel} \cdot \boldsymbol{\mu})(\boldsymbol{\epsilon}_{\parallel} \cdot \boldsymbol{\mu})$

polarization suppression for charge scattering is realized.

Now let us start to illustrate the formation of satellite peaks in the reciprocal space. The high order satellite peaks are related to the terms with high powers level of  $\boldsymbol{\mu}$  in Eq. 3.6. We notice that  $\boldsymbol{\mu}$  in Eq. 3.6 is the function of the vector  $\mathbf{R}$  which defines the position of the magnetic atom.  $(\boldsymbol{\epsilon}' \times \boldsymbol{\epsilon}) \cdot \boldsymbol{\mu}(\mathbf{R})$  in Eq. 3.6 is the first order term of  $\boldsymbol{\mu}$ , which generates magnetic scattering. Since the Bragg reflections are Fourier transforms of the real space lattice in the reciprocal space, the total amplitude is  $\sum_{\mathbf{R}} \exp(i\mathbf{Q} \cdot \mathbf{R})(\boldsymbol{\epsilon}' \times \boldsymbol{\epsilon}) \cdot \boldsymbol{\mu}(\mathbf{R})$  for coherent scattering from an array of atoms, where  $\mathbf{Q}$  is the scattering vector. This expression can be simplified if the array of atoms are periodic. The scattering amplitude is then of the form,  $(\mu|\boldsymbol{\epsilon}' \times \boldsymbol{\epsilon}|)[\exp\{i\mathbf{R} \cdot (\mathbf{Q} + \boldsymbol{\tau})\} + \exp\{i\mathbf{R} \cdot (\mathbf{Q} - \boldsymbol{\tau})\}]$  where  $\boldsymbol{\tau}$  is the modulation wave vector. Bragg reflections occur when  $\mathbf{Q} \pm \boldsymbol{\tau} = \mathbf{G}$  where  $\mathbf{G}$  is a reciprocal vector for the magnetic lattice. If all terms in Eq. 3.6 are counted, dipole (E1) resonant scattering can contribute to Bragg reflections at a charge peak position and satellites positions with distances of  $\tau$  and  $2\tau$  to the center of the main charge reflection. Hill et al have pointed out that the quadrupole (E2) amplitude contains terms in  $\boldsymbol{\mu}$  from zero up to fourth order and there are thirteen distinct contributions [HM96].

## Symmetry Analysis

The Nobel laureate P. W. Anderson claimed that "it is only slightly overstating the case to say that physics is the study of symmetry." [And72] Symmetry is often studied in the theory of phase transitions since the phases involved in transitions often possess different levels of symmetry. As a consequence, a symmetry-breaking process is defined as the transition from the more symmetrical phase to a less symmetrical one. For example, the ferromagnetic transition is a symmetry-breaking transition. In this case, the symmetry is broken under reversal of the direction of electric currents and magnetic field lines in the ferromagnetic phase, where magnetic domains containing

aligned magnetic moments are formed. The relevant symmetry is named as "up-down symmetry" or "time-reversal symmetry". Here, by "time-reversal" I mean that the reverse transformation is applied to a time coordinate for the purpose of symmetry analysis. Since the electric currents will reverse direction under the time coordinate inversion, the term "time-reversal symmetry" describes the invariance of the system under such transformation.

When an effective spin Hamiltonian,  $H$ , is constructed for an ordered magnetic system, knowledge of the magnetic structure of the system (the ordered arrangement of the moments) is essential. The readers who are interested in magnetic crystallography can go further reading with Opechowski's "Magnetic Symmetry" [OG65] and Bertaut's paper [Ber68] for details.

In antiferromagnetic materials, the total magnetization is zero. However, this is not necessarily achieved by a simple up and down pattern in one dimensional case. Much more complicated structures can arise. A magnetic structure is fully described by propagation vector(s)  $k$ , the vectors  $\mathbf{S}_{kj}$  associated with magnetic moments for each magnetic atom  $j$  and propagation vector  $k$ , and a phase for each magnetic atom  $j$ ,  $\Phi_{kj}$  (included in  $\mathbf{S}_{kj}$ ). Here, we only discuss a specific case: the commensurate magnetic structure with a single propagation vector,  $k = (0, 0, 0)$ , where the magnetic structure can be described within the crystallographic unit cell. The magnetic symmetry is the combination of conventional crystallography plus the time reversal operator.

Before we go further in the discussion of magnetic symmetry, let us compare it with the conventional crystallographic symmetry, which describes the invariance of atomic positions under the symmetry operations of the space group. The objects under the crystallographic symmetry operations are atomic positions, which are scalars, while the objects under the magnetic symmetry operations are magnetic moments with positions, which are pseudovectors and change their signs under time inversion.<sup>1</sup> The crystallographic

---

<sup>1</sup>a pseudovector (or axial vector) is a quantity that transforms like a vector under a proper rotation,

structure is associated with conventional space group while the magnetic structure is associated with a new set of symmetry elements, the so-called magnetic or Shubnikov groups, which describe the invariance of magnetic structures. The invariance relevant to a magnetic structure requires that the spin configuration is invariant under all symmetry operations. New (primed) symmetry operations  $G'_k$ , where  $k$  is the propagation vector, are formed from the combination of conventional crystallographic symmetry elements  $G_k$  with the time-reversal operator  $R$ .

$$G'_k = G_k R = R G_k; R^2 = 1 \quad (3.7)$$

The effective spin Hamiltonian should be invariant under the new set of symmetry operations. The permutation of new symmetry elements will considerably enlarge the number of possible Shubnikov groups.

A system, which is confined by the magnetic structure, requires that the effective spin Hamiltonian is invariant under a Shubnikov group or, equivalently, invariant under time reversal. Therefore, the spin Hamiltonian must have the terms in even order of spins. For magnetic exchange interactions, we only take into account terms of order two in the spins:

$$H = -2 \sum_{R, R', i, j} A_{ij}(\mathbf{R}, \mathbf{R}') S_i(\mathbf{R}) S_j(\mathbf{R}') \quad (i, j = x, y, z) \quad (3.8)$$

Here,  $S_i(\mathbf{R})$  is the  $i$ -component of a spin  $S$  localized at point  $\mathbf{R}$ .  $A_{ij}(\mathbf{R}, \mathbf{R}')$  is a  $3 \times 3$  matrix which represents a tensor of rank two. All invariants of order 2 in the Hamiltonian are products of two basis vectors belonging to the same representation.

In order to help readers to understand the magnetic symmetry discussed above, we will introduce some relevant concepts in symmetry discussions and give the symmetry analysis of the  $8d$  sublattice belonging to the space group  $Pnma$ . The similar symmetry analysis of the  $4c$  sublattice can be found in the Bertaut's publication [Ber68].

---

but gains an additional sign flip under an improper rotation (a transformation that can be expressed as an inversion followed by a proper rotation). The conceptual opposite of a pseudovector is a (true) vector or a polar vector.

## The Independent Symmetry Elements

Symmetry elements and atomic positions are specified for all space groups in the International Tables for Crystallography. For instance,  $\text{Gd}_5\text{Ge}_4$  belongs to the orthorhombic space group  $Pnma$ . Gd atoms are located at three sublattices, one  $4c$  and two  $8d$ . Sets of positions for atoms at the  $8d$  site:

Position 1 :  $x, y, z$

Position 2 :  $1/2 - x, -y, 1/2 + z$

Position 3 :  $-x, 1/2 + y, -z$

Position 4 :  $1/2 + x, 1/2 - y, 1/2 - z$

Position 5 :  $-x, -y, -z$

Position 6 :  $1/2 + x, y, 1/2 - z$

Position 7 :  $x, 1/2 - y, z$

Position 8 :  $1/2 - x, 1/2 + y, 1/2 + z$

Let us go through and find out the independent symmetry elements for the  $8d$  sublattice. If a symmetry element is applied to a given point  $(x, y, z)$ , other equivalent points are generated. There is a minimal number of the symmetry elements which is necessary to generate all the other equivalent points of the general position. Those in the minimal set are termed as independent symmetry elements. The symmetry planes  $n$ ,  $m$  and  $a$  are one possible selection for a set of the independent symmetry elements defining the space group  $Pnma$ . Another choice for the set of the independent symmetry elements could be the 2-fold screw axis  $\tilde{2}_x$  at  $(x\ 1/4\ 1/4)$ , the inversion center  $\bar{1}$  at  $(0\ 0\ 0)$ , and  $\tilde{2}_z$  at  $(1/4\ 0\ z)$ , which are used in the following discussion.<sup>2</sup> For instance  $\tilde{2}_x$  sends Position

---

<sup>2</sup>It may be seen that two successive operations  $\tilde{2}_x$  and  $\tilde{2}_z$  on the point  $(x, y, z)$ ,  $\tilde{2}_z(\tilde{2}_x(x, y, z))$ , are equivalent to the operation  $\tilde{2}_y(x, y, z)$ , so that  $\tilde{2}_y$  is no longer independent and can be omitted.

1 to Position 4, Position 2 to Position 3, Position 5 to Position 8, and Position 6 to Position 7;  $\bar{1}$  sends Position 1 to Position 5, Position 2 to Position 6, Position 3 to Position 7, and Position 4 to Position 8;  $\tilde{2}_z$  sends Position 1 to Position 2, Position 3 to Position 4, Position 5 to Position 6, and Position 7 to Position 8. The arrangement of the magnetic moments located at these positions should be also invariant under the symmetry operations, which requires that the magnitudes of the magnetic moments are same at all equivalent positions. Each component of the magnetic moments is subject to the constraints set up by the symmetry operations.

### Construction of Irreducible Representations

In this section, some terms in group theory are introduced. [FH91] The definition of Group requires that a mathematical system obey a few simple rules. Then, group theory seeks to illustrate all of the properties common to all systems that obey these rules. In the study of group theory, representations are a very useful tool, since it provides a “bridge” which connects the group theory with linear algebra. As a branch of mathematics, group representation theory helps us understand the properties of abstract groups via their representations, which is usually the linear transformations of vector spaces. For the study of a vector space, the term “representation” is reserved for the special case of linear representations, as the case is discussed here. “Irreducible” is a term used in linear algebra, which describes the relationship between a vector space and its subspaces. If a vector space  $V$  has a non-zero subspace fixed under the group action, it is termed as reducible. Otherwise, it is said to be irreducible.

In order to construct the basis for each irreducible representation, it is most practical to look for linear combinations of the spin vectors  $\mathbf{S}_j$ . ( $j = 1, 2, \dots, 8$  for the eight equivalent positions at  $8d$  site) These combinations should transform into themselves with or without a change of sign under the symmetry operations  $\tilde{2}_x$ ,  $\bar{1}$ , and  $\tilde{2}_z$ . A trivial

linear combination is the vector sum

$$\mathbf{F}_B = \mathbf{S}_1 + \mathbf{S}_2 + \mathbf{S}_3 + \mathbf{S}_4 + \mathbf{S}_5 + \mathbf{S}_6 + \mathbf{S}_7 + \mathbf{S}_8 \quad (3.9)$$

which describes a ferromagnetic arrangement with all spins “pointing” up. The “+” sign represents that the moment is along the spin up direction. Other combinations are easily found by simple permutation inspection. The symmetry operations require four “+” and four “−” signs in the sum. They are listed below:

$$\mathbf{G}_B = \mathbf{S}_1 - \mathbf{S}_2 + \mathbf{S}_3 - \mathbf{S}_4 + \mathbf{S}_5 - \mathbf{S}_6 + \mathbf{S}_7 - \mathbf{S}_8 \quad (3.10)$$

$$\mathbf{C}_B = \mathbf{S}_1 - \mathbf{S}_2 - \mathbf{S}_3 + \mathbf{S}_4 + \mathbf{S}_5 - \mathbf{S}_6 - \mathbf{S}_7 + \mathbf{S}_8 \quad (3.11)$$

$$\mathbf{A}_B = \mathbf{S}_1 + \mathbf{S}_2 - \mathbf{S}_3 - \mathbf{S}_4 + \mathbf{S}_5 + \mathbf{S}_6 - \mathbf{S}_7 - \mathbf{S}_8 \quad (3.12)$$

$$\mathbf{P} = \mathbf{S}_1 + \mathbf{S}_2 + \mathbf{S}_3 + \mathbf{S}_4 - \mathbf{S}_5 - \mathbf{S}_6 - \mathbf{S}_7 - \mathbf{S}_8 \quad (3.13)$$

$$\mathbf{Q} = \mathbf{S}_1 - \mathbf{S}_2 + \mathbf{S}_3 - \mathbf{S}_4 - \mathbf{S}_5 + \mathbf{S}_6 - \mathbf{S}_7 + \mathbf{S}_8 \quad (3.14)$$

$$\mathbf{R} = \mathbf{S}_1 - \mathbf{S}_2 - \mathbf{S}_3 + \mathbf{S}_4 - \mathbf{S}_5 + \mathbf{S}_6 + \mathbf{S}_7 - \mathbf{S}_8 \quad (3.15)$$

$$\mathbf{L} = \mathbf{S}_1 + \mathbf{S}_2 - \mathbf{S}_3 - \mathbf{S}_4 - \mathbf{S}_5 - \mathbf{S}_6 + \mathbf{S}_7 + \mathbf{S}_8 \quad (3.16)$$

The “−” sign represents the moment is along the defined spin down direction. The eight vectors  $\mathbf{F}_B$ ,  $\mathbf{G}_B$ ,  $\mathbf{C}_B$ ,  $\mathbf{A}_B$ ,  $\mathbf{P}$ ,  $\mathbf{Q}$ ,  $\mathbf{R}$ , and  $\mathbf{L}$  form the “basis of irreducible representations”. (We use the symbols of the basis of irreducible representations same as in Bertaut’s paper [Ber68].)

## Transformation Properties

The transformation properties of the irreducible representations, which are formed by the spin vectors  $\mathbf{S}_j$ , can be deduced from applying the symmetry operations  $\tilde{2}_x$ ,  $\bar{1}$ , and  $\tilde{2}_z$  to the  $x$ -,  $y$ -, and  $z$ -components of the eight vectors  $\mathbf{F}_B$ ,  $\mathbf{G}_B$ ,  $\mathbf{C}_B$ ,  $\mathbf{A}_B$ ,  $\mathbf{P}$ ,  $\mathbf{Q}$ ,  $\mathbf{R}$ , and  $\mathbf{L}$ . Due to the symmetry constraints, each component of the basis of irreducible representations should transform into itself with, or without, a change of sign. Let us consider, for instance,  $\tilde{2}_x$  operation on  $C_x$ :

$$\tilde{2}_x C_{Bx} = \tilde{2}_x(S_{1x} - S_{2x} - S_{3x} + S_{4x} + S_{5x} - S_{6x} - S_{7x} + S_{8x}) \quad (3.17)$$

$$= S_{4x} - S_{3x} - S_{2x} + S_{1x} + S_{8x} - S_{7x} - S_{6x} + S_{5x} = C_{Bx} \quad (3.18)$$

the signs of the  $x$ -components of the spins do not change under the transformation. However when  $\tilde{2}_x$  is acting on  $C_y$ , the  $y$ -components of the spins change sign:

$$\tilde{2}_x C_{By} = \tilde{2}_x(S_{1y} - S_{2y} - S_{3y} + S_{4y} + S_{5y} - S_{6y} - S_{7y} + S_{8y}) \quad (3.19)$$

$$= -S_{4y} + S_{3y} + S_{2y} - S_{1y} - S_{8y} + S_{7y} + S_{6y} - S_{5y} = -C_{By} \quad (3.20)$$

Similar work is done for the transformation properties of the other vectors components under the symmetry operations. Table 3.2 summarizes and lists the sign change for each component of the basis vector under the operations  $\tilde{2}_x$ ,  $\bar{1}$ , and  $\tilde{2}_z$ . The symmetry constrains require the quantity of each magnetic component is same.

## Invariants

An invariant means that the variable is unaffected by a designated operation or transformation. Table 3.2 already contains the information needed for the construction of invariants. According to the group representation theory, the results are only rearranged by picking out those components which transform in the same way. A set of definite transformation properties is named as a ‘‘representation’’. For instance, the

Table 3.2 Transformation properties of the basis vectors for 8d site

<i>Vectors</i>	Operations								
	$\tilde{2}_x$			$\bar{1}$			$\tilde{2}_z$		
	<i>x</i>	<i>y</i>	<i>z</i>	<i>x</i>	<i>y</i>	<i>z</i>	<i>x</i>	<i>y</i>	<i>z</i>
$F_B$	+	-	-	+	+	+	-	-	+
$G_B$	-	+	+	+	+	+	+	+	-
$C_B$	+	-	-	+	+	+	+	+	-
$A_B$	-	+	+	+	+	+	-	-	+
$P$	+	-	-	-	-	-	-	-	+
$Q$	-	+	+	-	-	-	+	+	-
$R$	+	-	-	-	-	-	+	+	-
$L$	-	+	+	-	-	-	-	-	+

Table 3.3 Transformation properties of the basis vectors

Magnetic groups	Representations	<i>x</i>	<i>y</i>	<i>z</i>
$Pnma$	$\Gamma_1(+ + +)$	$C_{Bx}$	$G_{By}$	$A_{Bz}$
$Pn'm'a$	$\Gamma_2(- + +)$	$G_{Bx}$	$C_{By}$	$F_{Bz}$
$Pnm'a'$	$\Gamma_3(+ + -)$	$F_{Bx}$	$A_{By}$	$G_{Bz}$
$Pn'ma'$	$\Gamma_4(- + -)$	$A_{Bx}$	$F_{By}$	$C_{Bz}$
$Pn'm'a'$	$\Gamma_5(+ - +)$	$R_x$	$Q_y$	$L_z$
$Pnma'$	$\Gamma_6(- - +)$	$Q_x$	$R_y$	$P_z$
$Pn'ma$	$\Gamma_7(+ - -)$	$P_x$	$L_y$	$Q_z$
$Pnm'a$	$\Gamma_8(- - -)$	$L_x$	$P_y$	$R_z$

transformation properties of  $F_{Bx}$  under the operations  $\tilde{2}_x$ ,  $\bar{1}$ , and  $\tilde{2}_z$  may be specified by (+ - -) which means that  $F_{Bx}$  does not change sign under  $\tilde{2}_x$ , but does change sign under  $\bar{1}$  and  $\tilde{2}_z$ . By inspecting all combinations of the components of basis vectors which are invariant under the transformations, there are eight possibilities or representations  $\Gamma_j$  ( $j = 1, 2, \dots, 8$ ). In Table 3.3, the vector components which belong to the same representation are on the same line.

A similar analysis on the 4c site can be done for the transformation properties of the basis vectors of the 4c site. The results for both 4c and 8d sites are summarized and reorganized in Table 3.4, which will be used in later chapters.

Table 3.4 The magnetic modes of the  $4c$  and  $8d$  Wyckoff sites for the 8 possible magnetic space groups of the crystallographic space group  $Pnma$  associated with a magnetic unit cell that is the same as the crystallographic unit cell (based on Reference 17 with a modified sequence of the atomic positions according to Reference 18). The basis vectors ( $A, C, F, G$  for a  $4c$  site,  $A_B, C_B, F_B, G_B, L, P, Q, R$  for an  $8d$  site) are characterized by the sign sequence for the magnetic moment components along the three crystallographic axes.

$i$	position			$Pn'ma$			$Pnm'a$			$Pnma'$			$Pn'm'a$			$Pnm'a'$			$Pn'ma'$			$Pn'm'a'$			$Pnma$		
	$a$	$b$	$c$	$a$	$b$	$c$	$a$	$b$	$c$	$a$	$b$	$c$	$a$	$b$	$c$	$a$	$b$	$c$	$a$	$b$	$c$	$a$	$b$	$c$	$a$	$b$	$c$
		$4c$		$G$	$G$	$A$	$A$	$C$	$F$	$F$	$C$	$F$	$F$	$C$	$F$	$F$	$C$	$A$	$A$	$G$	$G$	$C$	$C$	$C$	$C$	$C$	$C$
1	x	1/4	z	+	+	+	+	+	+	+	+	+	+	+	+	+	+	+	+	+	+	+	+	+	+	+	+
2	1/2-x	3/4	1/2+z	+	+	-	-	-	-	-	-	+	+	-	+	+	-	+	-	-	+	-	-	-	-	-	-
3	-x	3/4	-z	-	-	-	-	+	+	+	+	+	+	+	+	+	+	+	+	+	-	-	-	-	-	-	+
4	1/2+x	1/4	1/2-z	-	-	+	+	-	-	-	-	+	+	-	+	+	-	+	-	-	+	-	-	-	-	-	-
$i$	$8d$			$P$	$L$	$Q$	$L$	$P$	$R$	$Q$	$R$	$P$	$G_B$	$C_B$	$F_B$	$F_B$	$A_B$	$G_B$	$A_B$	$F_B$	$C_B$	$R$	$Q$	$L$	$C_B$	$G_B$	$A_B$
1	x	y	z	+	+	+	+	+	+	+	+	+	+	+	+	+	+	+	+	+	+	+	+	+	+	+	+
2	1/2-x	-y	1/2+z	+	+	-	+	+	-	-	-	+	-	-	+	+	+	-	+	+	-	-	-	+	-	-	+
3	-x	1/2+y	-z	+	-	+	-	+	-	+	-	+	+	-	+	+	-	+	-	+	-	-	+	-	-	+	-
4	1/2+x	1/2-y	1/2-z	+	-	-	-	+	+	-	+	+	-	+	+	+	-	-	-	+	+	+	+	-	-	+	-
5	-x	-y	-z	-	-	-	-	-	-	-	-	-	+	+	+	+	+	+	+	+	+	-	-	-	+	+	+
6	1/2+x	y	1/2-z	-	-	+	-	-	+	+	+	-	-	-	+	+	+	-	+	+	-	+	+	-	-	-	+
7	x	1/2-y	z	-	+	-	+	-	+	-	+	-	+	-	+	+	-	+	-	+	-	+	-	+	-	+	-
8	1/2-x	1/2+y	1/2+z	-	+	+	+	-	-	+	-	-	-	+	+	+	-	-	-	+	+	-	+	+	+	-	-

## Application

The above discussion yields the results of symmetry analysis from pure mathematics. Now we try to discuss briefly how this symmetry analysis is relevant to the features of a physical system. It was pointed out by Landau that, given any state of a system, one may unequivocally say whether or not it possesses a given symmetry [LLP80]. Landau also suggested that the free energy of any system should obey two conditions: that the free energy is analytic, and that it obeys the symmetry of the Hamiltonian [LLP80]. Therefore, a phase transition from one phase into another possessing a different symmetry must be described by the breaking of the analytical forms of the relevant Hamiltonian. Since the Hamiltonian of the system is invariant under the symmetry operations, an ordered structure can be the result of only a single irreducible representation for a second-order phase transition (For example, the PM-AFM transition in  $\text{Gd}_5\text{Ge}_4$ ). As a consequence, the number of possible structures and the variables that each involve are significantly reduced. Furthermore, the different terms in the exchange Hamiltonian also are constrained by the symmetry requirements. The limitations will help us to understand the features of the physical system. Since the Hamiltonian must be even in the spin components (invariance under spin reversal), the invariants of order two are simply constructed by pair multiplication of components which belong to the same representation. For instance, in line of  $\Gamma_1$  in Table 3.3 the products  $C_{B,x}^2$ ,  $G_{B,y}^2$ ,  $A_{B,z}^2$ ,  $C_{B,x}G_{B,y}$ ,  $G_{B,y}A_{B,z}$ , and  $C_{B,x}A_{B,z}$  are invariants, i.e. they do not change sign in symmetry operations. The interesting question arises now: how is the magnetic coupling between different sublattices? Only the vectors of different sublattices belonging to the same representation may be coupled, since the spin Hamiltonian is invariant under the symmetry operations. In the actual case, this means that only  $C_y$  at the  $4c$  site may couple with  $C_{B,x}$ ,  $G_{B,y}$ , and  $A_{B,z}$  at  $8d$  site since they belong to the same representation,  $\Gamma_1$  i.e.  $Pnma$  (see Table 3.4)

In summary, symmetry analysis not only provides a very useful tool for the reduction in the number of possible structures, but also helps us to understand them in terms of the different terms in the exchange Hamiltonian. As one example, in zero field, all three Gd sites in  $\text{Gd}_5\text{Ge}_4$  were determined to be in the same magnetic space group  $Pnm'a$  [TKK<sup>+</sup>05]. The occurrence of couplings belonging to the same representation, indicates that the Hamiltonian contains significant terms of order two. In a spin-flop transition, the  $\vec{S} \cdot \vec{H}$  term in the Hamiltonian, which is induced by external field, should be much smaller than other terms and acts as a perturbation to meet the requirement that only quadratic terms dominate in the Hamiltonian. Similarly, the anisotropy term in Hamiltonian in zero field should also act as a perturbation. The weak magnetic uniaxial anisotropy in the antiferromagnet is necessary for a spin flop transition, which is predicted by renormalization-group theory. [FN74, BA75, KNF76].

## Multiple Diffraction

As discussed in Chapter 4, the  $(0\ k\ 0)$  positions ( $k$  is odd) in reciprocal space, where magnetic reflections were found in  $\text{Gd}_5\text{Ge}_4$ , are forbidden for normal charge scattering. This separation between the magnetic and charge reflections provides the feasibility of magnetic reflections measurements. However, the charge forbidden positions can be still strongly contaminated by multiple charge diffraction [SJ89]. In order to improve the magnetic signal to the charge background ratio, the contamination from multiple charge diffraction has to be minimized. In this section, some background knowledge of multiple diffraction is provided. The readers who are interested in multiple diffraction can do further reading with Chang's book [Cha84].

## Geometry Condition

Multiple diffraction is sometimes named as multiple-wave diffraction,  $N$ -beam diffraction or multiple scattering. Multiple diffraction (MD), in contrast to a simple Bragg (the so-called two-beam incident and reflected) reflection, arises when an incident beam simultaneously satisfies the Bragg law for more than one set of lattice planes within a single crystal, i.e. when more than two reciprocal-lattice points touch the surface of Ewald sphere. The occurrence of MD depends on many geometrical factors: the lattice constants, the space group to which the crystal belongs, the wavelength of the radiation, and the experimental arrangement (such as the relative arrangement of the crystal with respect to the incident radiation). One specific example from three-wave diffraction will be given in the next section. [Cha84]

## An Example from Three-Wave Diffraction

Three-wave diffraction is illustrated in reciprocal space in Fig. 3.3. When the crystal is oriented in such a way that another reciprocal lattice point  $L$  is on the surface of Ewald sphere, multiple diffraction can occur. The reflection  $\mathbf{K}_G$  is called the primary reflection and the reflection  $\mathbf{K}_L$  is called the detoured (secondary) reflection. A third reflection  $\mathbf{K}_G - \mathbf{K}_L$ , the coupling reflection, is required to bring the detoured reflection back into the direction of the main reflection. In such a case, not only the primary reflection but also the combined secondary and coupling reflections do a contribution to the intensity observed in the detector. For an ideal single crystal, both  $G$  and  $L$  have to be located on the surface of the Ewald sphere to achieve the third beam diffraction condition, which can be affected by both incident-beam energy and azimuth angle  $\phi$ . ( see the next section) For three-wave  $(O, G, L)$  diffraction, the three reciprocal lattice points are coplanar, while the corresponding wave vectors may or may not be coplanar. For an  $N$ -wave diffraction with  $N > 3$ , both the reciprocal lattice points and wave

vectors may or may not be coplanar.

The general  $N$ -wave diffraction is more complex than three-wave diffraction. One specific type of  $N$ -wave diffraction ( $N \geq 3$ ) is very interesting since its occurrence depends only on crystal symmetry. It is called “systematic multiple diffraction”. [Cha84] This type of  $N$ -wave diffraction ( $N \geq 3$ ) occurs when reciprocal lattice points are coplanar, but not wave vectors. In the other words, if the radius of the reflection circle on the surface of the Ewald sphere is  $r_s$  and the radius of the Ewald sphere is  $r_E$ ,  $r_s < r_E$  must hold. All wavelengths, which keep  $r_s < r_E$  holds, make such MD occur. If  $r_s = r_E$ , all the reciprocal lattice points and wave vectors are coplanar. There is only one specific wavelength allowed for the occurrence of MD. This diffraction is called “coplanar coincidental diffraction” [Cha84].

The occurrence of all the  $N$ -wave diffractions with  $N \geq 2$ , depends on the lattice constants, the wavelength of incoming beam, and the crystal lattice symmetry. In order to depict all geometrical factors in one picture, the number of reciprocal lattice points including the origin of the lattice, which determines the number of diffracted beams in multiple diffraction, needs to be identified. In principle, it is possible to derive general conditions under which possible MD take place for a given lattice. However, it is difficult in practice to deduce such conditions, since the variable position of the reflection circle in a lattice provides a great variety of conditions under which MD occurs. It is also difficult to construct graphically the Ewald sphere for a three-dimensional lattice. Nevertheless, the cubic lattice should have the highest possibility of generating high order multiple diffractions [Cha84].  $\text{Gd}_5\text{Ge}_4$  crystallizes in the  $\text{Sm}_5\text{Ge}_4$ -type orthorhombic structure with the lattice constants  $a = 7.6838 \text{ \AA}$ ,  $b = 14.7930 \text{ \AA}$ , and  $c = 7.7628 \text{ \AA}$  at  $T = 6 \text{ K}$ . [PHGR03] The lattice constant  $a$  is very close to  $c$  and almost half of  $b$ . Each unit cell can be viewed as stacking of upper block and lower block. Each block is a “quasi-cubic”. Therefore, we may have a large density of MD in our XRMS experiments.

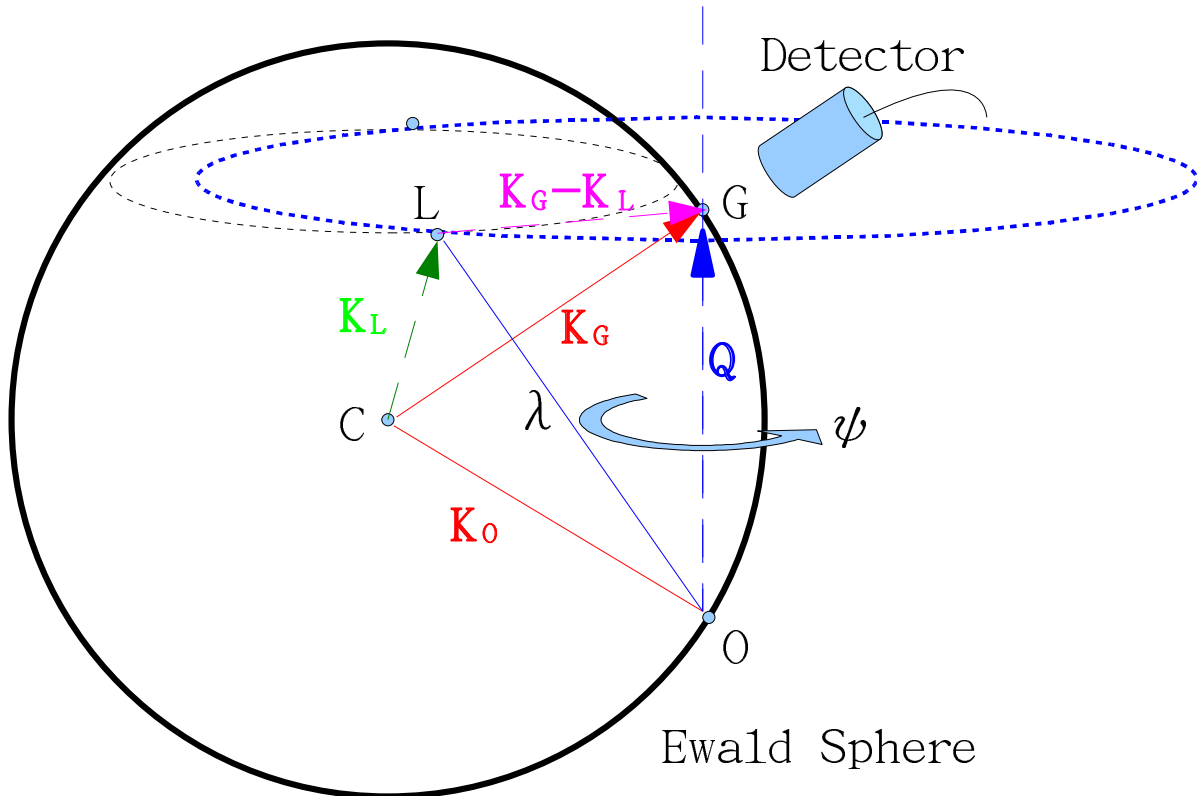


Figure 3.3 Geometry of one specific example of multiple diffraction formed by three wave vectors.  $C$  denotes the center of the Ewald sphere;  $O$  is the origin of reciprocal lattice space.  $G$  and  $L$  are the points on the surface of Ewald sphere.  $\psi$  is azimuthal angle.  $\mathbf{K}_O$ ,  $\mathbf{K}_G$ , and  $\mathbf{K}_L$  stand for incident, primary diffracted and secondary diffracted wave vectors, respectively. When both  $G$  and  $L$  are located on the surface of the Ewald sphere, a third beam diffraction condition is satisfied, for which  $\mathbf{K}_G - \mathbf{K}_L$  is the wave vector.

## Azimuth and Wavelength Dependence

Let's take the three-wave diffraction case described in Fig. 3.3. The Bragg condition for the primary reflection is always satisfied as long as the reciprocal lattice points  $O$  and  $G$  lie on the surface the Ewald sphere. One convenient way to achieve MD is to rotate a crystal around the scattering vector  $\mathbf{Q}$ , keeping the Bragg condition satisfied. This is the so-called azimuth  $\psi$  rotation. If an additional reciprocal lattice point, say  $L$ , is moved onto the surface of the Ewald sphere, then three-wave diffraction can take place. If the rotation is continued, the point  $L$  is moved away from the surface of the Ewald sphere and the three-wave diffraction disappears. If such azimuth rotation is kept going, other reciprocal lattice points  $M, N, \dots$  are moved onto and away from the surface of the Ewald sphere one by another. Such phenomena that the different multiple diffractions take place and then disappear were observed for resonant reflections from  $\text{Gd}_5\text{Ge}_4$  and are shown in Fig. 3.4. The second convenient way to achieve MD is to change the wavelength of the incoming radiation while the reciprocal lattice points  $O$  and  $G$  lie on the surface the Ewald sphere. If the wavelength decreases (increases), the Ewald sphere enlarges (shrinks). No matter how the shell of the Ewald sphere moves, the two points  $O$  and  $G$  stay on the surface, which ensures that the Bragg condition is satisfied. If an additional reciprocal lattice point,  $L$ , is moved onto the surface of the Ewald sphere, then three-wave diffraction can take place. The contour map of the energy dispersion v.s. azimuth rotation is shown in Fig. 3.4. In both ways, the peak width of a given multiple diffraction depends on how long the secondary reciprocal lattice points take to traverse the shell of the Ewald sphere during the crystal rotation. The thickness of the shell can be affected by the effective beam divergence, which depends on the mosaic spread of the sample, the intrinsic diffraction width of a perfect crystal and the geometry of the beam collimation.

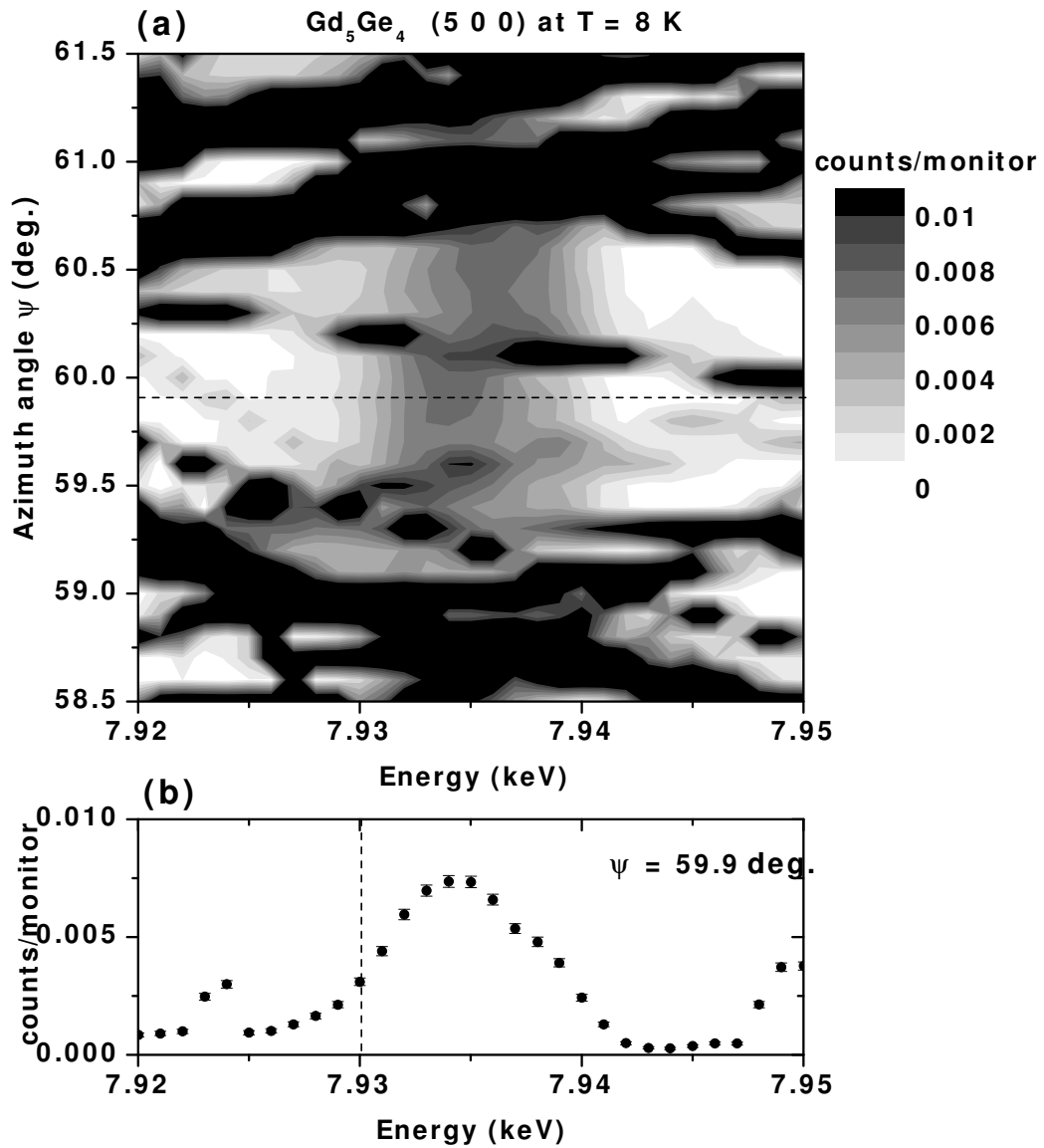


Figure 3.4 (a) Contour map of the intensity of  $\text{Gd}_5\text{Ge}_4$  (5 0 0) reflection as a function of energy and azimuth angle  $\psi$  at  $T = 8$  K. Discontinuities in the bands of multiple scattering across the energy range are artifacts from steps in mesh scans and (b) Single energy scan at the azimuth angle  $\psi = 59.9^\circ$ , which is depicted as a horizontal dashed line in (a). In (b), the vertical dashed line represents the position of the Gd  $L_{\text{II}}$  absorption edge. The maximum intensity at  $E = 7.934$  keV is a resonant signal, which is unchanged with the azimuth rotation.

## Polarization Factors in Multiple Diffraction

The polarization factors in multiple diffraction have been discussed in some publications. [Cha84, She04, She05] Here we only discuss a specific example in three-wave reflection as shown in Fig. 3.5.  $\mathbf{Q} = \mathbf{Q}(hkl)$ ,  $\mathbf{Q}_L = \mathbf{Q}_L(h_L k_L l_L)$ , and  $\mathbf{Q}_G = \mathbf{Q}_G(h_G k_G l_G) = \mathbf{Q} - \mathbf{Q}_L$  are the diffraction vector of the primary two-wave reflection, the secondary, and the coupling reflections, respectively. According to the usual definition of photon polarization, all  $\sigma$  vectors are perpendicular to the scattering plane and all  $\pi$  vectors lie in the scattering plane. The corresponding wave vector and the polarization vectors  $\sigma$ ,  $\pi$  forms a right-handed orthogonal axes system for each reflection. This is same as the conventional choice of unit polarization vectors for two-wave diffraction. However, this conventional way leads to an uncertainty in the directions of vectors  $\sigma$  and  $\pi$  due to the fact that each corresponding wave-vector could change direction in each specific three-wave multiple diffraction case. One convenient way to handle such uncertainty is realized by the definition of polarization factors in the following rule: all  $\sigma$  vectors are perpendicular to the diffraction vector  $\mathbf{Q}$  and all  $\pi$  vectors lie parallel to the scattering plane of the primary reflection, which is formed by the wave-vector  $\mathbf{K}_O$  of the incoming beam and the wave-vector  $\mathbf{K}_G$  of the diffracted one. There are two advantages: the system of unit polarization vectors is clearly associated with the azimuthal scan and the incident beam polarization state is unchanged, which helps the analysis of large numbers of multiple reflections.

For an easy analytical approach, we start with  $|\mathbf{Q}_G| = |\mathbf{Q}_L|$ , the same as for the case discussed in Ref [She04]. We use the final results from this publication:

$$\sigma_O \cdot \sigma_G = 1 \quad (3.21)$$

$$\sigma_O \cdot \pi_G = \sigma_G \cdot \pi_O = \sigma_O \cdot \pi_L = \sigma_G \cdot \pi_L = 0 \quad (3.22)$$

$$\sigma_L \cdot \pi_O = -\sigma_L \cdot \pi_G = \frac{\sin^2 \Theta (\cos^2 \Theta - \cos^2 \Sigma)^{1/2}}{\cos \Theta (1 - \cos \Sigma)} \quad (3.23)$$

$$\sigma_O \cdot \sigma_L = \sigma_L \cdot \sigma_G = \text{sign}(\cos \Sigma) \frac{\cos \Sigma - \cos^2 \Theta}{\cos \Theta (1 - \cos \Sigma)} \quad (3.24)$$

$$\pi_O \cdot \sigma_L = \pi_L \cdot \sigma_G = -\text{sign}(\cos \Sigma) \cos \Sigma \quad (3.25)$$

$$\pi_O \cdot \sigma_G = \cos 2\Sigma \quad (3.26)$$

The “sign” in the equations above is a function whose value is 1 when the variable is positive and  $-1$  when negative. In our experiments, the most commonly used polarization geometry is the  $\sigma$ - $\pi$  geometry. In the ideal situation, only photons in the  $\pi_G$  polarization state can pass through the polarization analyzer in the  $\sigma$ - $\pi$  geometry, in which the scattering plane for the sample is vertical but that for the analyzer is horizontal. For Thompson scattering, the polarization factor is  $\epsilon \cdot \epsilon'$ . If we assume that the incident beam is 100%  $\sigma$ -polarized and the polarization analyzer only allows  $\pi$ -polarized photons to pass through, we can use the equations above to get the polarization factor for the route from secondary to coupling reflections in the specific case described above. The polarization factor is square of

$$(\epsilon_O \cdot \epsilon_L)(\epsilon_L \cdot \epsilon_G) = (\sigma_O \cdot \epsilon_L)(\epsilon_L \cdot \pi_G) \quad (3.27)$$

$$= (\sigma_O \cdot \sigma_L)(\sigma_L \cdot \pi_G) \quad (3.28)$$

$$= -\text{sign}(\cos \Sigma) \frac{(\cos \Sigma - \cos^2 \Theta) \sin^2 \Theta (\cos^2 \Theta - \cos^2 \Sigma)^{1/2}}{\cos^2 \Theta (1 - \cos \Sigma)^2} \quad (3.29)$$

Thus generally, for  $\sigma$ -polarized incident beam, the scattered photons from multiple diffraction can pass through the polarization analyzer in  $\sigma$ - $\pi$  geometry, in which the polarization analyzer suppresses the primary charge diffraction.

## Application

Experimentally, the primary (Bragg) reflection may show a reduced or an enhanced intensity change while MD take places. Such an increase or a decrease in the intensity of a given two-beam reflection originates from the interaction among the diffracted

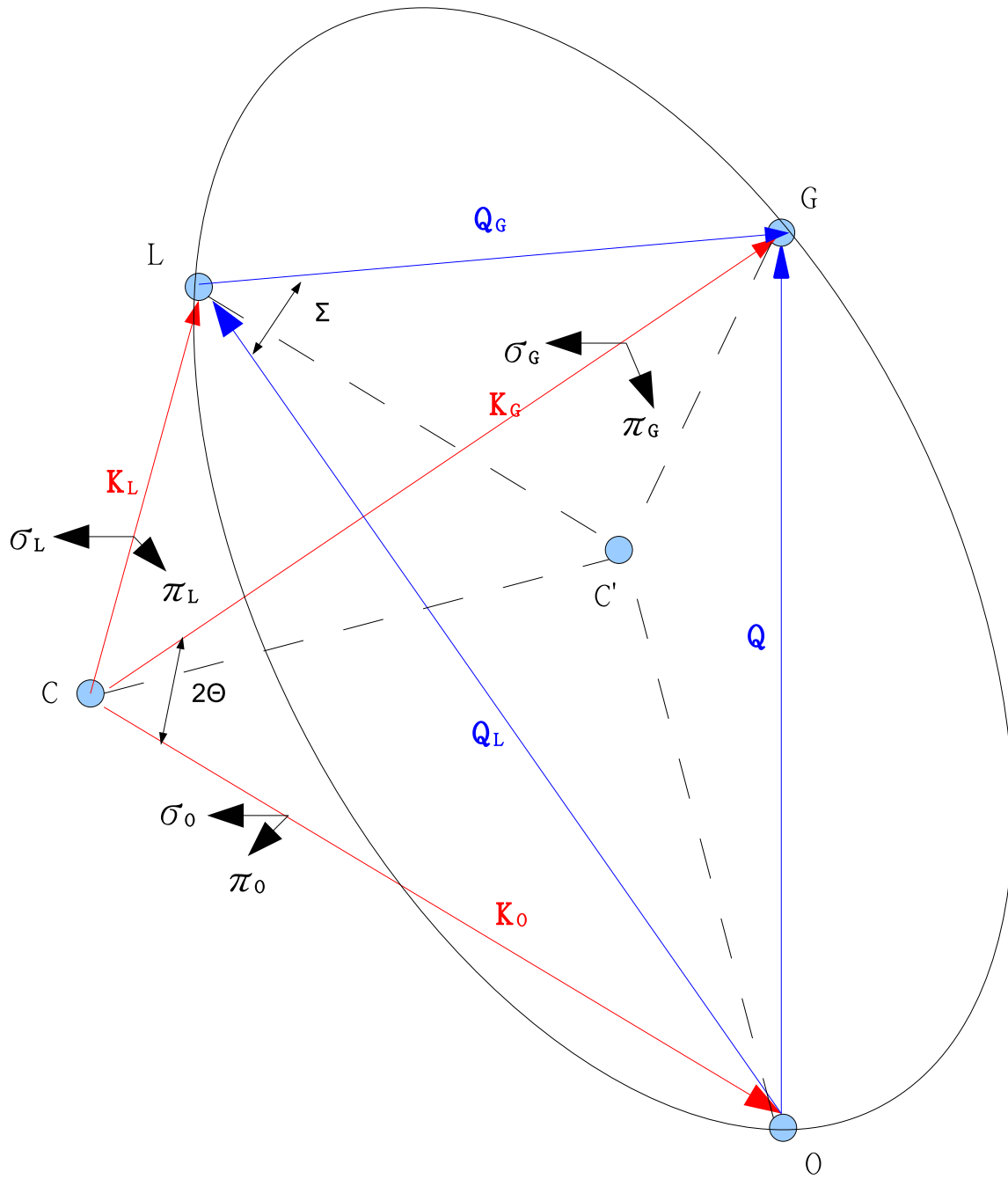


Figure 3.5 Choice of unit polarization vectors  $\sigma$  and  $\pi$  for symmetrical configuration. C denotes the center of the Ewald sphere; C' denotes the center of the optional circle;  $\mathbf{Q}$ ,  $\mathbf{Q}_L$ , and  $\mathbf{Q}_G$  represent scattering vectors. The wave-vectors  $\mathbf{K}_O$ ,  $\mathbf{K}_G$ , and  $\mathbf{K}_L$  lie in a section of Ewald sphere.

beams within the crystal. This kind of scattering power transfer has long been known. However, structural crystallographers always try to avoid such drastic effect that multiple diffraction has on diffracted-beam intensities, which is the “killer” for structure refinement. Synchrotron radiation has an advantages for MD topography as shown in Fig. 3.4 (a), i.e. wavelength dispersion. Synchrotron radiation enables a diffracting wavelength to be chosen that is optimal for the observation or elimination of multiple diffraction. Such a wavelength might not be available with a conventional source. In our XRMS experiment, we tried to minimize the MD contribution at the fixed resonant energy through a judicious choice of azimuth angle. (see Fig. 3.4)

## CHAPTER 4. The Magnetic Structure of $\text{Gd}_5\text{Ge}_4$ in Zero Field

### Introduction

The  $\text{Gd}_5(\text{Si}_x\text{Ge}_{1-x})_4$  alloys have received attention recently because of their unusually strong magnetocaloric [PG97b, PG97d], magnetostrictive [MBAI00, MAI<sup>+</sup>98], and magnetoresistive [MSGL<sup>+</sup>98, LPG99, LPGT00] properties when  $x \leq 0.5$ . All of these properties appear to be related to a first order magnetic transition accompanied by a martensitic-like structural change [TPS<sup>+</sup>04].

One of the end members of this series of compounds,  $\text{Gd}_5\text{Ge}_4$ , crystallizes in the  $\text{Sm}_5\text{Ge}_4$ -type orthorhombic structure with space group  $Pnma$ , and lattice constants  $a = 7.6838 \text{ \AA}$ ,  $b = 14.7930 \text{ \AA}$  and  $c = 7.7628 \text{ \AA}$  at  $T = 6 \text{ K}$  [PHGR03]. The Gd ions are located at one  $4c$  Wyckoff site and two inequivalent  $8d$  Wyckoff sites. They form two Gd-rich slabs, separated by sheets of Ge as shown in Fig. 2.3 [LGP02]. Below the Néel temperature,  $T_N \sim 127 \text{ K}$ , a second-order transition occurs where the Gd moments order antiferromagnetically. A first order magnetic transition from the antiferromagnetic phase (AFM) to a ferromagnetic phase (FM) occurs in an applied magnetic field of 18 kOe at  $T = 4.5 \text{ K}$  [LGP02]. Alternatively, when Si is substituted for Ge in  $\text{Gd}_5(\text{Si}_x\text{Ge}_{1-x})_4$  up to  $x < 0.2$ , a similar AFM  $\rightarrow$  FM first order transition occurs upon cooling in zero field [PG97c]. In both cases, the magnetic transition occurs concomitantly with a structural transition where the slabs shift relative to one another in the  $\mathbf{a}$  direction [PG97c, PHGR03]. From magnetization measurements and x-ray structural studies, it

has been proposed that the Gd magnetic moments are ferromagnetically aligned within the slabs, while the coupling between slabs can be antiferromagnetic or ferromagnetic. This indicates the presence of strong magneto-elastic coupling.

Details of the microscopic magnetic structure of  $\text{Gd}_5\text{Ge}_4$  or, in fact, any of the  $\text{Gd}_5(\text{Si}_x\text{Ge}_{1-x})_4$  alloys have not been determined largely due to the large neutron absorption cross-section of naturally occurring Gd. The aim of the present measurement is to elucidate the antiferromagnetic structure of  $\text{Gd}_5\text{Ge}_4$  using X-ray Resonant Magnetic Scattering (XRMS).

## Experimental Details

Single crystals of  $\text{Gd}_5\text{Ge}_4$  were grown using the Bridgman technique [SLPS05]. For the XRMS measurements, single crystals were extracted from the ingot and prepared with polished surfaces perpendicular to the crystallographic **a**- and **b**-axes, with a size of approximately  $2 \text{ mm} \times 2 \text{ mm}$ . The temperature dependence of the magnetization was measured with a SQUID magnetometer and is shown in Fig. 4.1. These data clearly show an antiferromagnetic transition at  $T_N = 127 \text{ K}$ , and indicate that the magnetic moment direction is likely mainly along the **c**-axis since the magnetization in **c**-direction,  $\chi_c$ , decreases to zero as temperature decreases to the base temperature. These results are in agreement with previous magnetization measurements [LGL<sup>+</sup>04].

The XRMS experiment was performed on the 6ID-B beamline in the MUCAT sector at the Advanced Photon Source at the Gd  $L_{\text{II}}$  absorption edge ( $E = 7.934 \text{ keV}$ ). The incident radiation was linearly polarized perpendicular to the vertical scattering plane ( $\sigma$ -polarized) with a spatial cross-section of  $1 \text{ mm}$  (horizontal)  $\times$   $0.2 \text{ mm}$  (vertical). In this configuration the resonant magnetic scattering, arising from electric dipole transitions ( $E1$ , from the  $2p$ -to- $5d$  states), rotates the plane of linear polarization into the scattering plane ( $\pi$ -polarization). In contrast, charge scattering does not change the polarization

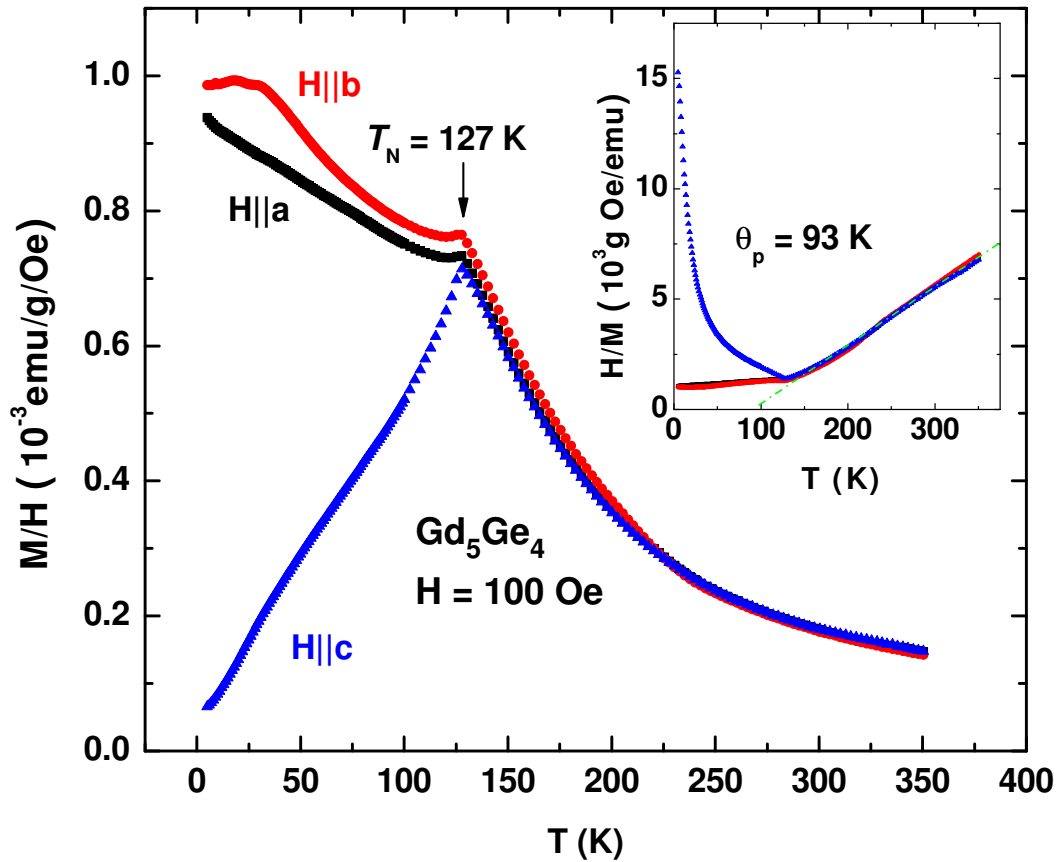


Figure 4.1 Magnetic susceptibility  $M/H$  of the  $Gd_5Ge_4$  single crystal. The temperature dependence of the susceptibility was measured on heating of the zero-field cooled sample in a field of 100 Oe applied parallel to the three crystallographic axes.

of the scattered photons ( $\sigma$ - $\sigma$  scattering). Pyrolytic graphite PG (0 0 6) was used as a polarization analyzer to suppress the charge background relative to the magnetic scattering signal.

Based on the predictions [LGL<sup>+</sup>04] of the AFM structure described above, the (0  $k$  0) reflections (for  $k$  odd) are expected to be strong magnetic reflections and forbidden for normal charge scattering. Therefore, the sample was mounted on the end of the cold-finger of a displex cryogenic refrigerator with the crystallographic **b**-axis parallel to the axis of the displex and set in the scattering plane. This configuration allows the sample to be rotated around the scattering vector **Q** (parallel to the **b**-axis) while keeping **Q** constant. In such an azimuth ( $\psi$ ) mode, either the **a-b** or **b-c** planes can be brought into coincidence with the scattering plane through a rotation of  $\psi$ . Since the resonant  $E1$  scattering is sensitive only to the component of the magnetic moment within the scattering plane, with a cross section  $f \propto \vec{k}' \cdot \vec{\mu}$  ( $\vec{k}'$  and  $\vec{\mu}$  are the wave vector of the scattered photons and the magnetic moment, respectively), all three cartesian components of the moment may be probed in this mode without remounting the sample [DIG<sup>+</sup>97].

In this particular experiment the magnetic peak positions are forbidden for normal charge scattering, but can be strongly contaminated by multiple charge scattering [SJ89]. However, the intensity of the multiple scattering is highly sensitive to both the incident beam energy and the azimuth angle  $\psi$ . For example, in Fig. 3.4 (a) a contour map of intensity in dependence on energy and azimuth angle is shown at the position of the (5 0 0) reflection measured on the sample surface cut perpendicular to the **a**-axis. The multiple scattering contribution at the resonant energy can be minimized through a judicious choice of azimuth angle as shown in Figure 3.4 (b), where the resonant scattering is well separated from the multiple scattering. We note that resonant scattering can arise from anomalous charge scattering in addition to magnetic scattering [FSS92].

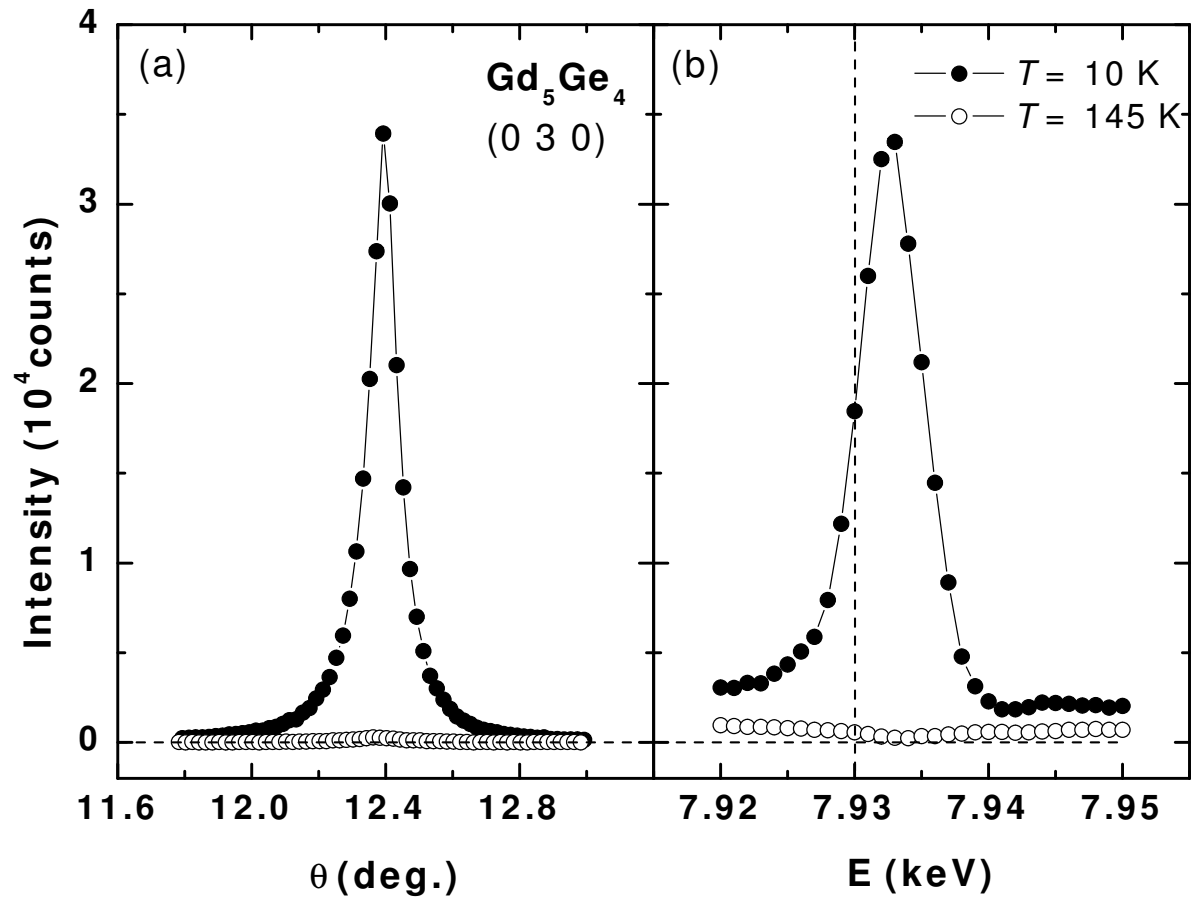


Figure 4.2 (a)  $\theta$  scan through the  $(0\ 3\ 0)$  magnetic peak at 10 K (filled circles) and 145 K (open circles) and (b) energy scans at 10 K (filled circles) and 145 K (open circles) through the magnetic peak. The data were measured at an azimuth angle of  $\psi = 30^\circ$  using aluminum attenuator with 0.41 transmission. The dashed line represents the position of the  $\text{Gd } L_{\text{II}}$  absorption edge.

## Magnetic Structure in Zero Field

With the sample at low temperature and oriented so that the **b-c** orthorhombic axes are coincident with the scattering plane, a strong magnetic reflection was found at the nominally forbidden (0 3 0) charge reflection position as illustrated in Fig. 4.2 (a). The full-width-half-maximum of the magnetic peak measured in  $\theta$ -scans (rocking curves) was  $0.1^\circ$ , the same as that from charge scattering. In order to confirm that the scattered intensity does indeed arise from resonant magnetic scattering, energy scans through the Gd  $L_{\text{II}}$  absorption edge were performed above and below the Néel temperature (See Fig. 4.2 (b)). At  $T = 145$  K, only charge scattering, arising from the tails of multiple scattering peaks, was observed. At low temperature, however, there is clear evidence of strong resonant scattering at the (0 3 0) magnetic peak position. Fig. 4.3 (a) displays the temperature dependence of the integrated intensity of the (0 7 0) magnetic peak. A Lorentzian peak shape was used to fit  $\theta$ -scans through the reciprocal lattice points to obtain the integrated intensities. The intensity decreases smoothly to zero as temperature increases up to  $T = 125$  K.. Magnetic reflections were found only at reciprocal lattice points (0  $k$  0), where  $k$  is odd. Therefore, the magnetic unit cell is the same as the crystallographic unit cell.

Having identified the location of the magnetic peaks and, therefore, the magnetic unit cell, we now turn to the determination of the magnetic moment direction in the antiferromagnetic structure. This was accomplished by azimuth scans through the (0  $k$  0) reflections. The (0 3 0) azimuth scan at  $T = 8$  K is shown in Figure 4.4. The integrated intensities of the magnetic peak are normalized by the intensity of the (0 4 0) charge peak (at the same azimuth angle) to reduce systematic errors. At an azimuth angle  $\psi = 90^\circ$ , where the **a-b** plane is coincident with the scattering plane, the integrated intensity is close to zero. We note that the intensity at  $\psi = 90^\circ$  is close to zero over the entire temperature range investigated in this experiment (from 8 K to

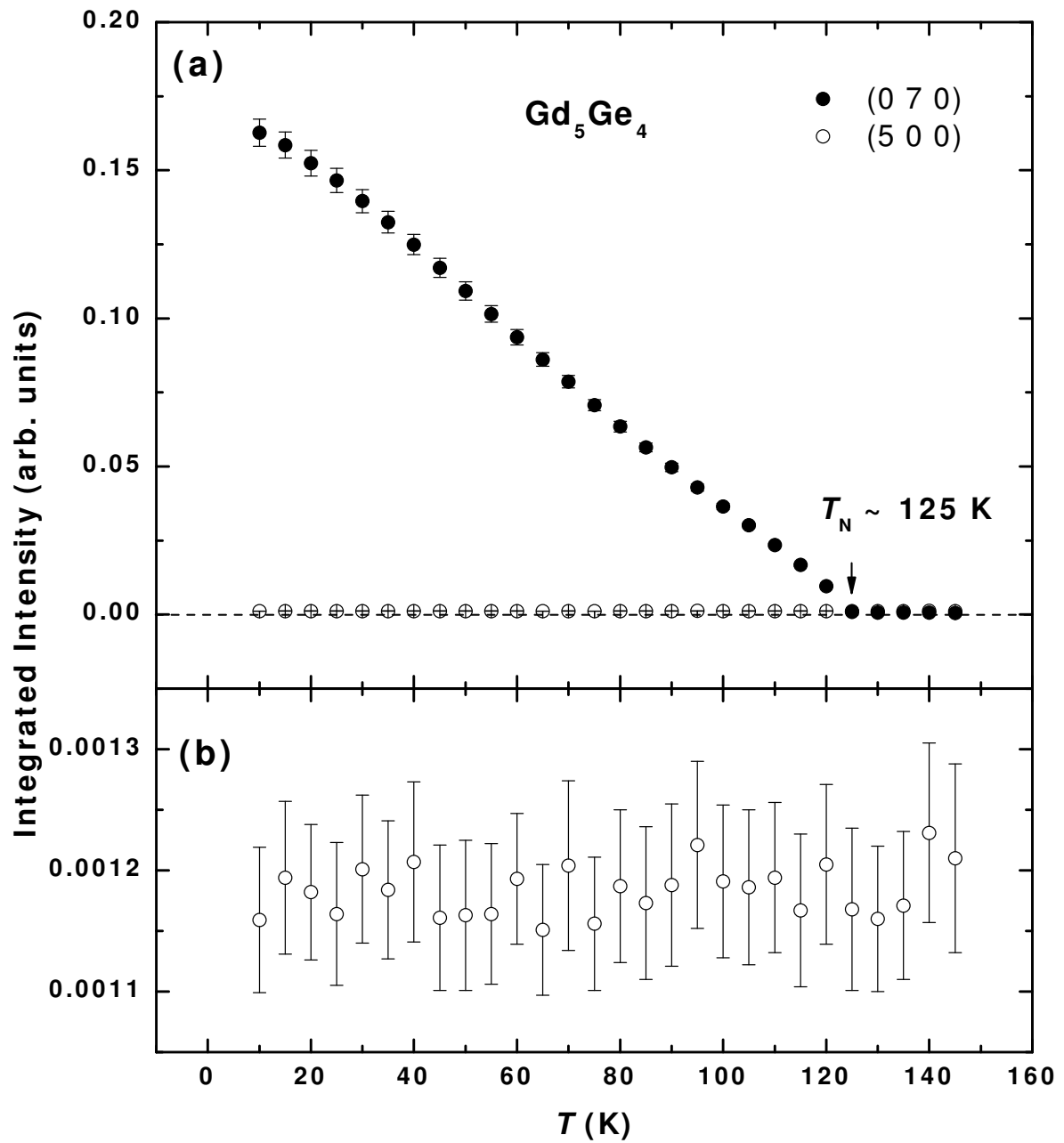


Figure 4.3 (a) Integrated intensity of the  $(0\ 7\ 0)$  magnetic peak measured upon heating the sample, at an azimuth angle of  $\psi = 30^\circ$ , using an aluminum attenuator with 0.41 transmission. (b) Integrated intensity of the  $(5\ 0\ 0)$  resonant peak measured during heating at an azimuth angle of  $\psi = 60^\circ$  without attenuator.

140 K). This indicates that there is no contribution to the scattering at this reflection from an **a** or **b** component of the magnetic moment. Two maxima are found at azimuth values of  $\psi = 0^\circ$  and  $180^\circ$  where the **b-c** plane is coincident with the scattering plane. Therefore, only the **c**-component contributes to the magnetic resonant scattering at this reflection.

The solid line in Fig. 4.4 represents the expected dependence,  $I = A \sin^2(\psi - \psi_c)$ , for the integrated intensity with  $\psi_c = (88.1 \pm 1.8)^\circ$ . The small deviation of  $\psi_c$  from  $90^\circ$  results from a slight misalignment of the sample. The intensity at  $\psi = 0^\circ$  deviates from the calculated curve because of particularly strong contributions from multiple scattering. Fig. 4.4 indicates that either there is no magnetic moment component along **a** or **b**, or the intensity of the (0 3 0) magnetic peak is not sensitive to either the **a** or the **b** magnetic moment components due to cancellations arising from the symmetry of the magnetic order.

In order to determine the sensitivity of the magnetic reflections to different spatial components of the magnetic moment, we must look into the details of the possible magnetic space groups. For the  $\text{Sm}_5\text{Ge}_4$ -type structure with the crystallographic space group  $Pnma$ , eight magnetic space groups are possible [Ber68, SP78], and are listed in Table 3.4. Each magnetic space group yields relations among the components of the magnetic moments along the three crystallographic axes described by modes. These modes represent the sign sequence of the moment components of each ion, in each site, along a particular direction.

In Table 4.1 the magnetic modes for the  $4c$  and  $8d$  Wyckoff sites are listed along with the corresponding structure factors for magnetic diffraction. From here, we see that only one mode,  $A$ , for the  $4c$  site and two modes,  $R$  and  $A_B$ , for the  $8d$  sites can contribute to the magnetic intensity of (0  $k$  0) reflections. Selected (0  $k$  0) reflections were measured, and their integrated intensities are shown in Table 4.2. Since only a **c** component contribution to the magnetic scattering was found for all (0  $k$  0) reflections,

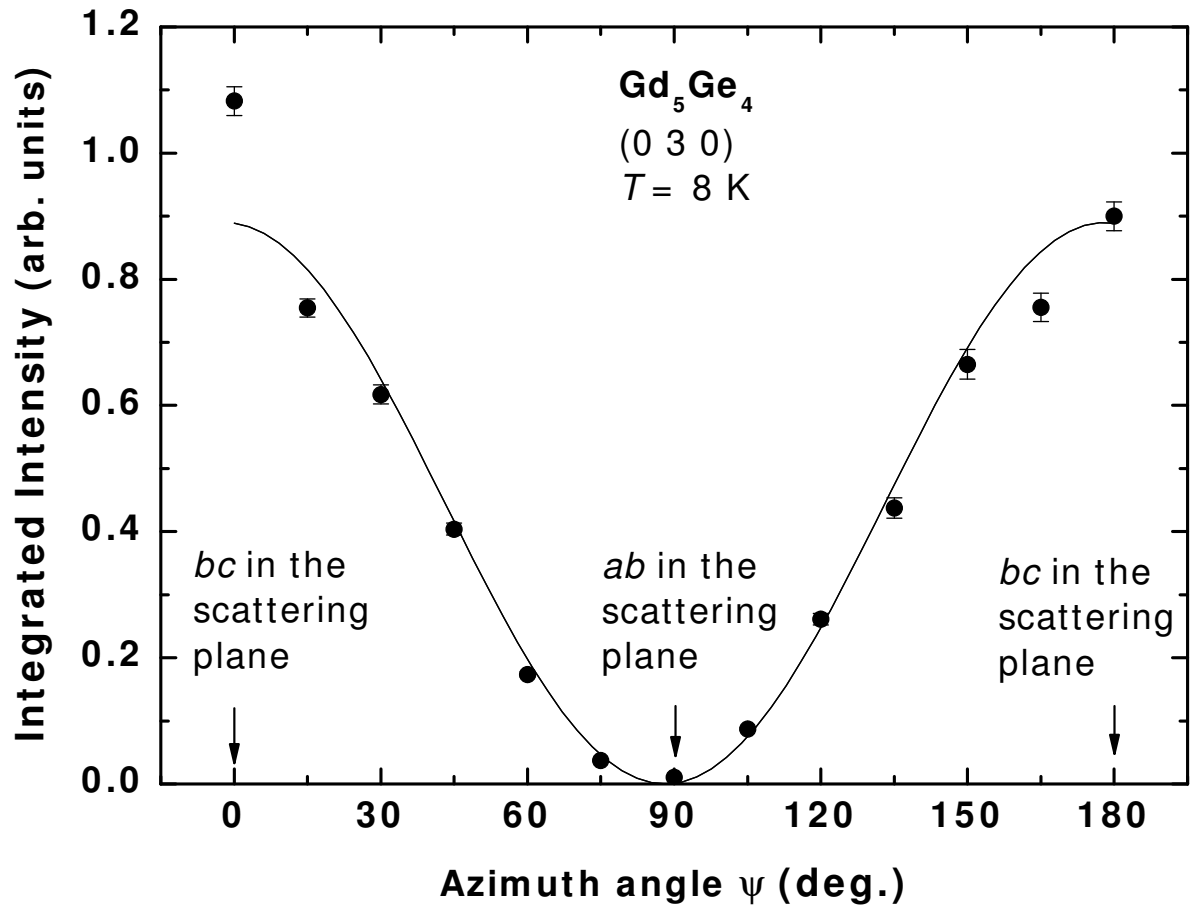


Figure 4.4 The integrated intensity of the (0 3 0) magnetic peak normalized by the (0 4 0) charge peak at  $T = 8$  K. The solid curve represents the variation expected for magnetic moments along the **c**-axis.

Table 4.1 Magnetic modes for the  $4c$  and  $8d$  Wyckoff sites, and their corresponding structure factors for the  $(h\ 0\ 0)$ ,  $(0\ k\ 0)$  and  $(0\ 0\ l)$  reflections ( $h, k, l$  are odd).  $x^{4c}, y^{4c}, z^{4c}$  and  $x^{8d}, y^{8d}, z^{8d}$  are the atomic positions and  $\mu_j^{4c}$  and  $\mu_j^{8d}$  are the magnetic moment components along the corresponding  $j$ -axis ( $j = a, b, c$ ) at the  $4c$  site and the  $8d$  sites respectively.)

mode	$(h\ 0\ 0)$	$(0\ k\ 0)$	$(0\ 0\ l)$
$A$	0	$i\mu_j^{4c}(-1)^{\frac{k-1}{2}}$	$-i\mu_j^{4c} \sin 2\pi lz^{4c}$
$C$	$\mu_j^{4c} \cos 2\pi hx^{4c}$	0	$\mu_j^{4c} \cos 2\pi lz^{4c}$
$F$	0	0	0
$G$	$-i\mu_j^{4c} \sin 2\pi hx^{4c}$	0	0
$A_B$	0	$2\mu_j^{8d} \cos 2\pi ky^{8d}$	0
$C_B$	0	0	0
$F_B$	0	0	0
$G_B$	$2\mu_j^{8d} \cos 2\pi hx^{8d}$	0	$2\mu_j^{8d} \cos 2\pi lz^{8d}$
$L$	$-2i\mu_j^{8d} \sin 2\pi hx^{8d}$	0	0
$P$	0	0	0
$Q$	0	0	0
$R$	0	$-2i\mu_j^{8d} \sin 2\pi ky^{8d}$	$-2i\mu_j^{8d} \sin 2\pi lz^{8d}$

only modes for the **c**-component must to be considered for  $(0\ k\ 0)$  reflections. We note that in general, all three Wyckoff sites need not be in the same magnetic space group with the same corresponding modes [Ber68]. Considering all possible combinations, in our case, there can be 17 different descriptions of the intensities for  $(0\ k\ 0)$  reflections. All cases were checked by comparing the measured integrated intensities of the  $(0\ k\ 0)$  reflections with the structure factors calculated from Table 4.1. For example, if all three sites are described by the same magnetic space group  $Pnm'a$ , only the **c**-components in the  $A$  mode at the  $4c$  site and the  $R$  mode at the two  $8d$  sites contribute to the intensity of the magnetic  $(0\ k\ 0)$  reflections according to:

$$I = A \sin^2(\psi - \psi_c) \frac{\cos^2 \theta}{\sin 2\theta} \left| (-1)^{\frac{k-1}{2}} \mu_c^{4c} + 2\mu_c^{8d_1} \sin 2\pi k y^{8d_1} + 2\mu_c^{8d_2} \sin 2\pi k y^{8d_2} \right|^2 \quad (4.1)$$

Here,  $A$  is the scaling factor,  $\psi$  is azimuth angle, and  $\theta$  is half of the scattering angle. Additionally,  $\cos^2 \theta / \sin 2\theta = \frac{\sqrt{1 - (\frac{k\lambda}{2b})^2}}{\frac{k\lambda}{2b}}$ , where  $\lambda$  is the wavelength of the incident photons,  $b$  is the lattice constant, and  $y^{8d_1} = 0.1022$  and  $y^{8d_2} = 0.1168$  for  $T = 6\text{ K}$  [PHGR03].

For all 17 cases the calculated integrated intensity was fit to the measured data with two dependent parameters  $\mu_c^{8d_1}/\mu_c^{4c}$  and  $\mu_c^{8d_2}/\mu_c^{4c}$  and an overall scaling factor  $A(\mu_c^{4c})^2$ . The best fit to the data, shown in Table 4.2 corresponds to all three magnetic Gd sites described by the same magnetic space group,  $Pnm'a$ . The resulting ratios  $\mu_c^{8d_1}/\mu_c^{4c} = 0.98 \pm 0.03$  and  $\mu_c^{8d_2}/\mu_c^{4c} = 0.99 \pm 0.04$  indicate equal magnetic moment components along the **c**-axis at the three Wyckoff sites. An important result of this analysis is that the absence of intensity at the  $(0\ 3\ 0)$  reciprocal lattice point at azimuth  $\psi = 90^\circ$  does not require the absence of **a** or **b** components of the magnetic moment but, rather, arises from the magnetic space group symmetry. A second consequence of this analysis is that no **b**-component of the magnetic moment is allowed for the  $4c$  site (see Table 3.4).

Table 4.1 also provides us with a means of investigating whether there is a compo-

Table 4.2 The measured and calculated (from Eqn. 4.1) values of the integrated intensity of  $(0\ k\ 0)$  reflections at  $T = 6$  K.

$k$	Measured intensity	Calculated Intensity
3	$0.123 \pm 0.002$	0.123
5	$0.0045 \pm 0.0003$	0.00021
7	$0.186 \pm 0.006$	0.186
9	$0.0028 \pm 0.0002$	0.0029
11	$0.0248 \pm 0.0008$	0.0249
13	$0.0221 \pm 0.0009$	0.0221

ment of the magnetic moment along the  $\mathbf{a}$ -axis through measurements of the magnetic scattering at the  $(h\ 0\ 0)$  lattice points ( $h$  odd). At these reflections, only the component of the moment along the  $\mathbf{a}$ -axis contributes to the scattering according to modes  $G$  and  $L$  in the magnetic space group  $Pnm'a$ . Because the  $\mathbf{a}$ -component is parallel to the scattering vector,  $\mathbf{Q}$ , for  $(h\ 0\ 0)$  reflections, the integrated intensities are not dependent upon the azimuth angle  $\psi$ . The  $(h\ 0\ 0)$  reflections with  $h = 1, 3, 5,$  and  $7$  were measured at the Gd  $L_{II}$  absorption edge. At  $T = 10$  K, the resonant intensities are too weak to be separated from multiple scattering, except at the  $(5\ 0\ 0)$  reflection as shown in Fig. 3.4. Surprisingly, although weak resonant scattering was indeed observed for the  $(5\ 0\ 0)$  reflection, no temperature dependence of its intensity was observed, even above the Néel temperature, as shown in Fig. 4.3 (b). Therefore, this resonant scattering does not arise from magnetic scattering related to the magnetic order below  $T_N$ . We believe this resonant contribution arises from Templeton scattering [TT94, FSS92], perhaps originating from long-range ordering of anisotropic charge distributions. Further investigations of this feature are planned.

Any magnetic scattering signal at the  $(5\ 0\ 0)$  reflection must be very small. Furthermore, no significant resonant scattering was found at the  $(1\ 0\ 0)$ ,  $(3\ 0\ 0)$ , or  $(7\ 0\ 0)$  positions. These results suggest that there is no  $\mathbf{a}$ -component of the magnetic moments.

Although we can not exclude small **a**-components for the magnetic moments on the  $4c$  and  $8d$  sites based on only four reflections, specific features of the crystallographic structure may be used to obtain additional constraints on the **a**-components. For example, in  $\text{Tb}_5\text{Ge}_4$ , there is no **a**-component of the moment at the  $4c$  site while sizable **a**-components were identified for both  $8d$  sites [SP78, RMA<sup>+</sup>02]. This most likely arises from the environment of the  $4c$  sites in the structure. In both slabs shown in Fig. 2.3, each Gd ion at the  $4c$  site is located at the center of a deformed cube with 4 Gd ions at the  $8d_1$  site and 4 Gd ions at the  $8d_2$  site at the corners [SP78]. This can result in a near compensation of the **a**-component of the exchange field at the  $4c$  sites by the surrounding 8 Gd ions for the  $Pnm'a$  magnetic space group. If we assume that for  $\text{Gd}_5\text{Ge}_4$  no **a**-component of the moment exists at the  $4c$  site, then the upper limits for  $\mu_a^{8d_1}$  and  $\mu_a^{8d_2}$  are determined to be  $0.06\mu_c$  and  $0.05\mu_c$ , respectively, from the constraints given by the measured  $(h\ 0\ 0)$  reflections.

Unfortunately, the **b**-components of the magnetic moment contribute only to the magnetic intensity of charge forbidden, off-specular  $(h\ k\ 0)$  and  $(0\ k\ l)$  reflections. Therefore, no direct information concerning the **b**-component can be obtained. For the  $(h\ k\ 0)$  reflections, the magnetic structure factors arise from linear combinations of the **a**- and **b**-components, while for the  $(0\ k\ l)$  reflections both the **b**- and **c**-components contribute. A complicating factor in the analysis of these reflections is that, in both cases, the entanglement of magnetic components for two different crystallographic directions introduces magnetic domains whose populations strongly influence the intensity of the magnetic reflections. While we have shown above that there is no **b**-component of the magnetic moment at the  $4c$  site, it is extremely difficult to unambiguously determine the presence or absence of the magnetic components  $\mu_b^{8d_1}$  and  $\mu_b^{8d_2}$  with the limited number of accessible magnetic reflections. However, if we assume that the magnitudes of the magnetic moment at all sites are the same,<sup>1</sup> the result that  $\mu_c^{8d_1}/\mu_c^{4c} = 0.98 \pm 0.03$  and

---

<sup>1</sup>Resonant scattering at the L-edges of rare earths involves transitions from the 2p core states to the

$\mu_c^{8d_2}/\mu_c^{4c} = 0.99 \pm 0.04$  (see above) allows us to postulate that the magnetic moments lie primarily along the **c**-axis for all three sites.

Summarizing, this XRMS experiment on the  $\text{Gd}_5\text{Ge}_4$  system has shown that, below the Néel temperature,  $T_N = 127$  K, the antiferromagnetic order is described by a magnetic unit cell which is the same as the crystallographic unit cell. As proposed by Levin et al.,[LGL<sup>+</sup>04]the magnetic moments are ferromagnetically aligned within the slabs, while their stacking in the **b**-direction is antiferromagnetic. Furthermore, all Gd sites order within the same magnetic space group,  $Pnm'a$ . The magnetic moments are primarily aligned along the **c**-axis and the **c**-components of the magnetic moments at the 3 different sites are the same within the error. Within experimental error, no **a**-component of the magnetic moments was detected. While a **b**-component of the moment at the 4c site can be excluded by the symmetry of the space group, the presence of a **b**-component of the moment at the 8d sites could not be unambiguously determined.

## The Unusual Order Parameter in $\text{Gd}_5\text{Ge}_4$ in Zero Field

If we look at Fig. 4.3 (a) carefully, we see the concavity of the curve in the intermediate temperature range. This feature is very unusual. The integrated intensity of Bragg reflection is generally proportional to the square of sublattice magnetization,  $M$ . If the sublattices magnetization follows the power law  $M \propto (T_c - T)^2\beta$ , then the plot of the temperature dependence of the integrated intensity should be convex. Here,  $T_c$  is the critical temperature and  $\beta$  is the critical exponent. ( $0 < \beta \leq 1/2$ ) Even if  $M$  follows a mean field behavior, the plot of  $I$  v.s.  $T$  should be a straight line. In order to explain the unusual temperature dependence, we need a second order parameter. For

---

unoccupied 5d states. The magnitude of the resonant scattering is largely determined by the matrix element of the transitions which, in turn, depends upon the size of the exchange interaction between the 4f and 5d electrons. Therefore, at least for Gd where the 4f-5d exchange interaction is large, the resonant scattering signal is closely related to the size of the 4f moment. While theoretical calculations show that the Gd moment at the 4c site is  $\sim 1\%$  larger than those at the two 8d sites,[PPGH07] the accuracy of our results is not sufficient to confirm this small difference.

example, it was reported that there is a spin reorientation transition in  $\text{Tb}_5\text{Ge}_4$  in zero field [RMA<sup>+</sup>02]. It is a reasonable speculation that a similar spin reorientation transition could occur in  $\text{Gd}_5\text{Ge}_4$ . Let us review first the spin reorientation transition in  $\text{Tb}_5\text{Ge}_4$ .

## Spin Reorientation in $\text{Tb}_5\text{Ge}_4$ in Zero Field

### The Bulk Measurements of $\text{Tb}_5\text{Ge}_4$

Single crystals of  $\text{Tb}_5\text{Ge}_4$  for the magnetization and XRMS measurements were grown using the Bridgman technique. The sample was extracted from the ingot, prepared with cut surfaces perpendicular to the crystallographic axes with a size of approximately 2 mm×2 mm×2 mm. The temperature dependence of the magnetization of the  $\text{Tb}_5\text{Ge}_4$  single crystal was measured with a Quantum Design SQUID magnetometer and is shown in Fig. 4.5. The zero-field cooled  $M(T)$  curves measured along the three principal crystallographic axes of  $\text{Tb}_5\text{Ge}_4$  in a magnetic field,  $H = 1$  kOe. These data clearly show an antiferromagnetic transition at  $T_N(\text{Tb}) = 92$  K, and indicate that the magnetic moment direction is likely mainly along the **c** axis since  $\chi_c$  decreases most closely to zero as temperature decreases to the base temperature. The temperature dependence of the reciprocal magnetic susceptibility ( $H/M$ ) follows Curie-Weiss behavior above  $\sim 160$  K (see inset of Fig. 4.5.) The different intercepts of the Curie-Weiss lines of the three principal crystallographic axes represent the anisotropy in the paramagnetic state. The difference is negligible between the **a** axis and the **c** axis in the paramagnetic state. The **b** axis is the hard axis in the paramagnetic state. At lower temperature  $\sim 55$  K, a kink in the magnetization curve of all three crystallographic axes, are clearly visible marked with a dashed line in Fig. 4.5, suggesting a further change in the magnetic structure.

The single crystal of  $\text{Tb}_5\text{Ge}_4$  for the electrical resistivity measurements had the dimensions 1 mm × 2 mm × 2 mm. Electrical connections to the sample were made by attaching thin platinum wires using silver paste. The dc electrical resistance measure-

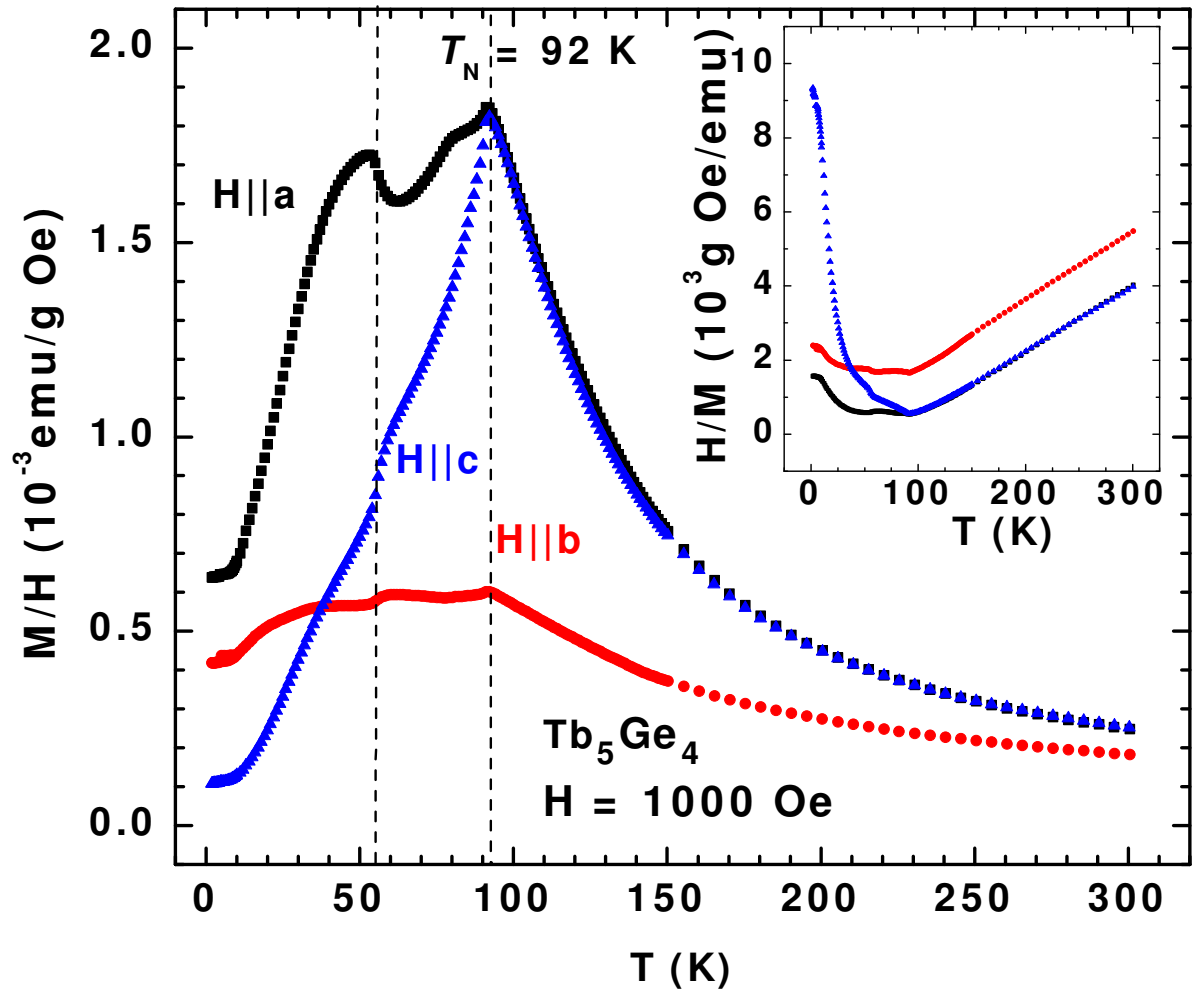


Figure 4.5 Magnetic susceptibility  $M/H$  of the  $\text{Tb}_5\text{Ge}_4$  single crystal. The temperature dependence of the susceptibility was measured on heating of the zero-field cooled sample in a field of 1000 Oe applied parallel to the three crystallographic axes.

ments were carried out using a Quantum Design SQUID magnetometer equipped with a probe for making four-point measurements. The measurements were performed at a constant dc electrical current of 5 mA in a temperature range from 5 to 300 K in zero magnetic field.

The temperature dependence of the electrical resistivity of  $\text{Tb}_5\text{Ge}_4$ , measured by S. Jia on cooling between 5 and 300 K with current along  $\mathbf{b}$  axis, is shown in Fig. 4.6. The electrical resistivity exhibits the low-temperature metallic and the high-temperature semiconductor-like behaviors, and shows a well-defined peak at 92 K. The change in slope of the resistivity curve at  $\sim 55$  K, with the electrical current applied along  $\mathbf{b}$  axis, is same as the second characterized temperature found in magnetization measurement. This also suggests a further change in the magnetic structure which changes the slope of the resistivity curve in consequence.

### **The XRMS Measurements of $\text{Tb}_5\text{Ge}_4$**

The XRMS experiment was performed on the 6ID-B beamline in the MUCAT sector at the Advanced Photon Source at the Tb  $L_3$  absorption edge ( $E = 7.517$  keV). The incident radiation was linearly polarized perpendicular to the vertical scattering plane ( $\sigma$ -polarized) with a spatial cross-section of 1 mm (horizontal)  $\times$  0.2 mm (vertical). In this configuration the resonant magnetic scattering, arising from electric dipole transitions ( $E1$ , from the  $2p$ -to- $5d$  states), rotates the plane of linear polarization into the scattering plane ( $\pi$ -polarization). In contrast, charge scattering does not change the polarization of the scattered photons ( $\sigma$ - $\sigma$  scattering). Pyrolytic graphite PG (0 0 6) was used as a polarization analyzer to suppress the charge background relative to the magnetic scattering signal. the sample was mounted on the end of the cold-finger of a displax cryogenic refrigerator with the crystallographic  $\mathbf{b}$ -axis parallel to the axis of the displax and set in the scattering plane. The multiple scattering contribution at the resonant energy can be minimized through a judicious choice of azimuth angle.

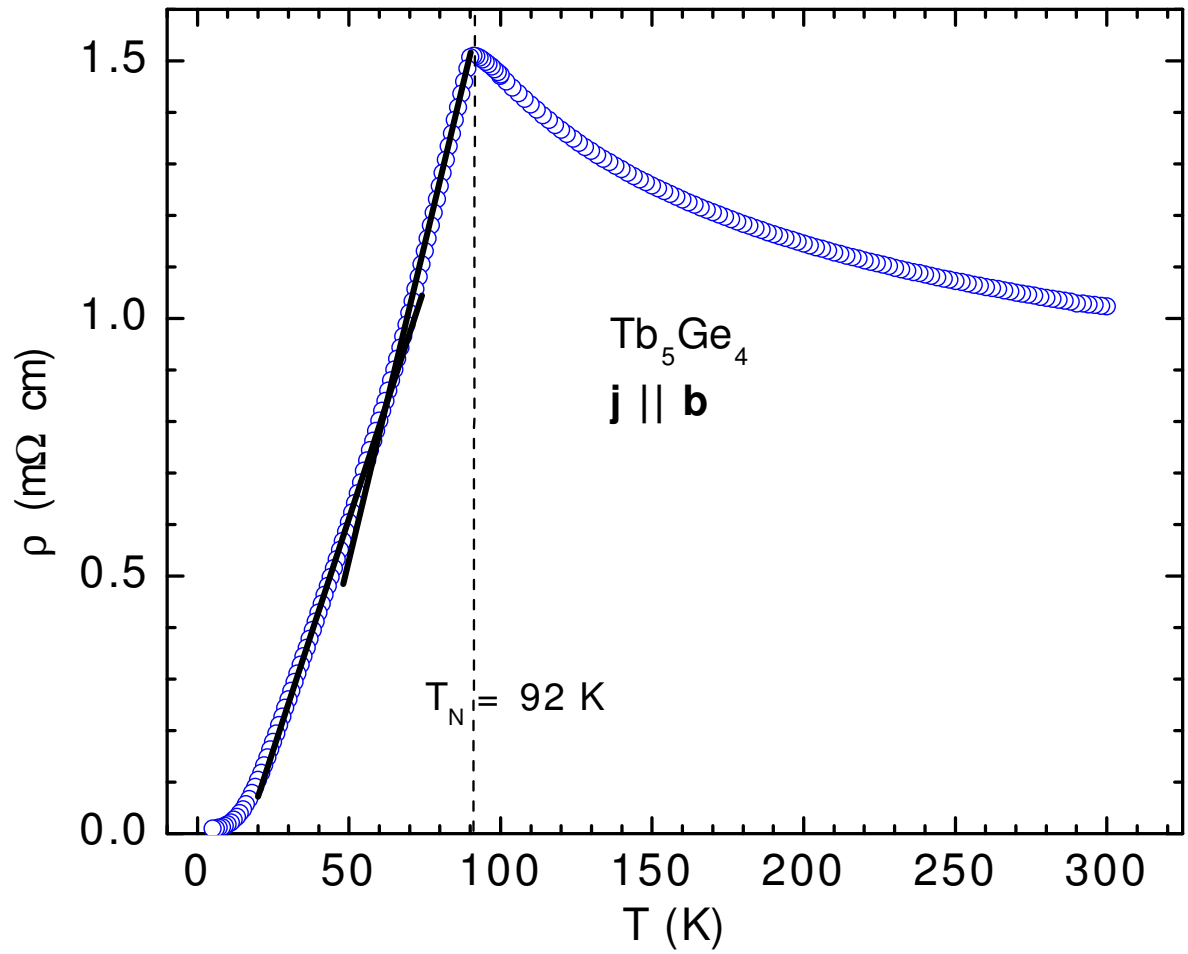


Figure 4.6 The temperature dependence of the electrical resistivity of the  $\text{Tb}_5\text{Ge}_4$  single crystal measured on heating up the sample with a current applied parallel to the  $\mathbf{b}$  axis. The solid lines are drawn to guide the eyes.

The sample was first cooled to 6 K. Reciprocal lattice scans, from (3 0 0) to (4 0 0), from (4 0 0) to (4 1 0), and from (4 0 0) to (4 0 1), were done to search for any satellite peak signaling a change in magnetic structure. Magnetic reflections were found only at reciprocal lattice points  $(h k l)$ , where  $h$ ,  $k$ , and  $l$  are integers. Therefore, the magnetic unit cell is same as crystallographic unit cell.

Fig. 4.7 shows the temperature dependence of the integrated intensity of the (0 7 0) magnetic peak. A Lorentzian peak shape was used to fit  $\theta$ -scans through the reciprocal lattice points to obtain the integrated intensities. The intensity decreases to zero as temperature increases up to  $T_N(\text{Tb}) = 92$  K. A kink found at  $T_{\text{sr}}(\text{Tb}) \sim 55$  K, is the same temperature as the anomaly in the magnetization curves and the resistivity curve. We also point out here that the temperature dependence of the integrated intensities shown in Fig. 4.7 is different from that of the (0 1 0) magnetic reflection obtained from the powder neutron scattering [RMA<sup>+</sup>02], which shows a smooth decrease in intensity, without any noticeable inflection up to the Néel temperature.

Due to the geometry limitation, we could not measure enough magnetic reflections to determine all three magnetic components at all three Tb sublattices. Here we use the results of the magnetic structure analysis from the neutron scattering measurements in Ref. [RMA<sup>+</sup>02].  $\text{Tb}_5\text{Ge}_4$  crystallizes in the  $Pnma$  orthorhombic space group. The atomic arrangement in  $\text{Tb}_5\text{Ge}_4$  is the same as in the isomorphic  $\text{Sm}_5\text{Ge}_4$  [SJT67] and  $\text{Gd}_5\text{Ge}_4$  [PG97c] compounds. Both the crystallographic space group and precise atomic arrangement remain unaltered upon cooling down to 6 K. The magnetic space group is same as that of  $\text{Gd}_5\text{Ge}_4$ ,  $Pnm'a$ , below  $T_N(\text{Tb}) = 92$  K. Analysis of magnetic reflections at base temperature leads to a complex canted-antiferromagnetic structure ( $T < T_{\text{sr}}$ ), which we note as low-temperature antiferromagnetic structure (i.e. LTAFM). The components of the Tb magnetic moments are listed in Table 4.3. The magnetic moments are essentially confined to the **ac** plane, the moments are mainly aligned along **c** axis. The Tb ions at 4c site (Tb1) form an almost collinear sublattice, the angle with the **c**

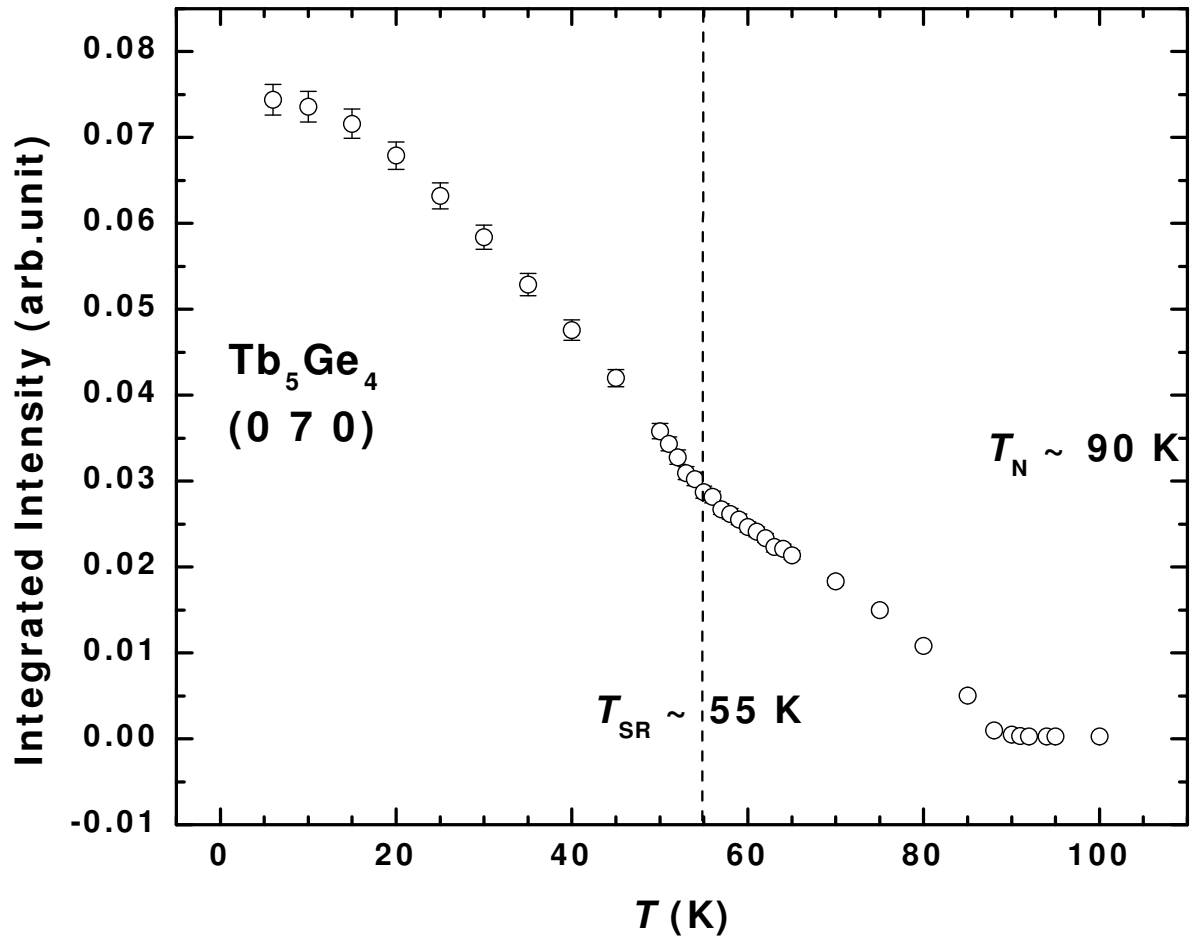


Figure 4.7 Integrated intensity of the (0 7 0) magnetic reflection measured upon heating the  $\text{Tb}_5\text{Ge}_4$  sample.

axis is about  $10^\circ$ . The canting angles of Tb ions at the  $8d_1$  (Tb2) and  $8d_2$  (Tb3) sites, with respect to  $\mathbf{c}$  axis, are larger,  $23^\circ$  and  $31^\circ$ , respectively. At 85 K ( $T_{\text{sr}} < T < T_{\text{N}}$ ), the magnetic moments cant along all three orthorhombic directions. The Tb1, Tb2, and Tb3 ions making canting angles with respect to  $\mathbf{c}$  axis of  $0^\circ$ ,  $7^\circ$ , and  $27^\circ$ , respectively. Therefore, a spin reorientation transition occurs on cooling at  $T_{\text{sr}}(\text{Tb}) = 55$  K from the high-temperature antiferromagnetic structure (HTAFM) to LTAFM.

Table 4.3 Components of the Tb magnetic moments for all of the studied  $\text{Tb}_5\text{Ge}_4$  compounds as determined from the Rietveld refinements of the D2B neutron powder diffraction data. (From Table III in Ref. [RMA<sup>+</sup>02])

T (K)	$\mu_{\text{Tb1}}(\mu_B)$			$\mu_{\text{Tb2}}(\mu_B)$			$\mu_{\text{Tb3}}(\mu_B)$		
	$\mu_x$	$\mu_y$	$\mu_z$	$\mu_x$	$\mu_y$	$\mu_z$	$\mu_x$	$\mu_y$	$\mu_z$
85	0	0	4.57(9)	0.3(2)	0.2(2)	3.0(1)	1.3(2)	1.0(2)	3.3(1)
2	1.49(8)	0	8.3(1)	2.7(1)	1.5(1)	7.06(8)	4.1(1)	1.8(2)	7.49(9)

## Spin Reorientation in $\text{Gd}_5\text{Ge}_4$ in Zero Field

### The Bulk Measurements of $\text{Gd}_5\text{Ge}_4$

The single crystal of  $\text{Gd}_5\text{Ge}_4$  for the electrical resistivity measurements had the dimensions  $1 \text{ mm} \times 2 \text{ mm} \times 2 \text{ mm}$ . Electrical connections to the sample were made by attaching thin platinum wires using silver paste. The dc electrical resistance measurements were carried out using a Quantum Design SQUID magnetometer equipped with a probe for making four-point measurements. The measurements were performed at a constant dc electrical current of 5 mA in a temperature range from 5 to 300 K in zero magnetic field.

The temperature dependence of the electrical resistivity of  $\text{Gd}_5\text{Ge}_4$ , measured by S. Jia on cooling between 5 and 300 K with currents along  $\mathbf{a}$  and  $\mathbf{b}$  axis, is shown in Fig. 4.8. The measurement on heating was made after the sample was slowly  $\sim 0.5$  K/min cooled

in the zero magnetic field. The electrical resistivity exhibits the low-temperature metallic and the high-temperature semiconductor-like behaviors, and shows a well-defined peak at 127 K. The result for single crystal measurement, with the electrical current applied along  $\mathbf{a}$  axis, is identical in shape to that measured on the polycrystalline sample reported in Ref. [LPGM01].. The change in slope of the resistivity curve with the electrical current applied along  $\mathbf{b}$  axis at  $\sim 75$  K, suggests a possible transition. Recalling that the magnetic moments modulate along  $\mathbf{b}$  axis in  $\text{Gd}_5\text{Ge}_4$  below the Néel temperature, this possible transition may result from the orientation change of magnetic moments.

### The XRMS Measurements of $\text{Gd}_5\text{Ge}_4$

The XRMS experiment was performed on the 6ID-B beamline in the MUCAT sector at the Advanced Photon Source at the Gd  $L_2$  absorption edge ( $E = 7.934$  keV). All other experimental setup is same as we described that for  $\text{Tb}_5\text{Ge}_4$ . The single crystal of  $\text{Gd}_5\text{Ge}_4$  for the XRMS measurements had the dimensions  $2 \text{ mm} \times 2 \text{ mm} \times 3 \text{ mm}$ . The sample was first cooled to 6 K. Reciprocal lattice scans, from  $(0 \ 4.05 \ 0)$  to  $(0 \ 5.1 \ 0)$ , from  $(-1.1 \ 10 \ 0)$  to  $(1.1 \ 10 \ 0)$ , and from  $(0 \ 10 \ -1.1)$  to  $(0 \ 10 \ 1.1)$ , were done to search for any satellite peak signaling a change in magnetic structure. Magnetic reflections were found only at reciprocal lattice points  $(h \ k \ l)$ , where  $h$ ,  $k$ , and  $l$  are integers. Therefore, the magnetic unit cell is same as crystallographic unit cell.

Fig. 4.3 (a) shows the temperature dependence of the integrated intensity of the  $(0 \ 7 \ 0)$  magnetic peak. A Lorentzian peak shape was used to fit  $\theta$ -scans through the reciprocal lattice points to obtain the integrated intensities. The intensity decreases gradually to zero as temperature increases up to  $T_N(\text{Gd}) = 125$  K.

In general, the integrated intensity  $I \propto M^2$ , where  $M$  is the magnitude of a magnetic moment i.e. the order parameter in an antiferromagnet. In consequence, the temperature dependence of the integrated intensity should be a convex curve or a straight line following the  $I(T) \propto (T - T_N)^{2\beta}$  relation below  $T_N$ , where  $\beta$  is a critical exponent and

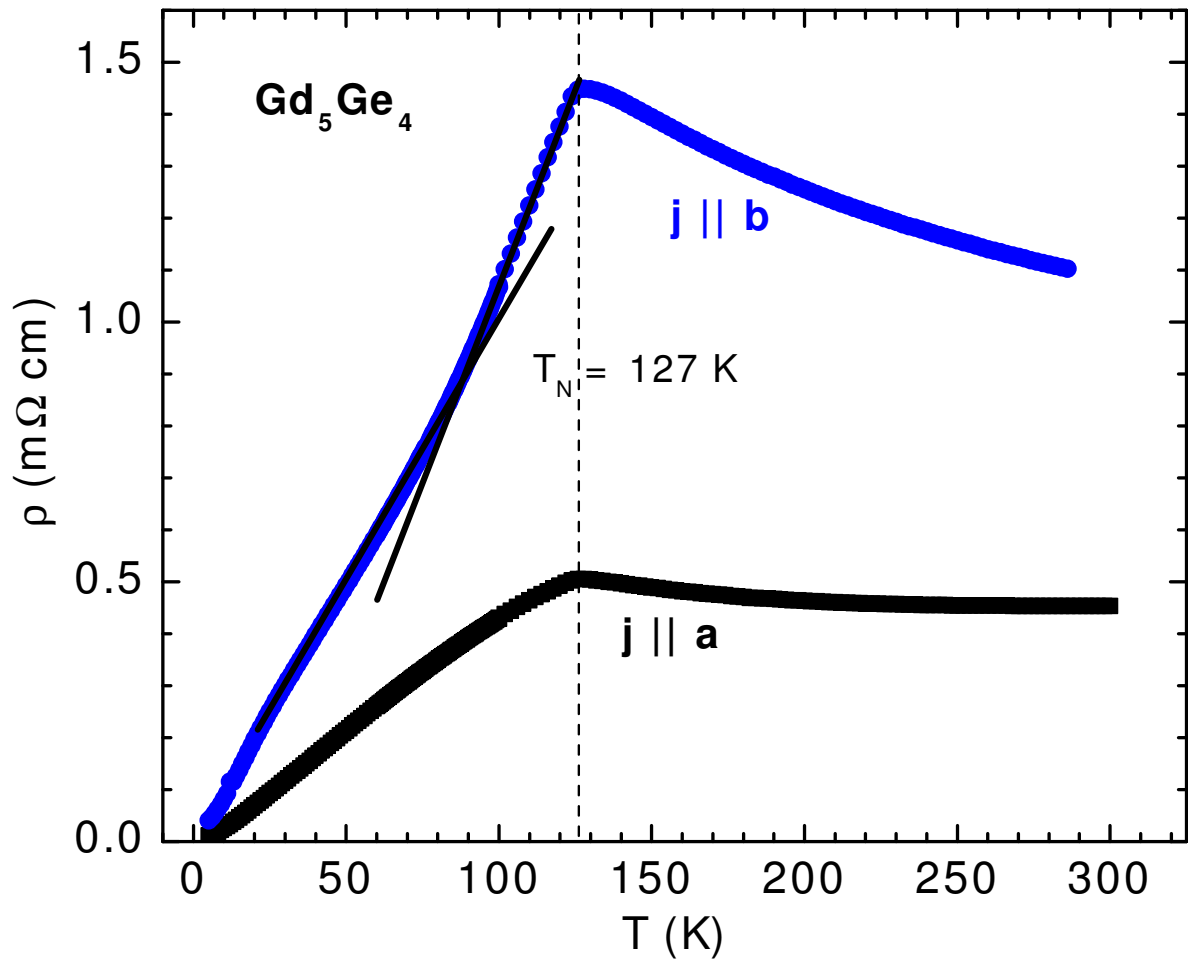


Figure 4.8 The temperature dependence of the electrical resistivity of the  $\text{Gd}_5\text{Ge}_4$  single crystal measured on heating up the sample with a current applied parallel to the **a** axis and **b** axis respectively. The solid lines are drawn to guide the eyes.

$0 < \beta \leq 0.5$ . Therefore, one unusual character of the curve is the concavity. The sample was heated upto 100 K. Reciprocal lattice scans from (0 4.05 0) to (0 5.1 0) were performed to investigate whether a new modulation appears in the resonant scattering between  $T_{\text{sr}}(\text{Gd})$  and  $T_{\text{N}}(\text{Gd})$ , but no additional wave vector could be located. Magnetic reflections were found only at reciprocal lattice points (0  $k$  0). Recalling Eq. 4.1, the concavity could be related to a spin-reorientation transition which slightly changes the **c** component of magnetic moments.

We can also derive the structure factor for ( $h$  0 0) magnetic reflections based on the magnetic space group of  $\text{Gd}_5\text{Ge}_4$ ,  $Pnm'a$ :

$$I = A \frac{\sin^2 \theta}{\sin 2\theta} \left| \mu_a^{4c} \sin 2\pi h x^{4c} + 2\mu_a^{8d_1} \sin 2\pi h x^{8d_1} + 2\mu_a^{8d_2} \sin 2\pi h x^{8d_2} \right|^2 \quad (4.2)$$

Here,  $A$  is the scaling factor and  $\theta$  is half of the scattering angle.  $h$  is odd. From Eq. 4.2, we see that ( $h$  0 0) magnetic reflections are sensitive to the **a**-components of magnetic moments. Although weak resonant scattering was indeed observed for the (5 0 0) reflection, no temperature dependence of its intensity was observed, even above the Néel temperature, as shown in Fig. 4.3 (b). This resonant scattering does not arise from magnetic scattering related to the magnetic order below  $T_{\text{N}}$ , but from anomalous charge scattering [TT94, FSS92]. Therefore, no change is observed in the **a** component of magnetic moments below  $T_{\text{N}}$ . If there is a spin-reorientation transition in  $\text{Gd}_5\text{Ge}_4$ , the magnetic moments should change the orientation within **bc** plane.

For (0 0  $l$ ) magnetic reflections, the integrated intensity is contributed by the **c** component of magnetic moments, as shown below:

$$I = A \frac{\sin^2 \theta}{\sin 2\theta} \left| \mu_c^{4c} \sin 2\pi l z^{4c} + 2\mu_c^{8d_1} \sin 2\pi l z^{8d_1} + 2\mu_c^{8d_2} \sin 2\pi l z^{8d_2} \right|^2 \quad (4.3)$$

Unfortunately, the **b**-components of the magnetic moment contribute only to the magnetic intensity of charge forbidden, off-specular ( $h$   $k$  0) and (0  $k$   $l$ ) reflections. For the ( $h$   $k$  0) reflections, the magnetic structure factors arise from linear combinations of the

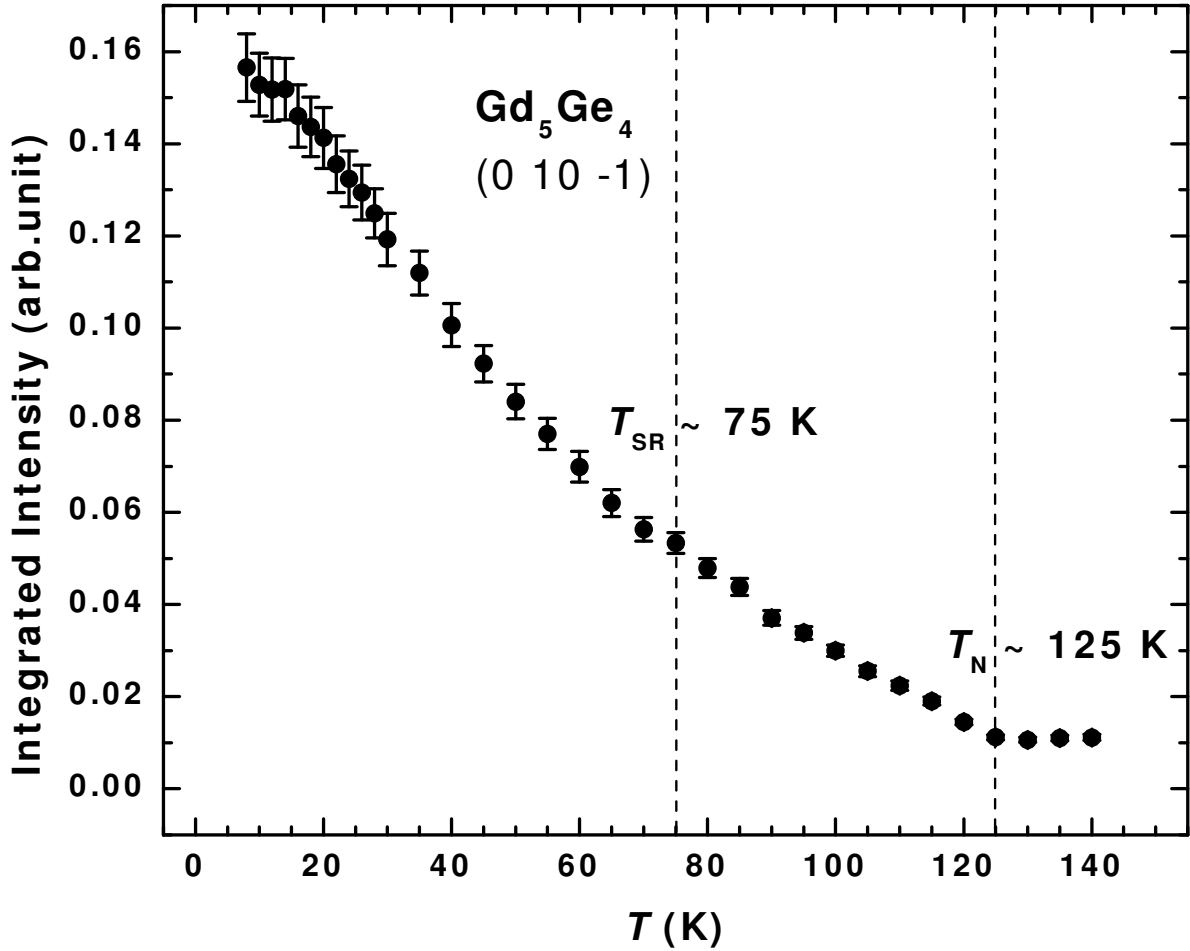


Figure 4.9 Integrated intensity of the (0 10 -1) magnetic reflection measured upon heating the  $Gd_5Ge_4$  sample.

**a**- and **b**-components, while for the (0  $k$   $l$ ) reflections both the **b**- and **c**-components contribute. We need large number of magnetic reflections measured to refine all parameters. Only a few reflections were measured due to the geometry limitation. No information concerning the **b**-component could be concluded directly.

Fig. 4.9 shows the temperature dependence of the integrated intensity of the (0 10 -1) magnetic peak. The intensity decreases to zero as temperature increases up to  $T = 125$  K. A kink found at  $T_{sr}(Gd) \sim 75$  K, is the same temperature as the anomaly in the resistivity curve with the electrical current applied along **b** axis shown in Fig. 4.8.

The data indicates that above  $T_{\text{sr}}(\text{Gd})$ , but still below  $T_{\text{N}}(\text{Gd})$ , the magnetic moments in  $\text{Gd}_5\text{Ge}_4$  might change their direction like what happens in  $\text{Tb}_5\text{Ge}_4$ .

Table 4.4 The measured and calculated values of the integrated intensity of  $\text{Gd}_5\text{Ge}_4$  (0  $k$  0) reflections at  $T = 90$  K.

$k$	Measured intensity	Calculated Intensity
3	0.0156(5)	0.01545
5	0.0016(4)	0.00002
7	0.030(2)	0.03035
9	0.0004(2)	0.00076
11	0.0019(1)	0.00280
13	0.0029(3)	0.00368

In order to determine the magnetic structure in both HTAFM phase and the LTAFM phase in  $\text{Gd}_5\text{Ge}_4$ , the integrated intensities of (0  $k$  0) reflections were measured at  $T = 6$  K and  $T = 90$  K. The data at  $T = 6$  K are listed in Table 4.2. We recall the conclusion from Chapter 4: the magnetic moments lie primarily along the  $\mathbf{c}$ -axis for all three sites and the magnitudes of the magnetic moment at all three Gd sites are the same at  $T = 6$  K within experimental error ( $\mu_c^{8d_1}/\mu_c^{4c} = 0.98 \pm 0.03$  and  $\mu_c^{8d_2}/\mu_c^{4c} = 0.99 \pm 0.04$  as shown in Table 4.5). The data at  $T = 90$  K are listed in Table 4.4. Considering all possible combinations of basis vectors at the three sites as shown in Table 3.4, the best fit to the data, as shown in Table 4.4, corresponds to all three magnetic Gd sites described by the same magnetic space group,  $Pnm'a$ . The fitting yields the ratios  $\mu_c^{8d_1}/\mu_c^{4c} = 0.71 \pm 0.13$  and  $\mu_c^{8d_2}/\mu_c^{4c} = 0.91 \pm 0.15$  as shown in Table 4.5. We conclude that, within error,  $\mu_c^{8d_1}$  is smaller than  $\mu_c^{4c}$  at  $T = 90$  K. We recall that the magnetic moments along  $\mathbf{c}$  axis are same size at the three Gd sites in the LTAFM phase and that no  $\mathbf{a}$  component of magnetic moments was observed in both the LTAFM and HTAFM phases of  $\text{Gd}_5\text{Ge}_4$ . Due to the symmetry constrain, there is no  $\mathbf{b}$  component of magnetic moments at  $4c$  site. If we assume that the magnitudes of the magnetic moment at all

sites are the same in the both phases,<sup>2</sup> the spin-reorientation transition from LTAFM to HTAFM in  $\text{Gd}_5\text{Ge}_4$  then corresponds to magnetic moments at  $8d_1$  and  $8d_2$  sites tilt slightly away from  $\mathbf{c}$  direction.

Table 4.5  $\mathbf{c}$ -component of the Gd magnetic moments as determined from  $(0\ k\ 0)$  reflections at  $T = 6$  K and  $T = 90$  K.

$k$	Measured intensity	Calculated Intensity
	$T = 6$ K	$T = 90$ K
$\mu_c^{8d_1}/\mu_c^{4c}$	0.98(3)	0.71(13)
$\mu_c^{8d_2}/\mu_c^{4c}$	0.99(4)	0.91(15)

## Discussion

Phase transitions are a common phenomenon encountered in nearly every branch of physics [SW72]. Magnetism, in particular, is a rich field in this regard due to the vector nature of the order parameter. Integral to this is the concept of magnetic anisotropy, i.e., the difference in energy for various orientations of the magnetization with respect to a sample. An understanding of spin reorientation transitions is an important source of knowledge regarding magnetic anisotropy. This information is invaluable because ab initio calculations of magnetic anisotropy energies in even the simplest systems are difficult [TJEW95], and it is currently not feasible to predict, from first principles, the behavior of complicated alloys and multilayered systems.

$\text{Tb}_5\text{Ge}_4$  possesses a same  $\text{Sm}_5\text{Ge}_4$ -type crystallographic structure and a same magnetic space group as  $\text{Gd}_5\text{Ge}_4$  does. The difference in magnetic structure is that  $\text{Tb}_5\text{Ge}_4$

<sup>2</sup>Resonant scattering at the L-edges of rare earths involves transitions from the 2p core states to the unoccupied 5d states. The magnitude of the resonant scattering is largely determined by the matrix element of the transitions which, in turn, depends upon the size of the exchange interaction between the 4f and 5d electrons. Therefore, at least for Gd where the 4f-5d exchange interaction is large, the resonant scattering signal is closely related to the size of the 4f moment. While theoretical calculations show that the Gd moment at the 4c site is  $\sim 1\%$  larger than those at the two 8d sites [PPGH07], the accuracy of our results is not sufficient to confirm this small difference.

has a canted one but  $\text{Gd}_5\text{Ge}_4$  has nearly a collinear one in LTAFM. The delicate competition between the magneto-crystalline anisotropies (due to crystalline electric field [CEF] effect and spin-orbit coupling) and the nearest-neighbor magnetic exchange interactions may allow a canted antiferromagnetic structure in 3-dimensional sublattice in  $\text{Tb}_5\text{Ge}_4$ .

In general, the spin-reorientation phenomena results from competing anisotropies in the system. In rare earth compounds, potential sources of magnetic anisotropy include contributions from single ion, dipolar, and exchange interactions. For most of the rare-earth elements with finite orbital moments, the single-ion anisotropy due to the CEF effect dominates the anisotropy of the magnetic ground state. However, the Gd-based antiferromagnets usually have insignificant anisotropy because the CEF effect are absent due to the half filled 4f-shells ( $L = 0$ ). Therefore, the spin-reorientation transition in  $\text{Gd}_5\text{Ge}_4$  can't arise from CEF effect. The dipolar interactions and the spin-orbit coupling of the conduction electrons may play a dominant role in the determination of preferred direction of magnetic moments in  $\text{Gd}_5\text{Ge}_4$ . As a result, the spin-reorientation transition in both  $\text{Gd}_5\text{Ge}_4$  and  $\text{Tb}_5\text{Ge}_4$  may arise from the delicate competition between the magnetic anisotropy from the spin-orbit coupling of the conduction electrons and the dipolar interactions anisotropy.

### **Magnetic Structure of $\text{Gd}_5\text{Si}_{0.33}\text{Ge}_{3.67}$ in Zero Field**

$\text{Gd}_5(\text{Si}_x\text{Ge}_{1-x})_4$  alloys have been extensively studied since the discovery of a giant magnetocaloric effect [PG97b, PG97d, PG97c, PG97a, PG98], whose origin lies in the large entropy change associated with the first-order magnetostructural transition. In these alloys, strongly interacting magnetic and non-magnetic ions are arranged in subnanometer-thick 2D slabs forming a 3D crystallographic framework. The interslab interactions in these naturally occurring nanolayered magnetic materials may

be controlled with a high precision by varying the stoichiometry i.e., the value of  $x$ . When  $0 \leq x \leq 0.2$ , a second-order PM-to-AFM transition occurs at the Néel temperature ( $127 \sim 134$  K) [PG97c, MBAI00]. Upon further cooling, a reversible first-order AFM-FM transition takes place, whose temperature  $T_C$  ranges linearly as shown in Fig. 2.1 [PG97d, PG97c]. The AFM-FM transition occurs simultaneously with a structural transition from a high-temperature  $\text{Sm}_5\text{Ge}_4$ -type orthorhombic [O(II)] phase to a low-temperature  $\text{Gd}_5\text{Si}_4$ -type orthorhombic [O(I)] phase [MBAI00]. As this transition shows a strong magnetoelastic coupling [CLB<sup>+</sup>04], it can be induced by the application of moderate magnetic fields [MBAI00]. The magnetostructural character of the transition can be understood through an examination of the layered crystal structure of  $\text{Gd}_5(\text{Si}_x\text{Ge}_{1-x})_4$ . For the O(I) phase, which is FM, 2D slabs are interconnected through Ge(Si)-Ge(Si) covalent-like bonds [CPP<sup>+</sup>00]. The interslab bonds are broken when the distance between all Ge(Si) atoms increases during the transformation to the O(II) phase, leading to AFM ordering [HLH<sup>+</sup>07].

The nature of the AFM ordering related to the O(II) phase [LGP02, MAM<sup>+</sup>03] is speculated to be similar to that of  $\text{Gd}_5\text{Ge}_4$ . However, in the case of  $\text{Gd}_5\text{Ge}_4$ , one could guess that a first order AFM-FM transition would occur at 20 K from Fig. 2.1. In fact, the magnetic ordering remains AFM with the O(II) structure after zero-field-cooling (ZFC) down to  $\sim 2$  K [LGP02, LPGM01]. An XRMS investigation of the magnetic structure of  $\text{Gd}_5\text{Si}_{0.33}\text{Ge}_{3.67}$ , the small doped Si compound, was carried on to see any interesting property around the discontinuity of the first order transition line near  $\text{Gd}_5\text{Ge}_4$  side on the phase diagram as shown in Fig. 2.1.

## Magnetization

Single crystals of  $\text{Gd}_5\text{Si}_{0.33}\text{Ge}_{3.67}$  were grown using the Bridgman technique. The sample for the magnetization measurement was extracted from the ingot with a size of approximately  $1 \text{ mm} \times 1 \text{ mm} \times 1 \text{ mm}$ . The crystal was oriented by back-reflection Laue

and the crystallographic directions assigned using x-ray diffraction two theta scans of the single crystal. The temperature dependence of the magnetization was measured with a low field of 100 Oe in a SQUID magnetometer and is shown in Fig. 4.10. These data clearly show an antiferromagnetic transition at  $T_N = 128$  K as we expected. (see the inset figure.) Upon further cooling, an AFM-FM transition occurs at  $T_C \sim 67$  K. Then the magnetization becomes saturated very quickly.

The field dependence of the magnetization was measured at  $T = 70$  K as shown in Fig. 4.11. The sample was cooled in zero field to 70 K (AFM state). Then the external magnetic field was applied along **a**-axis. The field was ramped up from 0 Tesla to 3 Tesla, and then back down to 0 Tesla. Next, the sample was cycled in an opposite field direction. The AFM-FM transition occurs at  $H_{cr} \sim 1$  Tesla. This shows that, the AFM-FM transition can also be induced by the application of moderate magnetic fields. The magnetic moments reach the saturation value of  $\sim 7.7\mu_B$ , which agree with the calculated values [PPGH07]. The two  $M(H)$  curves for increasing and decreasing magnetic field applied in **a** direction are very close to each other, showing that the field-induced AFM-FM transition has a small hysteresis.

### Magnetic Structure in Zero Field

For the XRMS measurements, a single crystal was extracted from the ingot and prepared with polished surfaces perpendicular to the crystallographic **a**- and **b**-axes, with a size of approximately 2 mm  $\times$  2 mm  $\times$  2 mm. The XRMS experiment was performed on the 6ID-B beamline in the MUCAT sector at the Advanced Photon Source at the Gd  $L_2$  absorption edge ( $E = 7.934$  keV). The incident radiation was linearly polarized perpendicular to the vertical scattering plane ( $\sigma$ -polarized) with a spatial cross-section of 1 mm (horizontal)  $\times$  0.2 mm (vertical). Pyrolytic graphite PG (0 0 6) was used as a polarization analyzer to suppress the charge background relative to the magnetic scattering signal. The sample was mounted on the end of the cold-finger of a displac-

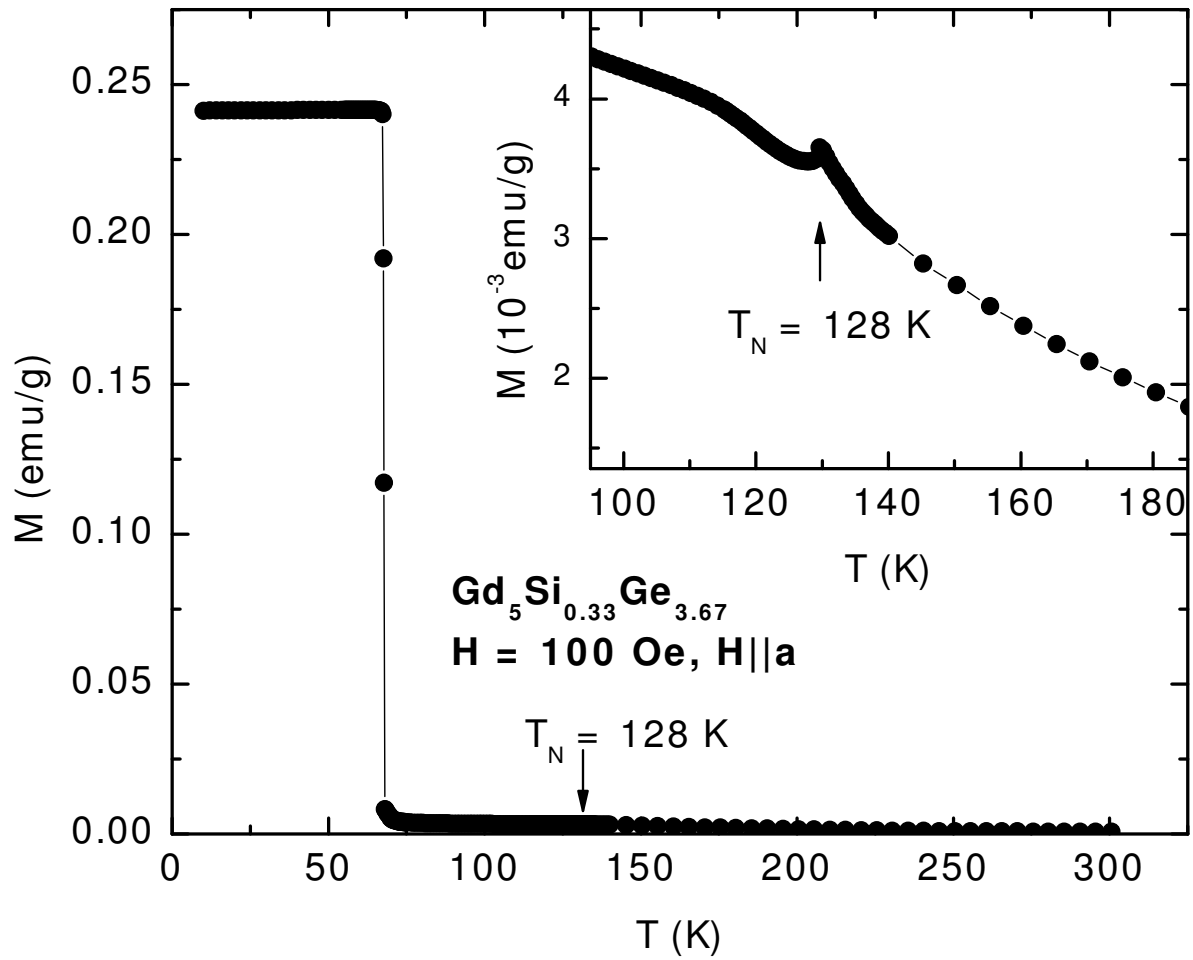


Figure 4.10 The field cooling of the single crystal of  $\text{Gd}_5\text{Si}_{0.33}\text{Ge}_{3.67}$  measured with the magnetic field vector parallel to the  $a$ -axis,  $H = 100$  Oe. Inset shows the magnetisation around the Néel temperature (labeled with an arrow).

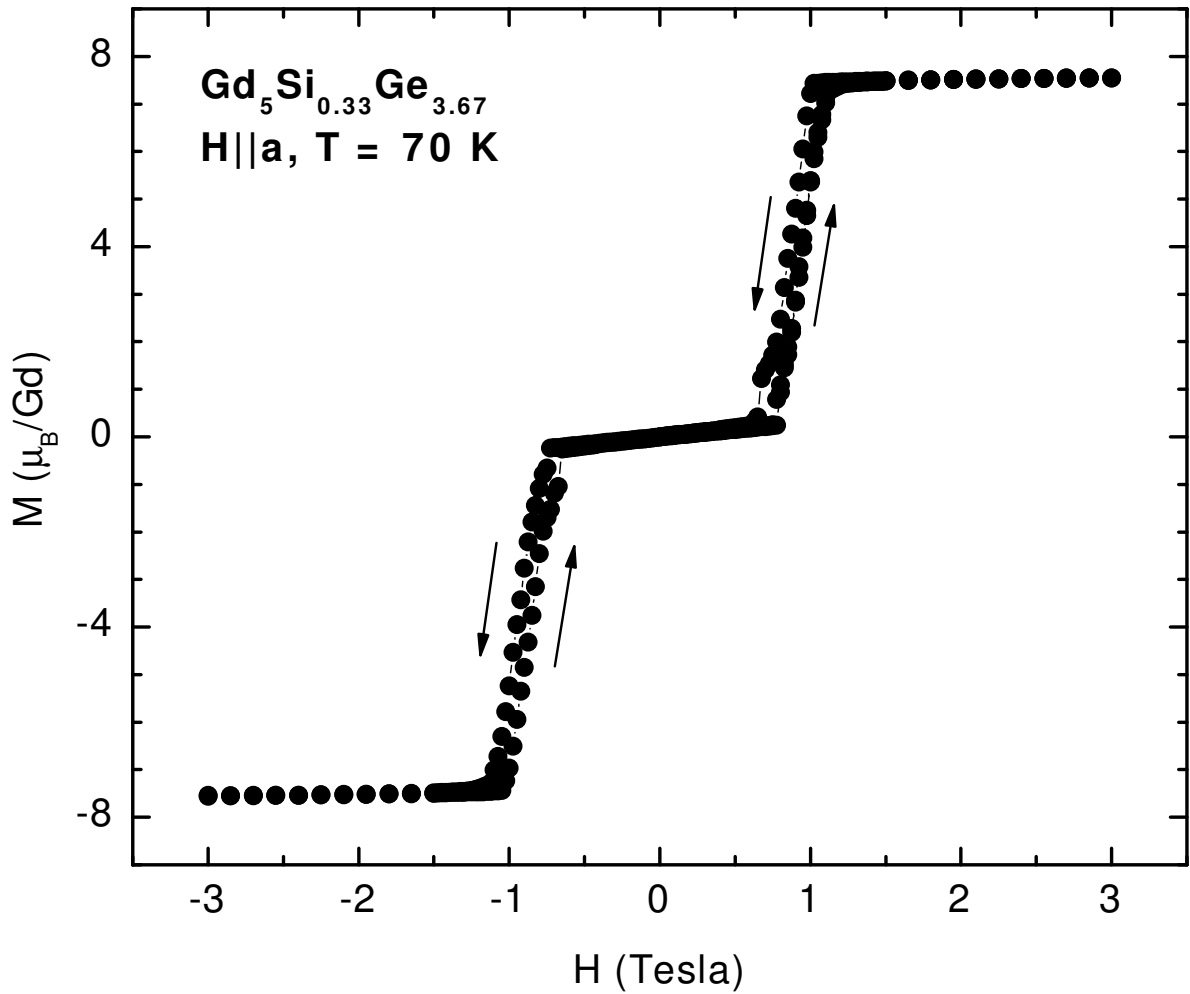


Figure 4.11 The magnetic field dependencies of the magnetization of the zero-field cooled single crystal of  $\text{Gd}_5\text{Si}_{0.33}\text{Ge}_{3.67}$  measured at  $T = 70\text{ K}$  when the magnetic field vector is parallel to the  $a$ -axis. The dashed lines show the extrapolated magnetic behavior without the magnetic field-induced AFM-FM transition during the second field-increasing measurement.

cryogenic refrigerator with the crystallographic **b**-axis parallel to the axis of the dispex and set in the scattering plane. As discussed before, the multiple scattering contribution at the resonant energy can be minimized through a judicious choice of azimuth angle.

The sample was first cooled to 80 K where the sample is antiferromagnetic. Reciprocal lattice scans along high symmetry direction  $(0\ k\ 0)$  were done to search for any satellite peak signalling a change in magnetic structure. Magnetic reflections were found only at reciprocal lattice points  $(0\ k\ 0)$ , where  $k$  is odd. Then the sample was heated up to 160 K, which is well above the Néel temperature, for a measurement of the temperature dependence of integrated intensities upon cooling. The  $(0\ 7\ 0)$  magnetic reflection and  $(0\ 8\ 0)$  charge reflection were measured at each temperature. Fig. 4.12 shows the temperature dependence of the integrated intensity of the  $(0\ 7\ 0)$  magnetic reflection. A Lorentzian peak shape was used to fit  $\theta$ -scans through the reciprocal lattice points to obtain the integrated intensities. The intensity started to increase at  $T_N(\text{Gd}) = 127$  K. A kink found at  $T_{\text{sr}} \sim 84$  K, is believed as a spin reorientation transition as discussed before. The integrated intensity of  $(0\ 7\ 0)$  continued to increase until the temperature reached 64.7 K. Then the magnetic reflection suddenly disappeared. The temperature for the AFM-FM transition,  $T_C = 64.7$  K is consistent with that in the magnetization measurement.

Fig. 4.12 shows the temperature dependence of the peak position of the rocking scans of the  $(0\ 8\ 0)$  charge reflection. A Lorentzian peak shape was used to fit  $\theta$ -scans through the reciprocal lattice points to obtain the corrected position. There is a significant change in the peak position at  $T_C = 64.7$  K. Therefore, the transition at  $T_C = 64.7$  K involves a strong magnetostrictive effect. Below  $T = 62$  K, no residual AFM signal is observed. This is a complete transition from AFM state to FM state.

In order to determine the magnetic structure in the AFM phase in  $\text{Gd}_5\text{Si}_{0.33}\text{Ge}_{3.67}$ , the integrated intensities of  $(0\ k\ 0)$  reflections were measured at  $T = 80$  K. The data at  $T = 80$  K are listed in Table 4.6. Considering all possible combinations of basis

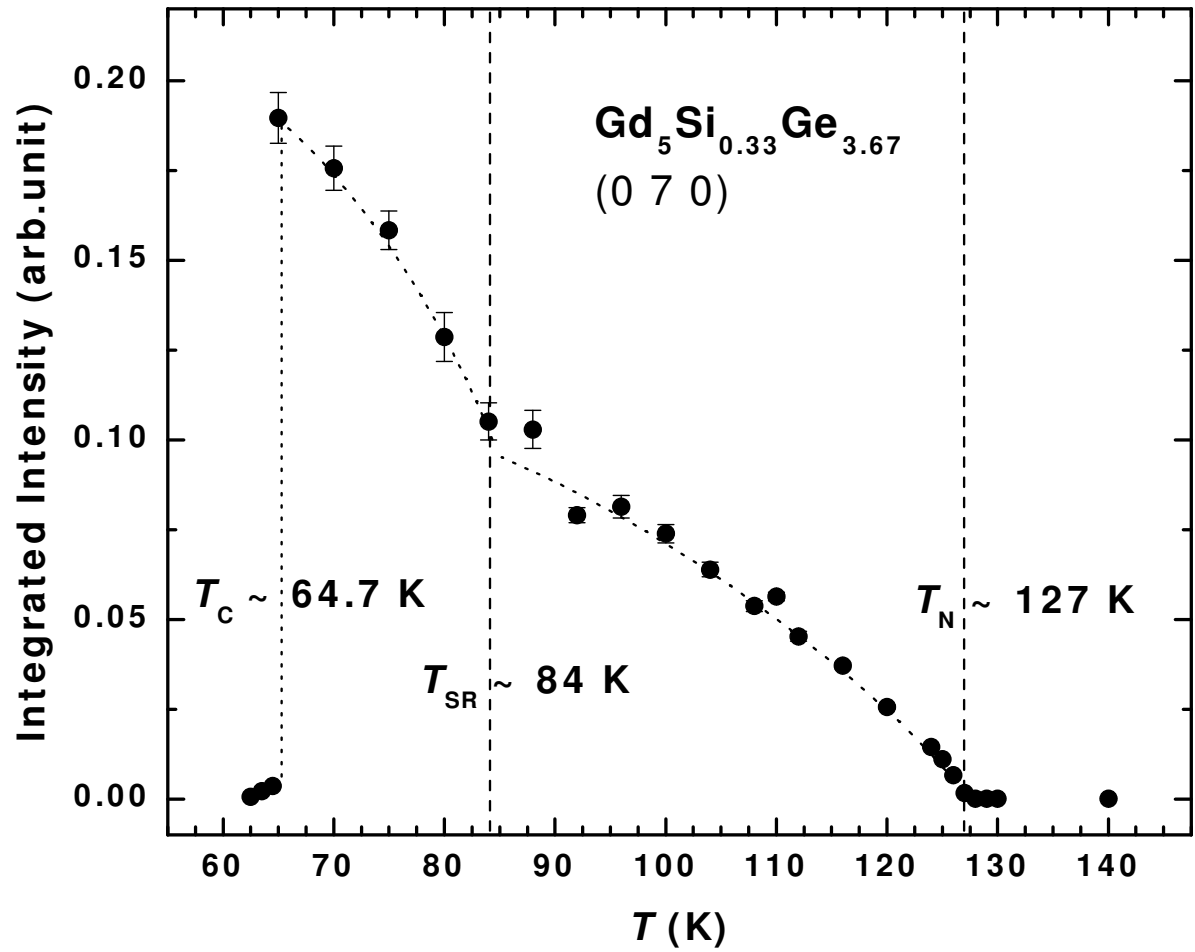


Figure 4.12 Integrated intensity of the (0 7 0) magnetic reflection measured upon heating the Gd<sub>5</sub>Ge<sub>4</sub> sample. The data is normalized by the (0 8 0) charge reflection. The dotted lines are drawn to guide the eyes.

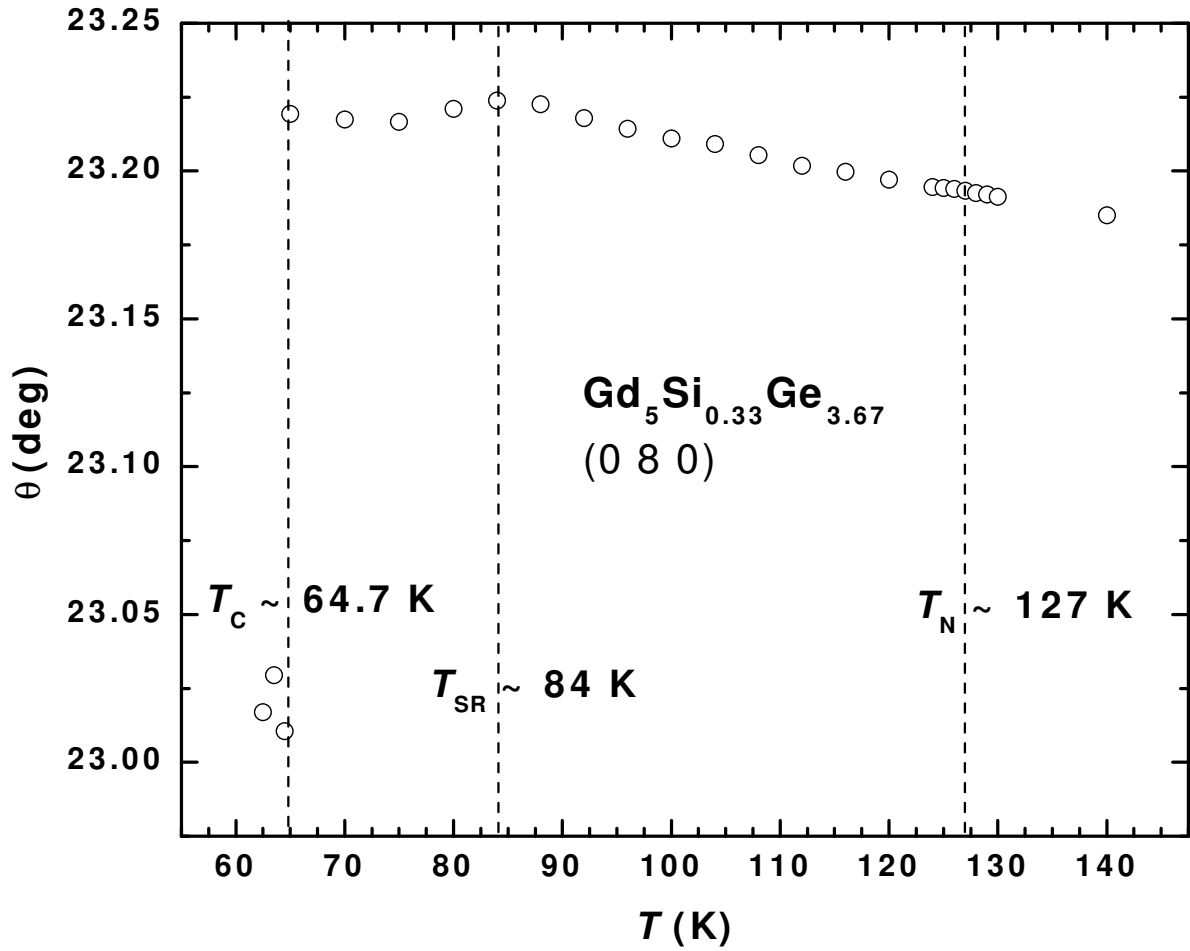


Figure 4.13 The peak position of the rocking scans of the (0 8 0) charge reflection measured upon heating the Gd<sub>5</sub>Ge<sub>4</sub> sample.

Table 4.6 The measured and calculated values of the integrated intensity of  $\text{Gd}_5\text{Si}_{0.33}\text{Ge}_{3.67}(0\ k\ 0)$  reflections at  $T = 80$  K.

$k$	Measured intensity	Calculated Intensity
3	0.0242(6).	0.0242
5	0.0004(2).	0.00001
7	0.0283(10)	0.0283
9	0.00062(10)	0.0002
11	0.00219(6).	0.00194
13	0.00304(10)	0.00280

vectors at the three sites as shown in Table 3.4, the best fit to the data, corresponds to all three magnetic Gd sites described by the same magnetic space group,  $Pnm'a$ . The fitting yields the ratios  $\mu_c^{8d_1}/\mu_c^{4c} = 1.16 \pm 0.04$  and  $\mu_c^{8d_2}/\mu_c^{4c} = 1.01 \pm 0.06$ . The magnetic structure of  $\text{Gd}_5\text{Si}_{0.33}\text{Ge}_{3.67}$  in the AFM phase is very similar to that of  $\text{Gd}_5\text{Ge}_4$ .

## Discussion

It is well-known that the indirect Ruderman-Kittel-Kasuya-Yosida (RKKY) 4f-5d-4f exchange interactions account for most of the magnetic phenomena observed in inter-metallic lanthanide systems, and it is certainly important in the  $\text{Gd}_5(\text{Si}_x\text{Ge}_{1-x})_4$  system. But RKKY may not be the only exchange interactions used to explain the mechanics of the drastic change in magnetic properties arising from the magnetostructural transition in  $\text{Gd}_5(\text{Si}_x\text{Ge}_{1-x})_4$  alloys. Levin et al [LPG00] firstly suggested that, beside the indirect RKKY 4f-5d-4f exchange, the Gd-Ge(Si)-Gd superexchange through the interslab covalent-like bonds also account for FM ordering in the O(I) structure.

There are some interesting theoretical findings, which help the understanding of mechanics of the magnetostructural transformation, published after our experiments. Paudyal et al have done the calculations for the total energy in  $\text{Gd}_5\text{Ge}_4$  by using the tight-binding linear muffin-tin orbital method within the exchange correlation parametrization

in the density functional theory [PPGH07]. Their calculations reveal that the O(II)-type  $\text{Gd}_5\text{Ge}_4$  has an antiferromagnetic ground state, whose total energy is lower than that of the ferromagnetic O(I)-type  $\text{Gd}_5\text{Ge}_4$ . This conclusion is in agreement with experiments. a first-order phase transformation between AFM O(II)  $\text{Gd}_5\text{Ge}_4$  and FM O(I)  $\text{Gd}_5\text{Ge}_4$  can be concluded from the behavior of the total energy versus shear perturbation [PPGH07]. While the interslab exchange coupling energy in the O(II)  $\text{Gd}_5\text{Ge}_4$  is lower than that of the O(I)  $\text{Gd}_5\text{Ge}_4$ , the FM 5d local exchange splitting of the Gd atoms in O(I)  $\text{Gd}_5\text{Ge}_4$  is larger than in the O(II)  $\text{Gd}_5\text{Ge}_4$  [PPGH07].

Haskel et al [HLH<sup>+</sup>07] applied X-ray magnetic circular dichroism (XMCD) measurements and density functional theory (DFT) to study the electronic conduction states in  $\text{Gd}_5(\text{Si}_x\text{Ge}_{1-x})_4$  materials through the first-order transition. The long-range RKKY ferromagnetic interactions between the localized Gd 4*f* moments in neighbor slabs, is transferred by the 4*p* band of the Ge atoms at interslab positions, which is hybridized with Gd 5*d* spin-dependent conduction states. The magnetic polarization of electrons in Gd 5*d* conduction band is transferred to the Ge sites through the orbital hybridization. The Ge(Si) bond-breaking transition, which destroys 3D ferromagnetic order, act as a trigger regulating the strength of interslab RKKY exchange coupling [HLH<sup>+</sup>07].

## CHAPTER 5. Spin-Flop Transition in $\text{Gd}_5\text{Ge}_4$

### Introduction

Gadolinium-based magnetic compounds typically exhibit only weak magnetoelastic effects [LR02]. However, strong magnetostriction has been observed in  $\text{Gd}_5(\text{Si}_x\text{Ge}_{1-x})_4$  alloys [MBAI00, MAI<sup>+</sup>98, CPP<sup>+</sup>00], where changes in the atomic positions and rearrangements of chemical bonds may be triggered by relatively weak applied magnetic fields. The magnetostrictive, magnetocaloric [PG97b, PG97d] and magnetoresistive [MSG<sup>+</sup>98, LPG99, LPGT00] effects are related to a first order magnetic transition, from either a paramagnetic or an antiferromagnetic phase to a ferromagnetic phase, accompanied by a martensitic-like structural change [TPGP04].

There have been several recent studies of the magnetic properties of  $\text{Gd}_5\text{Ge}_4$  single crystals [LGL<sup>+</sup>04, TKK<sup>+</sup>05, OPG<sup>+</sup>06]. The compound crystallizes in the orthorhombic space group  $Pnma$ , orders antiferromagnetically below 125 K, and remains antiferromagnetic (AFM) down to 2 K in the absence of an applied magnetic field [LPGM01]. This conclusion was supported by a diffraction study of the magnetic structure of a  $\text{Gd}_5\text{Ge}_4$  single crystal performed using x-ray resonant magnetic scattering [TKK<sup>+</sup>05]. In zero field, the magnetic unit cell is the same as the chemical unit cell. The magnetic order of the Gd moments can be described by the magnetic space group  $Pnm'a$  with magnetic moments aligned along the  $\mathbf{c}$  axis. The magnetic moments are equal, within 4% relative error, at the three different Gd sites (one 4c and two 8d sites). The magnetic structure consists of ferromagnetic slabs (see Fig. 2.3) stacked antiferromagnetically along the  $\mathbf{b}$

direction.

A fully reversible spin-flop transition has been proposed based on magnetization measurements of  $\text{Gd}_5\text{Ge}_4$  [LGL<sup>+</sup>04]. In Fig. 5.1, we reproduce these measurements at 10 K for the sample used in the present experiments, with the field applied along the **c** axis. The temperature dependence of the critical field for the spin-flop transition,  $H_{\text{sf}}$ , was reported by Z. W. Ouyang et al [OPG<sup>+</sup>06] (see Fig. 5.2). No similar transition was found with the external field applied along either the **a** axis or **b** axis [LGL<sup>+</sup>04]. If the magnetic field  $H$  is increased further at this temperature to values above 18 kOe, a first order magneto-structural transition occurs from an antiferromagnet to a ferromagnet [OPG<sup>+</sup>06].

Details of the magnetic structure of  $\text{Gd}_5\text{Ge}_4$  in this spin-flop (SF) phase have not yet been determined since naturally occurring Gd has a large neutron absorption cross section. We have employed x-ray resonant magnetic scattering (XRMS) to study the magnetic structure of the SF phase. In addition to the advantages offered by XRMS for neutron absorbing samples, XRMS provides a means for measuring the magnetic moment direction through polarization analysis of the scattered beam. Further, the high angular resolution possible with synchrotron radiation provides a sensitive probe of magnetostriction effects.

Our results show that for all three Gd atomic sites, the moments flop from their zero-field alignment along the **c** axis, to the **a** axis, in fields larger than approximately 9 kOe applied along the **c** axis. No significant magnetoelastic distortion was observed across the transition within experimental error. We have compared these results, along with bulk magnetization measurements, to band-structure calculations of the magnetic anisotropy energy in  $\text{Gd}_5\text{Ge}_4$ , finding good agreement.

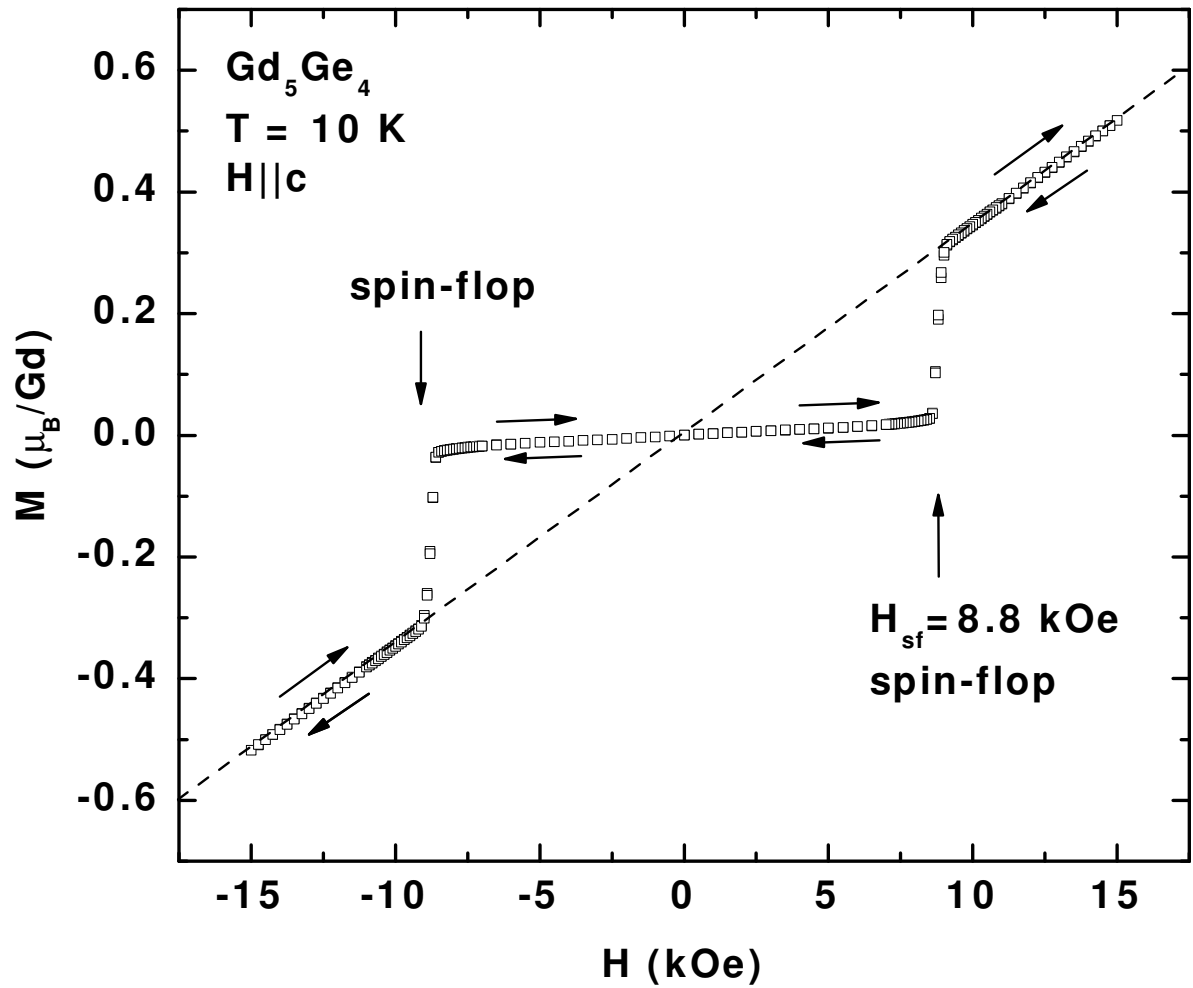


Figure 5.1 Field dependence of the magnetization of a zero-field cooled  $\text{Gd}_5\text{Ge}_4$  single crystal measured at  $T = 10\text{ K}$  with the magnetic field parallel to the  $c$  axis.

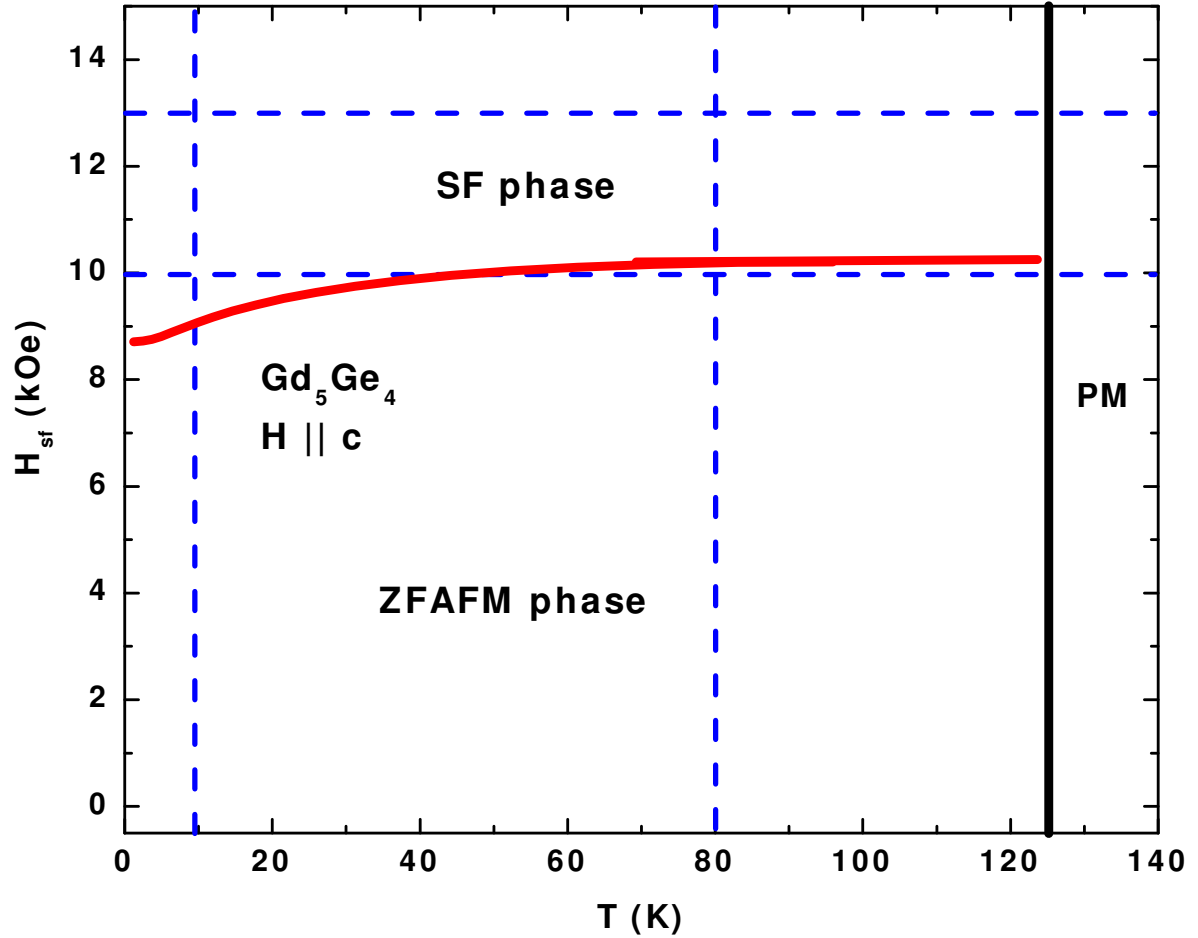


Figure 5.2 Temperature dependence of the spin-flop field,  $H_{\text{sf}}$ , derived from the field dependence of the magnetization measured at different temperatures. (From Ref. [OPG+06]) PM, SF, and ZFAFM represent the paramagnetic phase, the spin-flop phase, and the zero-field antiferromagnetic phase, respectively. The dashed lines represent the two field-dependence measurements and two temperature dependence measurements using XRMS in the present experiment.

## Experimental Details

Single crystals of  $\text{Gd}_5\text{Ge}_4$  for the magnetization and XRMS measurements were obtained from the Ames Laboratory Materials Preparation Center, which were grown using the Bridgman technique. Appropriate quantities of gadolinium (99.996% metals basis) and germanium (99.999%) were cleaned and arc melted several times under an argon atmosphere. The buttons were then re-melted to ensure compositional homogeneity throughout the ingot and the alloy drop cast into a copper mold. The as-cast ingot was electron beam welded in a tungsten Bridgman style crucible for crystal growth. The ingot was heated in a tungsten mesh resistance furnace under a pressure of  $8.8 \times 10^{-5}$  Pa up to  $1925^\circ\text{C}$  then withdrawn from the heat zone at a rate of 4 mm/hr. The as-grown crystal was oriented by back-reflection Laue and the crystallographic directions assigned using x-ray diffraction two theta scans of the single crystal. Samples were extracted from the ingot, and prepared with a polished surface perpendicular to the  $\mathbf{b}$  axis with a size of approximately  $2 \times 2 \times 3$  mm<sup>3</sup>. The magnetization was measured using a Quantum Design SQUID magnetometer.

The XRMS experiment was performed on the 4ID-D beamline at the Advanced Photon Source at an incident beam energy corresponding to the maximum in the resonant dipole scattering cross-section at the Gd  $L_2$  absorption edge [TKK<sup>+</sup>05]. The scattering geometry is shown in Fig. 5.3. A photon polarized perpendicular to the plane of scattering is said to exhibit  $\sigma$  polarization, while a photon polarized in the plane has  $\pi$  polarization. The incident beam was linearly polarized in the horizontal scattering plane ( $\pi$ -polarized) with a cross section of 0.22 mm (horizontal)  $\times$  0.1 mm (vertical). The sample was mounted on the cold finger of a Helium flow VTI (Variable Temperature Insert) with the  $\mathbf{b}$  axis parallel to the scattering vector  $\mathbf{Q}$ , and the  $\mathbf{c}$  axis perpendicular to the horizontal scattering plane. A vertical magnetic field was applied (perpendicular to the scattering plane) using a superconducting 4-Tesla split-coil magnet. Pyrolytic

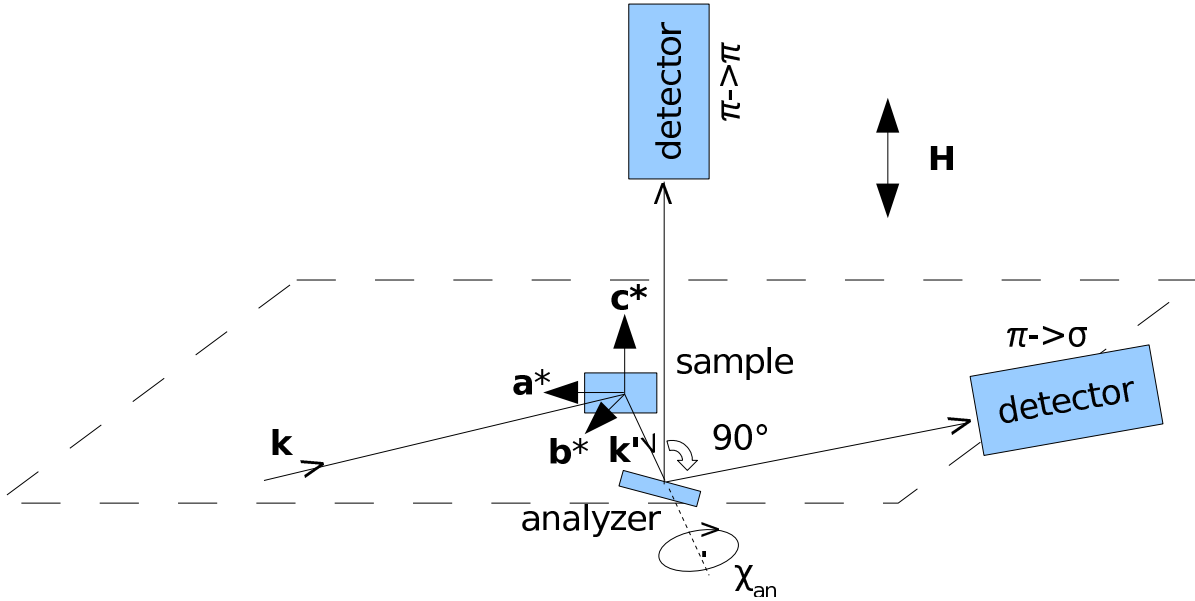


Figure 5.3 The experimental arrangement consisting of the sample, analyzer and detector.  $\mathbf{k}$  and  $\mathbf{k}'$  are the incident and scattered x-ray wave vectors respectively. The magnetic field  $\mathbf{H}$  was applied along the vertical direction. The switch between  $\pi-\sigma$  geometry (the detector arm in the horizontal plane) and  $\pi-\pi$  geometry (the detector arm along the vertical direction) was accomplished by a motor-driven analyzer angle,  $\chi_{an}$ .

graphite (0 0 6) functioned as both a polarization analyzer and to suppress the charge background in the measurement of the magnetic scattering signal.

The resonant scattering of interest, at the Gd  $L_2$  absorption edge, is due to electric dipole transitions between the core 2p states and the 5d conduction bands. The 5d bands are spin-polarized through the exchange interaction with the magnetic 4f electrons. The  $\pi-\pi$  scattering geometry is realized when the scattering plane for the sample is horizontal but that for the analyzer is vertical. In this geometry, the magnetic signal is sensitive to the component of the ordered magnetic moment out of the scattering plane, along the magnetic field direction ( $\mathbf{c}$  axis in this case). The scattering amplitude,  $f$ , is proportional to  $(\mathbf{k} \times \mathbf{k}') \cdot \boldsymbol{\mu}$  (i.e.  $\mu_c \sin 2\theta$ ) [HM96], where  $\mathbf{k}$ ,  $\mathbf{k}'$  and  $\boldsymbol{\mu}$  are the

wave vectors of the incident photons, scattered photons, and the magnetic moment, respectively. The  $\pi$ - $\sigma$  scattering geometry is realized when the scattering planes for both the sample and the analyzer are horizontal. In this geometry, the magnetic signal is sensitive to the components of the ordered magnetic moment within the **ab** scattering plane perpendicular to the magnetic field direction. The scattering amplitude,  $f$ , is proportional to  $\mathbf{k} \cdot \boldsymbol{\mu}$  (i.e.  $-\mu_a \cos \theta + \mu_b \sin \theta$ ) [HM96]. The motor-driven analyzer angle  $\chi_{\text{an}}$  which rotates about the scattered beam direction, provides the freedom to easily change between both scattering geometries (see Fig. 5.3). This allows all three Cartesian components of each moment to be probed without remounting the sample.

For  $\text{Gd}_5\text{Ge}_4$ , normal charge scattering is forbidden at the positions of the  $(0\ k\ 0)$  reflections where  $k$  is odd. Unfortunately, these positions can be strongly contaminated by multiple charge scattering. We can discriminate between the magnetic signal of interest and multiple scattering because the latter is highly sensitive to both the incident beam energy and the azimuth angle (see Fig. 3 in Ref. [TKK<sup>+</sup>05]). Hence, the multiple scattering contribution at the resonant energy can be minimized through a judicious choice of azimuth angle, where the resonant scattering is well separated from multiple scattering. In this particular experiment, all of the  $\mathbf{Q}$ -dependence measurements were performed using an azimuthal angle, the angle between the external field direction and **c** axis, of about  $\sim 7^\circ$ . This angle was chosen to minimize multiple scattering at reciprocal positions of different reflections. All other measurements were done with an azimuthal angle less than  $0.5^\circ$ .

## Results and Discussion

In this section, we describe magnetization measurements on the sample used for XRMS and confirm the magnetic structure of  $\text{Gd}_5\text{Ge}_4$  in zero field by XRMS. We then characterize the spin-flop transition in varying applied fields at selected temperatures.

We determined the magnetic structure of  $\text{Gd}_5\text{Ge}_4$  in the SF phase by measuring the  $(0\ k\ 0)$  magnetic Bragg reflections.

### Magnetization Measurements

The magnetization  $M$  of the zero-field cooled single crystal, measured at  $T = 10$  K, is shown in Fig. 5.1. The sample was cooled in zero field to 10 K. The external magnetic field was then applied along  $\mathbf{c}$  axis. The field was ramped up from 0 kOe to 15 kOe, and then back down to 0 kOe. Next, the sample was cycled through the opposite field direction. The  $M(H)$  curves coincide for increasing and decreasing magnetic field applied in  $\mathbf{c}$  direction, showing that the field-induced spin-flop transition is fully reversible and non-hysteretic. These data clearly show a jump at  $H_{\text{sf}} = 8.8$  kOe. The slope of the magnetization curve below the critical field is the susceptibility  $\chi_{\parallel}$  in the zero-field antiferromagnetic (ZFAFM) phase. The dashed line, which passes through the origin, represents the slope of the magnetization (i.e. the transverse susceptibility  $\chi_{\perp}$ ) in the SF phase. The transverse susceptibility is identical to measurements taken with the field along the  $\mathbf{a}$  and the  $\mathbf{b}$  axes. The projections of the moments along the  $\mathbf{c}$  axis in the SF phase are  $\sim 0.3\mu_{\text{B}}/\text{Gd}$  at  $H_{\text{sf}} = 8.8$  kOe. The magnetic anisotropy energy (MAE) related to antiferromagnetic order can be calculated from the magnetization measurement using  $E_{\text{ani}} = 1/2(\chi_{\perp} - \chi_{\parallel})H_{\text{sf}}^2$ . Here we consider  $\chi_{\parallel}$  and  $\chi_{\perp}$  as constants in both ZFAFM and SF phases as shown in Fig. 5.1 ( $\chi_{\parallel} = 0.0024\mu_{\text{B}}/\text{Gd}\cdot\text{kOe}^{-1}$  and  $\chi_{\perp} = 0.0345\mu_{\text{B}}/\text{Gd}\cdot\text{kOe}^{-1}$ ). The difference of energies between moments perpendicular to the  $\mathbf{c}$  axis and moments along the  $\mathbf{c}$  axis is about  $7\ \mu\text{eV}/\text{Gd}$ . These measurements are in close agreement with previous magnetization studies [LGL<sup>+</sup>04, OPG<sup>+</sup>06] that first suggested the existence of a spin-flop transition in this compound. While these measurements provided no direct information regarding the arrangement of Gd moments on the three inequivalent sites in the SF phase, it was speculated that all of the moments undergo a  $\sim 90^\circ$  rotation from the  $\mathbf{c}$  direction to the direction primarily along  $\mathbf{a}$  axis

Table 5.1 The measured and calculated values of the integrated intensity of  $(0\ k\ 0)$  reflections in  $\pi$ - $\pi$  geometry at  $T = 9$  K in zero field. The calculated values are based upon the model presented in Ref. [TKK<sup>+</sup>05]

$k$	measured (arb. unit)	calculated (arb. unit)
3	3.7(1)	3.4
5	1(1)	0.05
7	22.6(3)	22.6
9	0.5(5)	0.3
11	8.8(2)	9

[LGL<sup>+</sup>04].

### Magnetic Structure in Zero Field

We first consider the XRMS measurements in the  $\pi$ - $\pi$  scattering configuration, in the absence of a magnetic field. As the sample was cooled below the Néel temperature,  $T_N = 125$  K, resonant magnetic reflections were found at the charge forbidden  $(0\ k\ 0)$  positions (with  $k$  odd). The absorption edge energy was determined from an energy scan through the  $(0\ 8\ 0)$  charge reflection as shown in Fig. 5.4 (a). In Fig. 5.4 (b), for example, we show the scattered intensity at the  $(0\ 7\ 0)$  peak position as the incident beam energy is tuned through the Gd  $L_2$  absorption edge both above and below the Néel temperature. At  $T = 140$  K, above the Néel temperature, only residual charge scattering was observed arising from tails of multiple scattering peaks. Below  $T_N = 125$  K, the peak found at  $E = 7.932$  keV, just above the Gd  $L_2$  absorption edge, is the dipole resonance. The peak found at  $E = 7.952$  keV is assigned to multiple charge scattering since its position and intensity is extremely sensitive to both the energy and azimuthal angle.

Selected  $(0\ k\ 0)$  reflections were measured in both the  $\pi$ - $\sigma$  and  $\pi$ - $\pi$  scattering geometries at  $T = 9$  K in zero applied field. A Lorentzian peak was used to obtain the

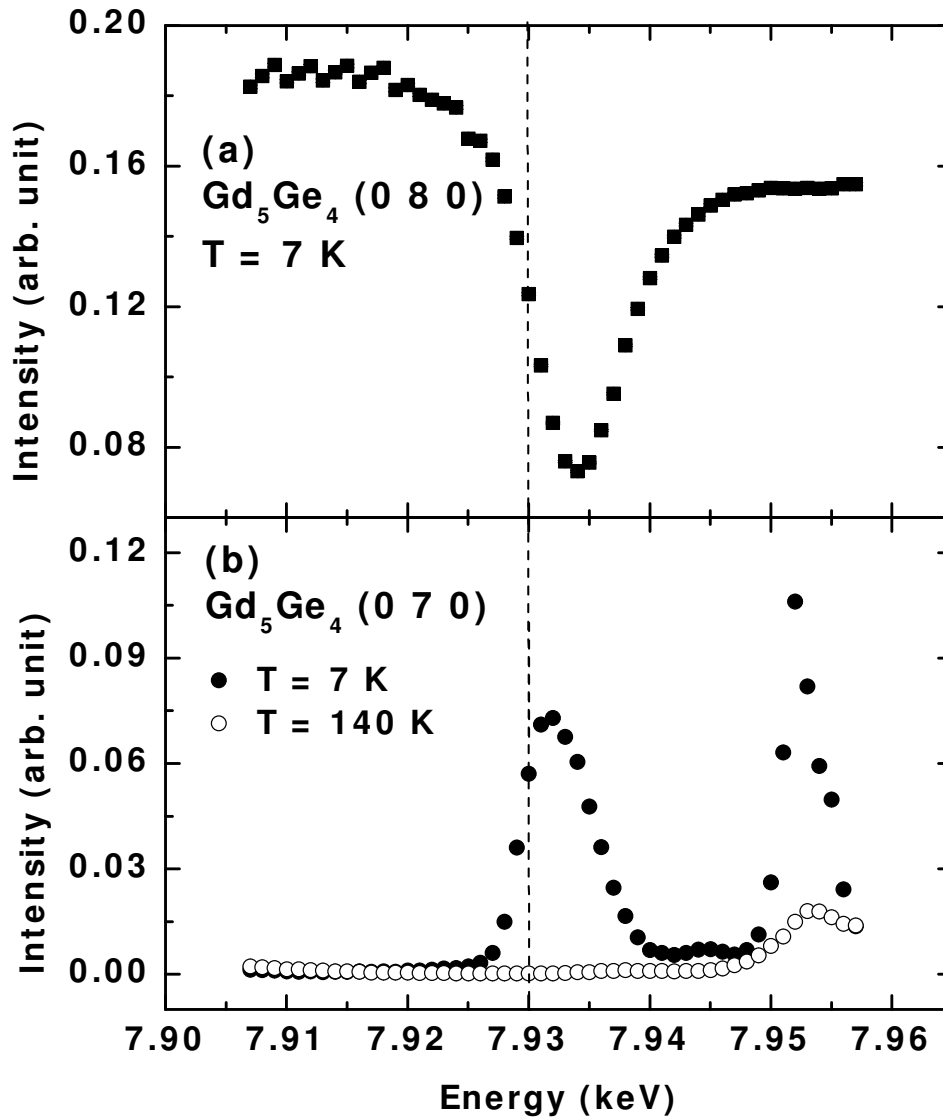


Figure 5.4 (a) Energy scan of the charge Bragg reflection,  $(0\ 8\ 0)$ , across the Gd  $L_2$  absorption edge. The dashed line indicates the inflection point and is taken to be the absorption edge energy. (b) Energy scans at the nominally charge forbidden  $(0\ 7\ 0)$  reflection across the Gd  $L_2$  absorption edge in  $\pi$ - $\pi$  geometry at  $T = 7\text{ K}$  (filled circles) and  $T = 140\text{ K}$  (open circles). The peak approximately 0.002 keV above the absorption edge is the dipole resonance while the sharp peak approximately 0.02 keV higher arises from multiple charge scattering.

integrated intensities of the rocking scans through the reciprocal lattice points. The results are shown in Table 5.1. The large errors for the (0 5 0) and (0 9 0) reflections arise from contamination from the tails of multiple scattering. As described in the previous section, magnetic reflections measured in the  $\pi$ - $\pi$  scattering geometry, are sensitive to the component of the magnetic moment along the  $\mathbf{c}$  axis. The measured intensities are consistent with the results of our previous scattering study [TKK<sup>+</sup>05]. Specifically, in zero field, the magnetic space group is  $Pnm'a$  for all Gd atoms in  $Gd_5Ge_4$  with the magnetic moments directed along the  $\mathbf{c}$  axis. While theoretical calculations show that the Gd moment at the 4c site is  $\sim 0.1\mu_B$  larger than those at the two 8d sites [PPGH07], the accuracy of our results is not sufficient to confirm this small difference.<sup>1</sup> We also observed weak, but measurable magnetic reflections in the  $\pi$ - $\sigma$  scattering geometry. This arises from the small, but finite, projection of the magnetic moments into the scattering plane because the  $\mathbf{c}$  axis of the crystal was tilted  $7^\circ$  away from vertical direction in these measurements.

### Observation of the Spin-Flop Transition

Fig. 5.5 displays the magnetic field dependence of the integrated intensity of (0 7 0) at  $T = 9$  K, normalized to the (0 8 0) charge reflection. The sample was first cooled in zero-field. The vertical magnetic field (along the  $\mathbf{c}$  direction) was then ramped up from 0 to 13 kOe. The spin-flop transition is evident in both scattering channels ( $\pi$ - $\pi$  and  $\pi$ - $\sigma$ ) at  $H_{sf} \sim 9$  kOe. This value for  $H_{sf}$  is consistent with the bulk magnetization measurement on this sample (see Fig. 5.1). The ratio between the maximum integrated intensities observed from  $\pi$ - $\pi$  scattering geometry below the spin-flop transition and the  $\pi$ - $\sigma$  scattering geometry above the spin-flop transition is not equal to one but the

---

<sup>1</sup>The errors of fitting parameter from the integrated intensities listed in Table 5.1 are larger than that from Table II in Ref. [TKK<sup>+</sup>05] because of the following two reasons: The (0 13 0) reflection is not achievable due to the geometric limit from the magnet in this present study. Low- $\mathbf{Q}$  reflections are much weaker in  $\pi$ - $\pi$  scattering geometry than that in the  $\sigma$ - $\pi$  scattering geometry.

geometric factor,  $(\sin 2\theta / \cos \theta)^2$  from the cross section for resonant magnetic scattering. (see Table 3.1)

Fig. 5.6 displays the magnetic field dependence for the charge-normalized integrated intensity of the (0 7 0) magnetic reflection at  $T = 80$  K. The spin-flop field,  $H_{\text{sf}} \sim 10.4$  kOe, increases only slightly with temperature, again consistent with the bulk magnetization measurements on a  $\text{Gd}_5\text{Ge}_4$  single crystal (see Fig. 5.2). At both temperatures, the full width half maximum (FWHM) of the (0 7 0) magnetic Bragg reflection, measured in both scattering geometries, increases as the integrated intensity decreases in the SF transition process. In contrast, the FWHM of the (0 8 0) charge Bragg reflection remains constant ( $0.05^\circ$ ) in both phases. The broader FWHM found in both transverse and longitudinal scans of magnetic reflections indicates a reduced correlation length and a decreased size of the magnetic domains.

Both above and below the spin-flop transition, scans along (0  $k$  0) were done to search for any additional satellite reflection signaling a change in the magnetic structure. Magnetic reflections were found only at reciprocal lattice points (0  $k$  0), where  $k$  is odd. No additional magnetic modulation vector develops in the transition, which indicates that the magnetic unit cell remains the same as in the ZFAFM phase. The magnetic (0 7 0) Bragg reflection changes from one polarization channel to the other in the transition but keeps the magnetic structure factor same for both phases, which is concluded from the intensity ratio from the two polarization channels. This indicates that the magnetic moments only change direction, but not the magnitude.

The field dependence of longitudinal scans of the (0 8 0) charge reflections were measured in reciprocal space at  $T = 9$  K as shown in Fig. 5.7. Within experimental error ( $\Delta k/k < 0.001$ , where  $k$  is the value of the scattering vector along  $\mathbf{b}$  axis.), there is no discontinuous change in the lattice parameter (peak position) at the SF transition. Therefore, the SF transition is not a magneto-structural transition.

The Full Width Half Maximum (FWHM) of the (0 7 0) magnetic Bragg reflection,

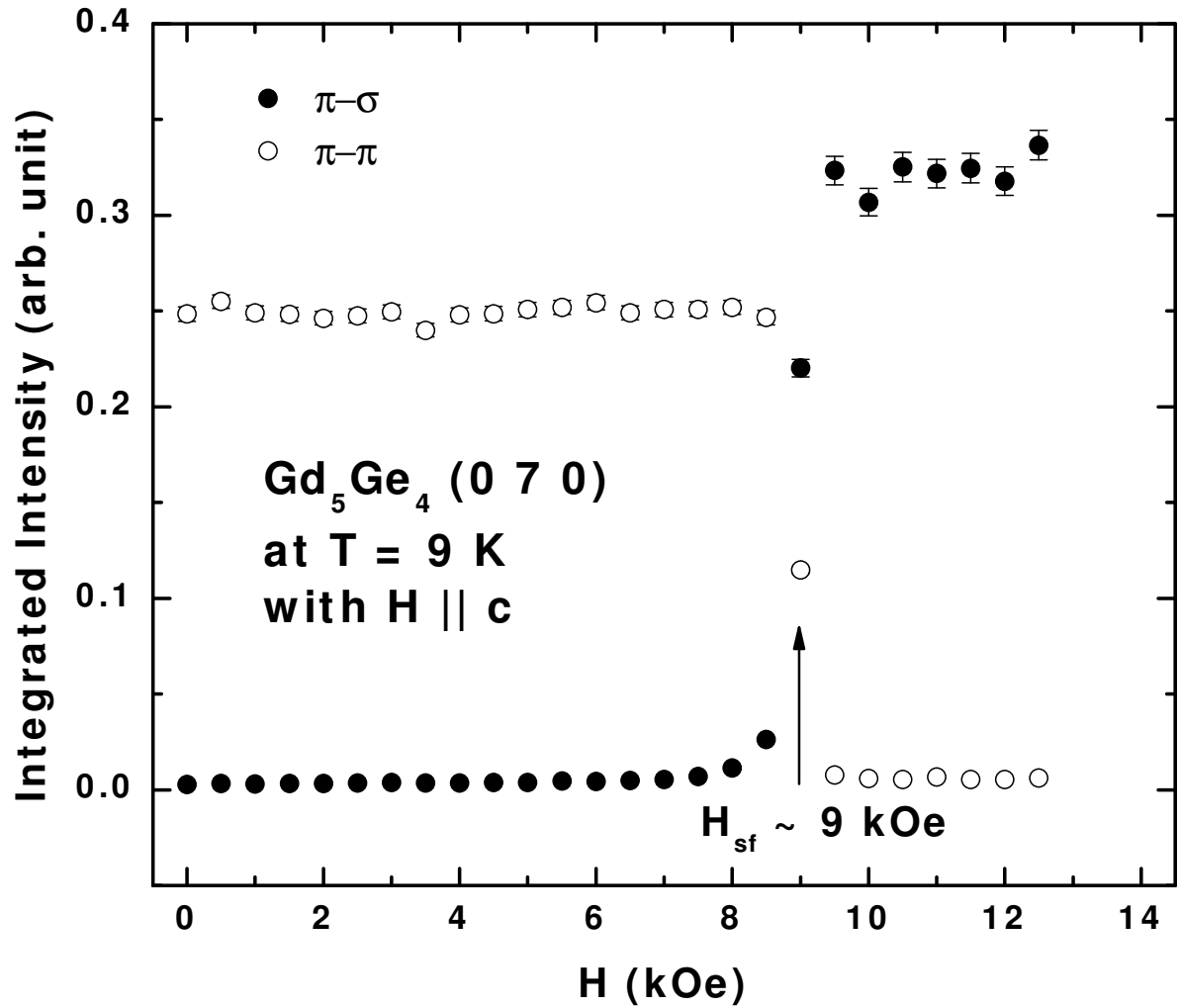


Figure 5.5 The (0 7 0) magnetic reflection measured with increasing magnetic field (along the **c** direction) in both  $\pi$ - $\pi$  and  $\pi$ - $\sigma$  geometries at  $T = 9$  K. Integrated intensity normalized by the (0 8 0) charge reflection.

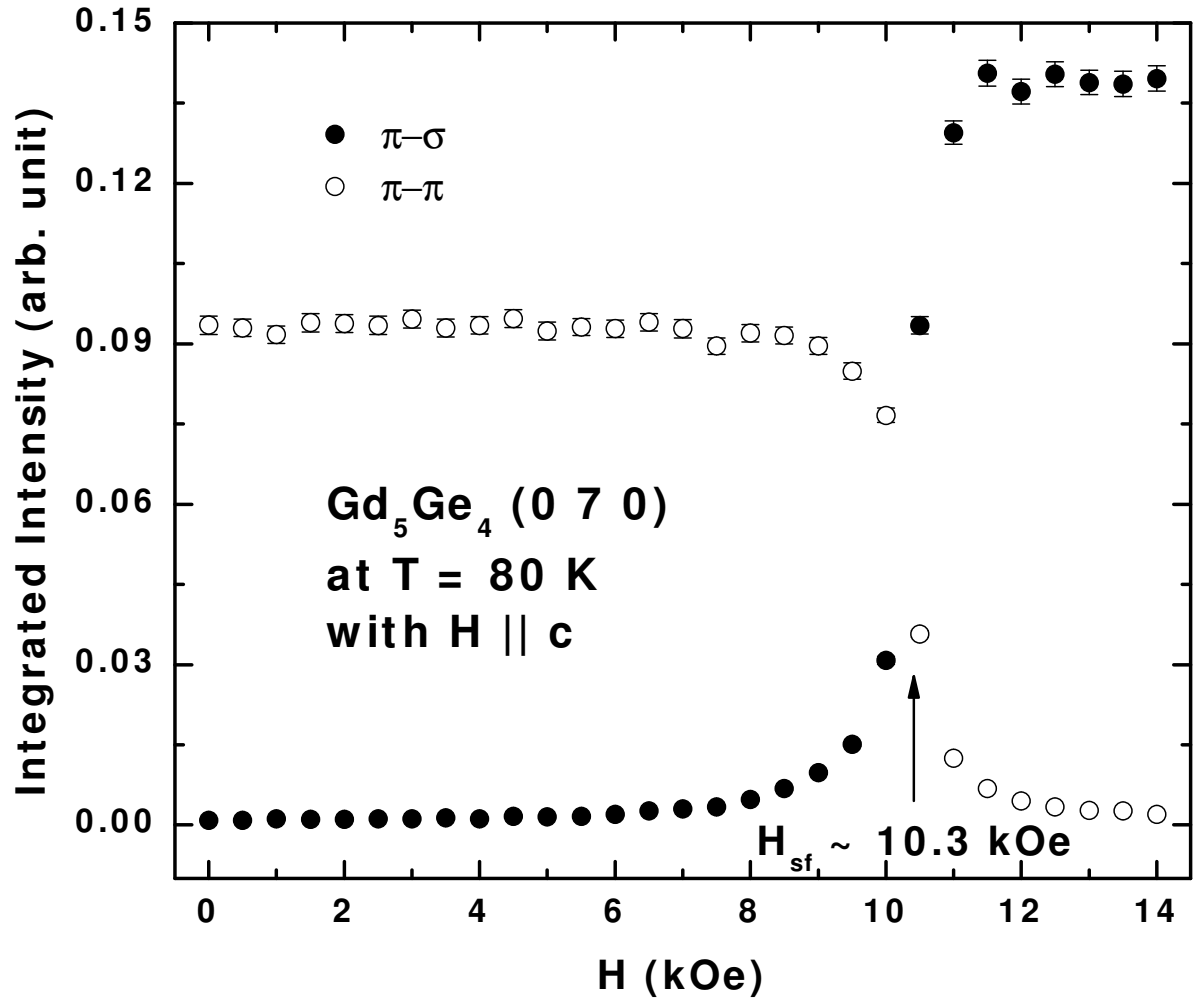


Figure 5.6 The (0 7 0) magnetic reflection measured with increasing magnetic field (perpendicular to the scattering plane) in both  $\pi$ - $\pi$  and  $\pi$ - $\sigma$  geometries at  $T = 80$  K. Integrated intensity normalized by the (0 8 0) charge reflection.

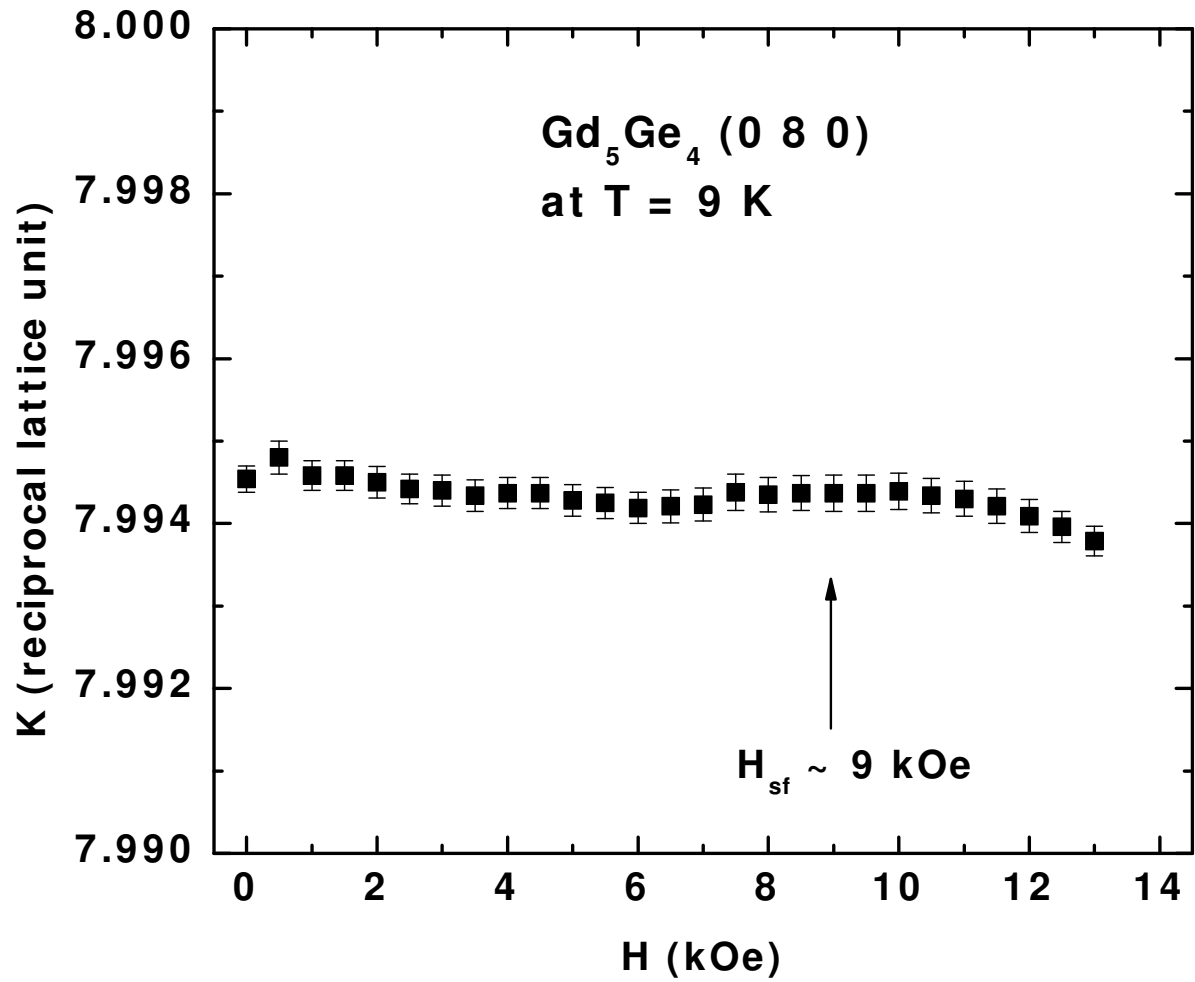


Figure 5.7 The longitudinal scans of the (0 8 0) charge reflections measured in the reciprocal space with increasing field at  $T = 9$  K.

measured in the both scattering geometries, increases as the integrated intensity decreases through the transition. In contrast, the FWHM of the (0 8 0) charge Bragg reflection remains constant ( $0.05^\circ$ ) in the both phases. When the external field along  $\mathbf{c}$  axis is ramped up at a fixed temperature to cross the phase boundary, the increasing of FWHM of the magnetic reflections in the AFM phase represent the decreasing of the size of the AFM domains. Similarly, the decreasing of FWHM of magnetic reflection in the spin-flopped phase represents the increasing of AFM domains size as shown in  $\pi - \pi$  geometry. A similar nucleation phenomena was found in the phase transition driven by temperature with constant external field. Generally, a first-order transition from one phase to another is characterized by a discontinuous jump in the order parameter, and by an energy barrier between the two phases. Because of the barrier, there is a surface tension associated with an interface between the two phases. A nucleus of the new equilibrium phase gains bulk free energy but costs surface energy. For the nucleus to grow, its radius must exceed a critical radius,  $R_c = 2\sigma/\delta f$ , where  $\sigma$  is the surface tension and  $\delta f$  is the gain in bulk free energy density. The critical nucleus may form from thermodynamic fluctuations (homogeneous nucleation) or heterogeneous nucleation [CL00]. The non-hysteretic property of the spin-flop transition as shown in Fig. 5.1 indicates the heterogeneous nucleation.

### Magnetic Structure in the Spin-Flop Phase

In the SF phase, strong magnetic reflections appear in  $\pi$ - $\sigma$  scattering geometry and they disappear in  $\pi$ - $\pi$  scattering geometry. Since the scattering amplitude,  $f \propto -\mu_a \cos \theta + \mu_b \sin \theta$ , in  $\pi$ - $\sigma$  geometry, the magnetic moments in the SF phase must be within the  $\mathbf{ab}$  scattering plane. There are eight possible magnetic space groups for  $\text{Gd}_5\text{Ge}_4$  (see Table I in Ref. [TKK<sup>+</sup>05]). From Table II in Ref. [TKK<sup>+</sup>05], it is easy to see that only one basis vector,  $A$ , for the  $4c$  site and two basis vectors,  $R$  and  $A_B$ , for the  $8d$  sites can contribute to the magnetic intensity of (0  $k$  0) reflections. We also note

Table 5.2 The measured and calculated values of the integrated intensity of  $(0\ k\ 0)$  reflections in  $\pi$ - $\sigma$  geometry at  $T = 9$  K with  $H = 10$  kOe. The calculated values are based on the magnetic space group  $Pn'm'a'$ .

$k$	measured (arb. unit)	calculated (arb. unit)
3	31.2(5)	31.3
5	1(1)	0.4
7	44.2(7)	44.1
9	0.6(6)	1.1
11	7.1(2)	7.1

that, in the most general case, all three Gd sites need not have the symmetry required by the same magnetic space group with corresponding basis vectors [Ber68]. The scattering structure factor can be calculated for each possible representation (combination of basis vectors) at the three sites. Therefore, the magnetic structure can be analyzed by a  $\mathbf{Q}$ -dependent measurement.

In order to determine the magnetic structure in the SF phase, the integrated intensities of a series of  $(0\ k\ 0)$  reflections were measured, in both  $\pi$ - $\sigma$  and  $\pi$ - $\pi$  scattering geometries at  $T = 9$  K with  $H = 10$  kOe. The integrated intensities measured in  $\pi$ - $\sigma$  geometry are listed in Table 5.2. The large errors for the  $(0\ 5\ 0)$  and  $(0\ 9\ 0)$  reflections again arise from contamination by multiple charge scattering. As was true for the zero-field data presented above, weak reflections were found in  $\pi$ - $\pi$  geometry due to a small but finite projection of the magnetic moments out of the scattering plane because of the finite azimuth angle. Considering all possible combinations of basis vectors at the three sites, the best fit to the data, as shown in Table 5.2, corresponds to all three magnetic Gd sites described by the same magnetic space group,  $Pn'm'a'$ , with moments aligned primarily along the  $\mathbf{a}$  axis. The Gd moments have intraslab FM correlation and interslab AFM correlation. The fitting yields the ratios  $\mu_a^{8d_1}/\mu_a^{4c} = 0.95 \pm 0.15$  and  $\mu_a^{8d_2}/\mu_a^{4c} = 1.17 \pm 0.18$ , where  $\mu_a^{4c}$ ,  $\mu_a^{8d_1}$ , and  $\mu_a^{8d_2}$  are the magnetic moment components

along  $\mathbf{a}$  axis at the three sites, respectively. We conclude that, within the error limits, the magnetic moments along  $\mathbf{a}$  axis are equal at the three Gd sites. Recalling that the magnetic moments along  $\mathbf{c}$  axis are same size at the three Gd sites in the ZFAFM phase [TKK<sup>+</sup>05], the spin-flop transition then corresponds to a simple  $\sim 90^\circ$  rotation of the antiferromagnetically aligned moments at all three Gd sites from the  $\mathbf{c}$  direction to the direction primarily along  $\mathbf{a}$  axis above  $H_{\text{sf}}$  as postulated by E. M. Levin et al [LGL<sup>+</sup>04].

In addition to the antiferromagnetic component, the system also has a ferromagnetic component induced by the external field along  $\mathbf{c}$  axis as shown in Fig. 5.1, which is not measurable directly by XRMS. The spin-flop transition in  $\text{Gd}_5\text{Ge}_4$  can be described by the picture proposed by L. Néel seven decades ago [N36]. A magnetic field along the easy axis can not change the magnetization of a local moment system unless it flops the moments. However, if the moments flop to a configuration perpendicular to the applied field, they can tilt along the magnetic field. In this way, the system gains Zeeman energy. When the net energy gained is greater than the anisotropy energy, the spin-flop transition occurs.

The temperature dependence of the integrated intensity of the (0 7 0) magnetic reflection in the ZFAFM phase and the SF phase is shown in Fig. 5.8. The intensity always decreases to zero as the temperature increases to  $T_N = 125$  K. When one curve is scaled by the geometric factor from scattering cross sections, the two are identical. This indicates that both phases have the same size of the magnetic moments, but are different in the moment direction at each temperature. Similar behavior of the integrated intensity in both phases also facilitates separation of the behavior when crossing the phase boundary by analyzing the temperature dependence of the integrated intensity as shown in Fig. 5.9. The transition temperature  $T_{\text{sf}} \sim 42$  K is the inflection point of the curve. The width for the SF transition is  $\sim 20$  K and is consistent with Ref. [OPG<sup>+</sup>06]. The non-vanishing resonant signal in the ZFAFM phase, which was measured in  $\pi$ - $\sigma$  channel after the transition is complete, represents minor spin-flop domains coexisting

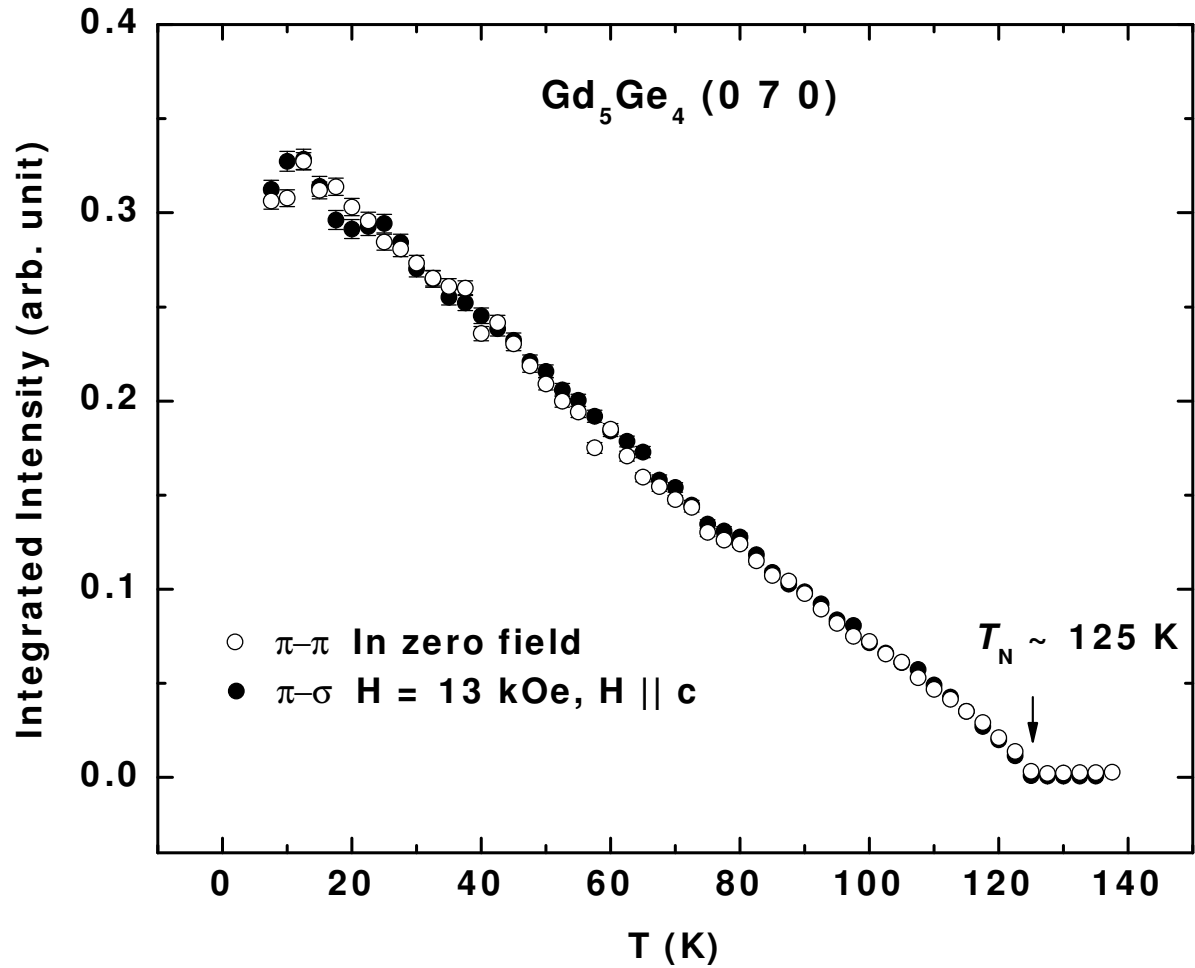


Figure 5.8 Integrated intensity of the (0 7 0) magnetic reflection measured when the sample was warmed up. The open circles represent the measurement in the  $\pi$ - $\pi$  scattering geometry in zero field. The closed circles represent the measurement in the  $\pi$ - $\sigma$  geometry in a vertical magnetic field,  $H = 13$  kOe (the spin-flop phase). Both are normalized by the integrated intensity of the (0 8 0) reflection measured in  $\pi$ - $\sigma$ . For comparison, the data in  $\pi$ - $\pi$  are divided by the geometric factor,  $(\sin 2\theta / \cos \theta)^2$ .

with the major ZFAFM phase. In this minor phase, a smaller SF domain size is estimated from the larger FWHMs of rocking scans and the longitudinal scans than those in the ZFAFM phase. From Fig. 5.2, the measurement of temperature dependence with  $H = 10$  kOe is close to the line representing the spin-flop transition in the high temperature region in the phase diagram. Thermodynamically stable multidomain states exist in the spin-flop region, owing to the phase coexistence at this first-order transition [BZR07].

## Discussion

### Magnetic Anisotropy Related to Antiferromagnetic Order

We know now that this field-induced phase transition is a pure SF transition at all three Gd sites. In general, the weak uniaxial magnetic anisotropy is essential for the SF transition. In rare earth compounds, potential sources of magnetic anisotropy include contributions from single ion, dipolar, and exchange interactions. For most of the rare-earth elements with finite orbital moments, the single-ion anisotropy due to crystalline electric field (CEF) effects dominates the anisotropy of the magnetic ground state. However, in gadolinium compounds, CEF effects are negligible due to the half filled 4f-shells ( $L = 0$ ). This is an ideal situation for studying the anisotropy due solely to weak interactions. In Gd metal, both the dipolar interactions and the spin-orbit interactions of the conduction electrons determine the magnetic anisotropy [JM91, FDG87, GHFD89, KS00, CTSA<sup>+</sup>03, CTBE<sup>+</sup>05]. Investigations of the anisotropy of magnetic interactions in some Gd compounds have been reported [RLD<sup>+</sup>03, GKG<sup>+</sup>05]. Here, we estimate the magnitude of magnetic anisotropy in the intermetallic compound  $\text{Gd}_5\text{Ge}_4$  based on band structure and magnetic dipole-dipole interactions calculations. The results are compared with the magnetization measurements in light of the magnetic structure determined by XRMS.

As the MAE is only about  $10 \mu\text{eV}/\text{Gd}$ , we must consider both the dipolar interactions

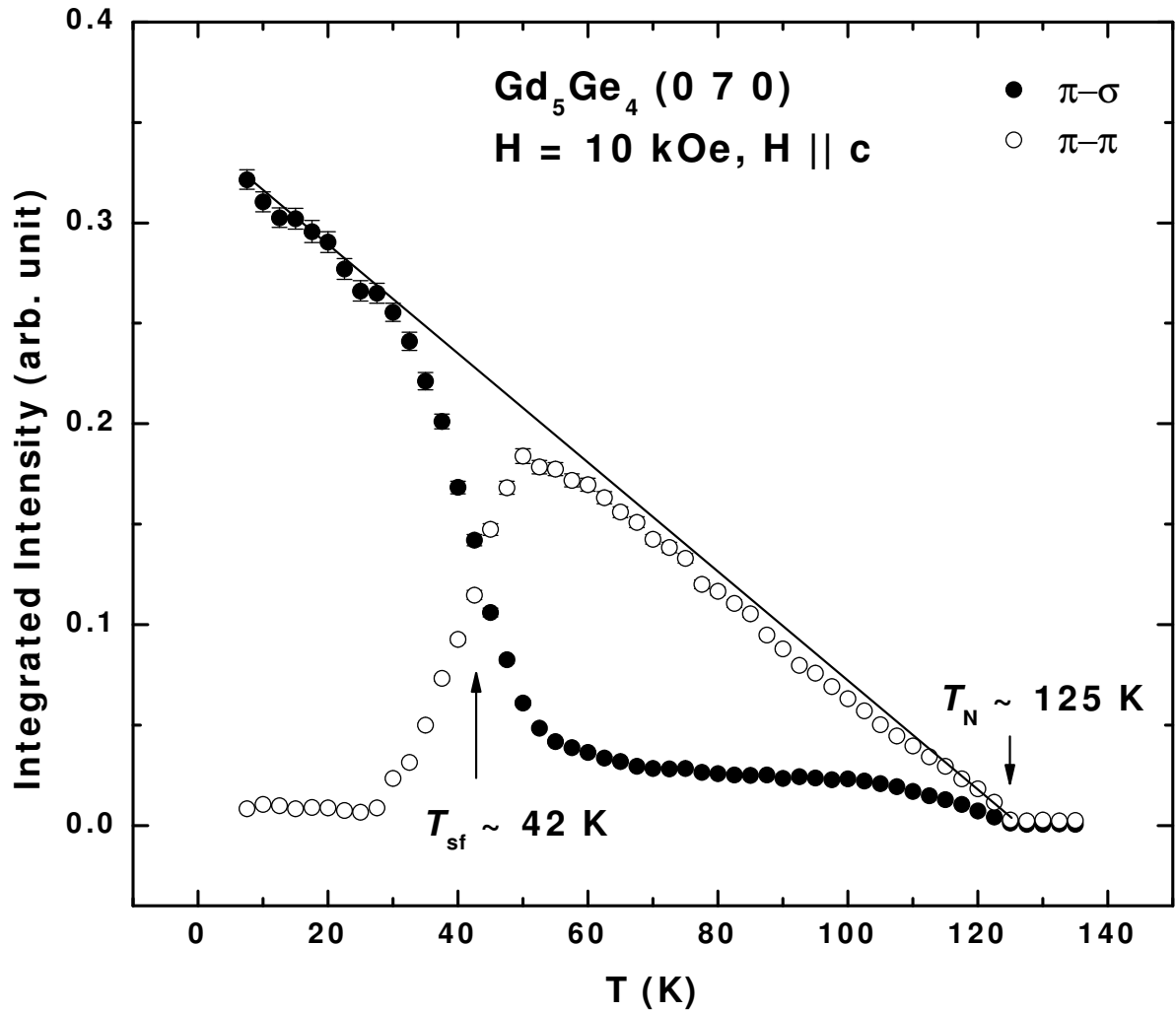


Figure 5.9 Integrated intensity of the (0 7 0) magnetic reflection measured when the sample was warmed up in a vertical magnetic field,  $H = 13$  kOe. The data in both scattering channels are normalized by the integrated intensity of the (0 8 0) reflection measured in  $\pi$ - $\sigma$ . For comparison, the data in  $\pi$ - $\pi$  are divided by the geometric factor,  $(\sin 2\theta / \cos \theta)^2$ . The straight line is drawn to guide the eyes.

Table 5.3 The magnetic anisotropy energies for  $\text{Gd}_5\text{Ge}_4$  from two different interactions. The calculations were made for AFM components along three crystallographic axes. The moments along **a**, **b**, and **c** correspond to magnetic space groups  $Pn'm'a'$ ,  $Pnma'$ , and  $Pnm'a$ , respectively. The moment size is assumed as  $7\mu_B/\text{Gd}$ . SO represents the spin-orbit interaction. Y.B. Lee calculated the MAE from SO in 5d bands.

The direction of AFM components	<b>a</b>	<b>b</b>	<b>c</b>
MAE from dipolar interactions ( $\mu\text{eV}/\text{Gd}$ )	-222	438	-217
MAE from SO in 5d bands ( $\mu\text{eV}/\text{Gd}$ )	10	-10	0
Total ( $\mu\text{eV}/\text{Gd}$ )	-212	428	-217

and the spin-orbit interactions of conduction electrons. The MAE associated with the dipole-dipole interaction in  $\text{Gd}_5\text{Ge}_4$  was numerically calculated with the assumption that the local moment is  $7\mu_B/\text{Gd}$  and that the moments are aligned along the three crystallographic directions and antiferromagnetically coupled between neighbored slabs for each of the three cases. According to this simple model, the dipolar energies are  $-222\mu\text{eV}/\text{Gd}$ ,  $438\mu\text{eV}/\text{Gd}$ , and  $-217\mu\text{eV}/\text{Gd}$  for moments along **a** axis, **b** axis, and **c** axis, respectively, as shown in Table 5.3. The dipolar interaction clearly yields the **b** axis to be the hard axis. The difference of MAEs between moments along **a** and **c** axes is quite small.

We now turn to the magnetic anisotropy due to the spin-orbit coupling in the conduction band. The 4f moments polarize the conduction electrons via the exchange interactions, which in turn transfer the magnetic anisotropy of the 5d conduction electrons to the Gd 4f magnetic moments through the 4f-5d exchange interaction. The MAE was calculated from first principles using the scalar relativistic [KH77], full potential linear augmented plane wave (FP-LAPW) method [BSM<sup>+</sup>01] with the LDA+ $U$  [PW92]. The  $U$  potential that was applied to properly treat the localized Gd 4f states was 6.7 eV [SLP99]. The spin-orbit (SO) interaction was added in each self-consistent iteration by

the second variation method. To obtain the self-consistent potential and the charge density distribution, we used 35  $\mathbf{k}$ -points in an irreducible Brillouin zone (IBZ), 3.2 and 2.2 atomic units for the Gd and Ge muffin-tin radius ( $R_{\text{MT}}$ ), respectively, and about 4000 basis functions. ( $R_{\text{MT}} \times K_{\text{max}} = 7.0$ ;  $K_{\text{max}}$  is the maximum value of the wave vector in the wave functions.) The magnetic anisotropy is the total energy difference between the magnetic moment configurations which have different SO strength. We employed 729  $\mathbf{k}$ -points in the IBZ to obtain an accurate total energy. The energy calculated with moments along the  $\mathbf{c}$  axis is 10  $\mu\text{eV}/\text{Gd}$  higher than that along the  $\mathbf{b}$  axis, and 10  $\mu\text{eV}/\text{Gd}$  lower than that along the  $\mathbf{a}$  axis as shown in Table 5.3. The SO coupling of the conduction electrons yields a weak orthorhombic anisotropy.

If both the dipolar calculation and SO calculation are combined, the energy calculated with moments along the  $\mathbf{c}$  axis is 5  $\mu\text{eV}/\text{Gd}$  lower than that along the  $\mathbf{a}$  axis and 645  $\mu\text{eV}/\text{Gd}$  lower than that along the  $\mathbf{b}$  axis. The  $\mathbf{a}$  and  $\mathbf{c}$  axes define the “easy plane”. The easy axis is the  $\mathbf{c}$  axis for the antiferromagnetic ground state in zero field according to this calculation. The moments in the SF phase prefer to align along the  $\mathbf{a}$  axis. The 5  $\mu\text{eV}/\text{Gd}$  difference in MAEs between the ZFAFM phase and the SF phase agree in magnitude with the experimental result, 7  $\mu\text{eV}/\text{Gd}$ .

## Conclusions

The XRMS experiments on  $\text{Gd}_5\text{Ge}_4$  have shown that the antiferromagnetically aligned moments at the three Gd sites flop from the  $\mathbf{c}$  axis to  $\mathbf{a}$  axis at  $T = 10$  K with a critical field,  $H_{\text{sf}} = 9$  kOe. The magnetic space group changes from  $Pnm'a$  to  $Pn'm'a'$  at all three sublattices. Both phases have intraslab FM correlations and interslab AFM correlations. The magnetic correlation is unchanged in both phases below  $T_N = 125$  K. We conclude that this field induced transition is a pure spin-flop transition, since the antiferromagnetically ordered moments at the three Gd sites flop from the  $\mathbf{c}$  direction to

the **a** direction. A small ferromagnetic component along **c** axis is induced by the applied field at the transition. Though  $\text{Gd}^{3+}$  ions have negligible single ion anisotropy, the easy plane anisotropy of the ordered state in  $\text{Gd}_5\text{Ge}_4$  originates from the dipolar interactions, with the SO coupling of the conduction electrons providing a weak orthorhombic anisotropy.

## CHAPTER 6. Short-Range Order in $\text{Gd}_5\text{Ge}_4$

Studies of the magnetization, heat capacity, and neutron scattering of  $\text{R}_5(\text{Si,Ge})_4$  indicate that magnetic short-range order (SRO) is retained above the Néel temperature. These results have recently been interpreted as evidence of a Griffiths phase based on Small-Angle Neutron Scattering (SANS) measurements of polycrystalline  $\text{Tb}_5\text{Si}_2\text{Ge}_2$  [MAM<sup>+</sup>06]. A Griffiths phase is a nanoscale magnetic clustering phenomenon that is driven by randomness in magnetic interactions that can be induced by chemical disorder or competing magnetic interactions. Interestingly, a ferromagnetic (FM) Griffiths-like phase has also been proposed to exist above the Néel transition in antiferromagnetic (AFM)  $\text{Gd}_5\text{Ge}_4$  based on the magnetization studies [OPKAG<sup>+</sup>06]. The nature of the AFM ordering in  $\text{Gd}_5\text{Ge}_4$ , which consists of strongly FM coupling block layers that have a weak AFM inter-block coupling, may play an important role. Before our XRMS studies, diffraction studies of magnetic SRO in the proposed Griffiths phase in  $\text{Gd}_5\text{Ge}_4$  had not been performed on single-crystal specimens. The Griffiths phase was expected to be observed as diffuse magnetic peaks above the (FM or AFM) magnetic transition temperature.

### Magnetization Measurements

In Fig. 6.1, the magnetization curves were measured on a single crystal of  $\text{Gd}_5\text{Ge}_4$  by Ouyang et al [OPKAG<sup>+</sup>06]. The temperature dependence of the inverse susceptibility ( $H/M$ ) curve follows the Curie-Weiss behavior only above  $\sim 240$  K. A curved downturn feature is present below this temperature. The  $H/M$  temperature dependence starts

to deviate from linear behavior between  $T_N$  and 160 K, which indicates that magnetic short-range order may exist in this temperature range. The positive paramagnetic Curie temperature implies dominant ferromagnetic interaction between magnetic ions. The curve of inverse magnetic susceptibility along the **b**-axis exhibits the largest deviation from Curie-Weiss behavior below 240 K. The one along **c**-axis shows the smallest deviation. Therefore, the **b**-axis may play a major role in defining short range ferromagnetic (FM) correlations in this compound. Randomly occurring FM clustering formed by the ferromagnetically ordered slabs in the long range ordered O(II)-type AFM  $\text{Gd}_5\text{Ge}_4$  may exist [RCC<sup>+</sup>06]. Therefore, the formation of the Griffiths-like phase above the Néel temperature may result from the competition of the AFM and FM exchange interactions that are present in a distinctly layered crystal structure of  $\text{Gd}_5\text{Ge}_4$ . We note that the Curie temperature  $T_C$  of any O(I)- $\text{Gd}_5\text{Si}_x\text{Ge}_{4-x}$  compound is always higher than that of an interslab bond-deficient monoclinic [CPP<sup>+</sup>00, PG97c] or O(II) polymorphic modification with the same stoichiometry [PSA<sup>+</sup>03]. Hence, random FM interactions and clustering are likely to occur inside the magnetically disordered  $\text{Gd}_5\text{Ge}_4$  slabs at temperatures much higher than  $T_N$ .

### **The Estimation of Scattering Intensity from Possible Short-Range Order**

Above the magnetic critical temperature, magnetic long-range order is broken, which is indicated by the disappearance of the magnetic Bragg reflections from diffraction pattern with increasing temperature passing through the magnetic critical temperature. Microscopically the magnetic moments at two different lattice points with long distance become uncorrelated. The arrangement of moments becomes more or less random. If a perfect randomness is achieved, the magnetic state is a paramagnet. However in some cases, there is tendency for a local specific arrangement of magnetic moments due to exchange interaction. Such magnetic state is called a magnetic short-range order.

The short-range correlation can be specified by the scattering effects produced. (see

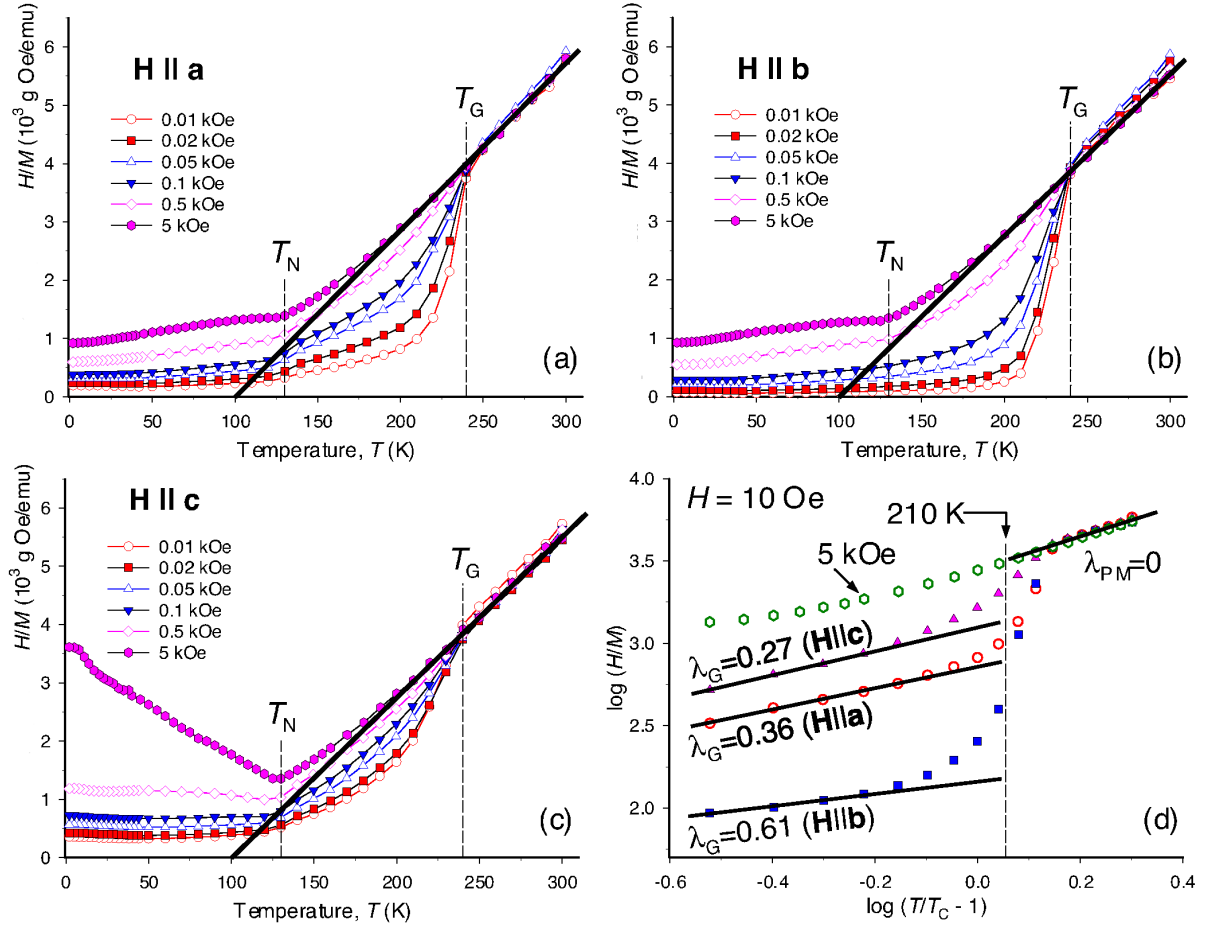


Figure 6.1 The field cooling inverse dc magnetic susceptibility of a single crystal  $Gd_5Ge_4$  measured along the **a** (a), **b** (b), and **c** axes (c) in magnetic fields ranging from 0.01 to 5 kOe. Panel (d) illustrates  $\log(H/M)$  vs  $\log(T/T_C - 1)$  for the three axes measured in a 10 Oe magnetic field and the same for the 5 kOe data along the **b** axis. ( $T_C$  is the critical temperature) Thick solid lines in (a)-(c) represent Curie-Weiss fits of the 5 kOe data. Solid lines in (d) are linear fits of  $\log(H/M)$  vs  $\log(T/T_C - 1)$  to establish  $\lambda$  in  $\chi(T) \propto (T - T_C)^{-(1-\lambda)}$ , with the dashed vertical line indicating the maximum slope of the curve for  $\mathbf{H} \parallel \mathbf{b}$ . Taken from Ref. [OPKAG<sup>+</sup>06]

Fig 6.3) If the magnetic moments arrangement is perfectly random, the scattered intensity decreases gradually the scattering vector increases from zero due to the polarization effect (The form factor is a constant). If short-range order exists, the curve of intensity vs scattering vector should exhibit low broad maxima. These maxima are usually located at the same positions in the reciprocal space as the sharp lines (Bragg reflections) from the superlattice formed by long-range ordering.

The  $\text{Gd}_5\text{Ge}_4$ -type crystal can be considered as being built up of a set of parallel layers. The forces acting within layers are greater than those acting between layers, which provides the features of rigidity within the layer and relative motion between layers. Such a picture is particularly useful since such layered crystals were often reported having incomplete order by X-ray investigations. The incomplete order may be due to the irregular sequence of layers, which result in changes of diffraction intensity and broadening of the interference spots in the x-ray diffraction investigation. Such an x-ray interference calculation was first investigated by Hendricks and Teller [HT42].

In our case, if the magnetic materials can be considered as being built up of a set of parallel or antiparallel spin layers, the magnetic layer irregularities may also be manifested by changes of intensities in the magnetic diffraction pattern by diffuse scattering. Below the Néel temperature,  $\text{Gd}_5\text{Ge}_4$  has a layer-ordered magnetic structure in which the ferromagnetic slabs are stacked antiferromagnetically along the  $\mathbf{b}$  direction with magnetic moments along the  $\mathbf{c}$  direction. The RKKY exchange interactions play a major role in correlation between magnetic ions in each slab. It is a good assumption that the intra-slab exchange interactions are larger than the inter-slab exchange interactions, since the RKKY indirect exchange interaction can not be easily transferred through broken Ge-Ge bonds [HLH<sup>+</sup>07].

Let us start the calculation based on the Hendricks-Teller model [HT42] for a partially magnetic ordered layered system as shown in Figure 6.2:

1. The magnetic moments in each slab are strongly coupled to each other and aligned

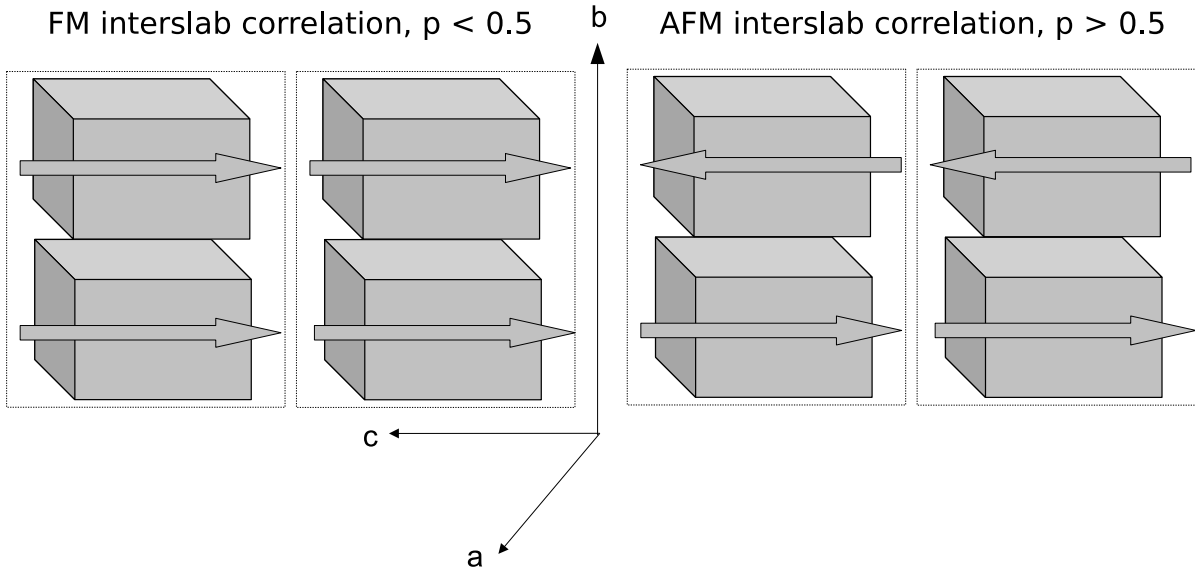


Figure 6.2 Ferromagnetic (left side, high probability when  $0 < p < 0.5$ ) and antiferromagnetic (right side, high probability when  $0.5 < p < 1$ ) correlations between neighboring slabs in the Hendricks-Teller partial order.

ferromagnetically along the  $\mathbf{c}$ -axis.

2. The total moment for each slab can take the value 1 or -1. (Ising-like)
3. The Griffiths phase-like AFM clustering is described by the probability, a variable  $p$  ( $0 < p < 1$ ), of the total moments of neighboring slabs aligning along the opposite direction. When  $p = 1$ , neighboring slabs must order antiferromagnetically along  $\mathbf{b}$ -axis i.e. the sample has an AFM long-range order along the defined direction. When  $p = 0$ , neighboring slabs must order ferromagnetically i.e. the sample has a FM long-range order along the defined direction. When  $p = 0.5$ , neighboring slabs have 50% possibility of aligning either ferromagnetically or antiferromagnetically.

For the purpose of calculations, layers will be treated as having form factors. The layer form factor is analogous to the atom form factor. The layer form factor has been

calculated by adding the scattering from the magnetic moments within the layers.

In  $\text{Gd}_5\text{Ge}_4$ , the magnetic structure factor from one slab is considered as the layer form factor. Each slab contains ten Gd atoms: two at the  $4c$  site, eight at two  $8d$  sites. All magnetic moments in the same slab point in the same direction. Let's say the magnetic moments in the first slab are along the positive direction of the  $\mathbf{c}$ -axis. Then a random number is generated to describe the magnetic coupling between the first and the second slabs. If  $p = 0.75$ , then this random number has 75% chance to be  $-1$  and 25% chance to be 1. If the random number is generated to be 1, then the magnetic moments in the first two neighboring slabs are parallelly aligned i.e. the magnetic moments in the second slab (neighboring to the first slab) are also aligned along the positive direction of  $\mathbf{c}$ -axis. If the random number is generated to be  $-1$ , the magnetic moments in neighboring slabs are antiparallel aligned. In the same way, we can generate the second random number for describing the magnetic coupling between the second and third slabs, the third random number for the third and fourth slabs, and so on. The  $p$  value is related to the correlation length of the magnetic short-range order. For example, if  $p = 0.5$  for the slabs stacking along  $\mathbf{b}$ -axis, the correlation length of the short-range order along  $\mathbf{b}$ -axis is about  $7 \text{ \AA}$ , i.e. the dimension for a slab.

In order to get a approximate comparison of the intensity between the magnetic short-range order and the magnetic Bragg diffraction, we start here with a preliminary estimation of the intensity based on the simple model described above. Since the full width at half maximum (FWHM) of charge Bragg reflections ( $0\ k\ 0$ ) is about 0.005 reciprocal lattice units, the dimension is about 200 unit cells i.e. 400 slabs. The probabilities  $p = 1, 0.95, 0.05, 0$  are used to generate about 400 random numbers of 1 and  $-1$  to represent the magnetic correlations between neighboring slabs in dynamic clusters. Then, the structure factor,  $f(q)$  for each  $p$  value is numerically calculated as the function of the scattering vector,  $q = (0k0)$ . The plot of the intensity,  $I = f(q)^2$  versus the scattering vector,  $q = (0k0)$ , is shown in Fig. 6.3. The data points  $(k, I)$  are generated with a step

size 0.2. ( $k = 1, 1.2, 1.4, \dots$ ) For  $p = 1$ , i.e. the long-range antiferromagnetic ordered system, the magnetic reflections appear at  $k = 1, 3, \dots$ , odd integer positions in the reciprocal space. The structure is same as the magnetic structure observed at  $T = 10$  K. For  $p = 0$ , i.e. the long-range ferromagnetic order system, the magnetic reflections appear at  $k = 2, 4, \dots$ , even integer positions in the reciprocal space. For  $p = 0.95$ , i.e. the short-range antiferromagnetic order system with a 0.95 probability of the antiparallel neighbor-slab spins, the broad magnetic features appear near  $k = 1, 3, \dots$ , odd integers positions in the reciprocal space. For  $p = 0.05$ , i.e. the short-range ferromagnetic order system with the 0.05 probability of the antiparallel neighbor-slab spins, the broad magnetic features appear near  $k = 2, 4, \dots$ , even integers positions in the reciprocal space.

The amplitudes of intensities of both the strongest magnetic Bragg reflection and the short-range order, which is based on this simple model, are compared from the calculation of structure factors. The ratio of both,  $I_{p=0.5}^{\text{Max}}(\text{SRO})/I_{p=1}^{\text{Max}}(0\ 7\ 0)$  is about  $10^{-3}$ , where  $I_{p=0.5}^{\text{Max}}(\text{SRO})$  is the maximal intensity of magnetic diffuse scattering when  $k > 2$  from the experimental limitation, and  $I_{p=1}^{\text{Max}}(0\ 7\ 0)$  is the amplitude of the magnetic reflection (0 7 0).

In order to estimate the intensity from measurements, we have to consider the FWHMs of the rocking scans on analyzers, since the analyzers with FWHMs from different rocking scans have different acceptance of scattered signals from the sample. The diffuse signal from the sample is more divergent than Bragg diffractions. In the other word, the FWHM of the rocking scans from the diffuse scattering is generally much bigger than that of the Bragg diffractions from either the sample or the analyzer. We note here that the FWHM of the rocking scans of (0 7 0),  $0.05^\circ$ , is much smaller than that of the pyrolytic graphite analyzer,  $0.5^\circ$ . Therefore, the measured intensity of the (0 7 0) reflection at Bragg condition is not influenced by the FWHM of the graphite analyzer, while the measured diffuse intensity is strongly determined by the FWHM of the graphite analyzer. The former intensity is the integrated intensity from the charac-

Table 6.1 Estimated intensity for magnetic short-range order using a pyrolytic graphite analyzer. We take  $p = 0.5$ .  $I_1^{\text{Max}}$  is the magnetic diffuse scattering intensity from the model with magnetic long-range order along two dimensions and short-range order along the other dimension.  $I_2^{\text{Max}}$  is the intensity from the model with magnetic long-range order along one dimension and short-range order along the other two dimensions.  $I_3^{\text{Max}}$  is the intensity from the model with short-range order along all three dimensions.

	$I_1^{\text{Max}}$	$I_2^{\text{Max}}$	$I_3^{\text{Max}}$
Estimated intensity (counts/s)	1000	1	$10^{-3}$

teristic of the sample while the latter is the integrated intensity from the characteristic of the graphite analyzer. Hence, the ratio of both measured intensities would be:

$$I_{p=0.5}^{\text{measure}}(\text{SRO})/I_{p=1}^{\text{measure}}(0\ 7\ 0) = \frac{I_{p=0.5}^{\text{Max}}(\text{SRO}) \times FWHM_{\text{analyzer}}}{I_{p=1}^{\text{Max}}(0\ 7\ 0) \times FWHM_{\text{sample}}} = 10^{-2}$$

We recall that the intensity of (0 7 0) magnetic reflection is experimentally about  $10^5$  counts/s as described in Chapter 4. Therefore, the count rate should be about 1000 counts/s from the simple model, in which the magnetic long-range order is along **a** and **c** axes directions and magnetic short-range order is along **b**-axis.

The ratio,  $I_{p=0.5}^{\text{Max}}(\text{SRO})/I_{p=1}^{\text{Max}}(0\ 7\ 0)$  yields very important information. If the magnetic structure changes from the low symmetry (magnetic long-range order along all three dimensions) to the high symmetry (magnetic long-range order along two dimensions and short-range order along the other dimension), the scattering intensity decreases by a factor of  $10^{-3}$ . If the magnetic SRO has to be described by short-range order along two crystallographic directions (only one dimension is long-range ordered, the other two dimensions are short-range ordered), the scattering intensity would decrease by factor of  $10^{-3}$  again.<sup>1</sup> The count rate is estimated as 1 counts/s. Similarly, if the magnetic short-range order is three dimensional in the system, the count rate is estimated as

<sup>1</sup>Here we don't need to consider the influence of FWHMs, since the scans along the other two dimensions are quite relaxed with the current experimental setup.

$10^{-3}$  counts/s. The estimations are list in Table 6.1.

### **The XRMS Experiment Setup**

As is well known, the interaction between the electron spin and the electromagnetic field gives rise to magnetic scattering of X-rays. A magnetic contribution to the quasi-elastic scattering exists even in the paramagnetic state of materials, brought about by exchange interactions. The magnetic short-range order effect, however, is generally very weak and masked by the charge diffuse scattering which are always present. In order to disclose the details about the magnetic short-range order, it is necessary to use strictly monochromatic radiation and preferably single-crystal specimens. The possibility of observing the magnetic diffuse scattering by a properly designed experiment is now opened up by the last-generation high-brilliance synchrotron radiation sources, which provide almost completely polarized X-ray beams.

The feasibility of an X-ray scattering experiment aiming at measuring the magnetic contribution to the diffuse scattering was investigated and a possible experimental configuration was proposed. For this process, the polarization of incoming and scattered photons is either parallel or perpendicular to the scattering plane. Scattered photons can have a polarization perpendicular to that of the incoming ones only when processes other than Thomson scattering are present, such as magnetic resonant scattering. The diffuse character of such a contribution makes its experimental determination much more difficult since the collection of the scattered photons must take place over a relatively large solid angle, simultaneously maintaining a good rejection of the Thomson scattering brought about by atomic thermal motion.

The XRMS experiment was performed on the 6ID-B beamline in the MUCAT sector at the Advanced Photon Source at the Gd  $L_2$  absorption edge ( $E = 7.934$  keV). The incident radiation was linearly polarized perpendicular to the vertical scattering plane ( $\sigma$ -polarized) with a spatial cross-section of 1 mm (horizontal)  $\times$  0.2 mm (vertical). In this

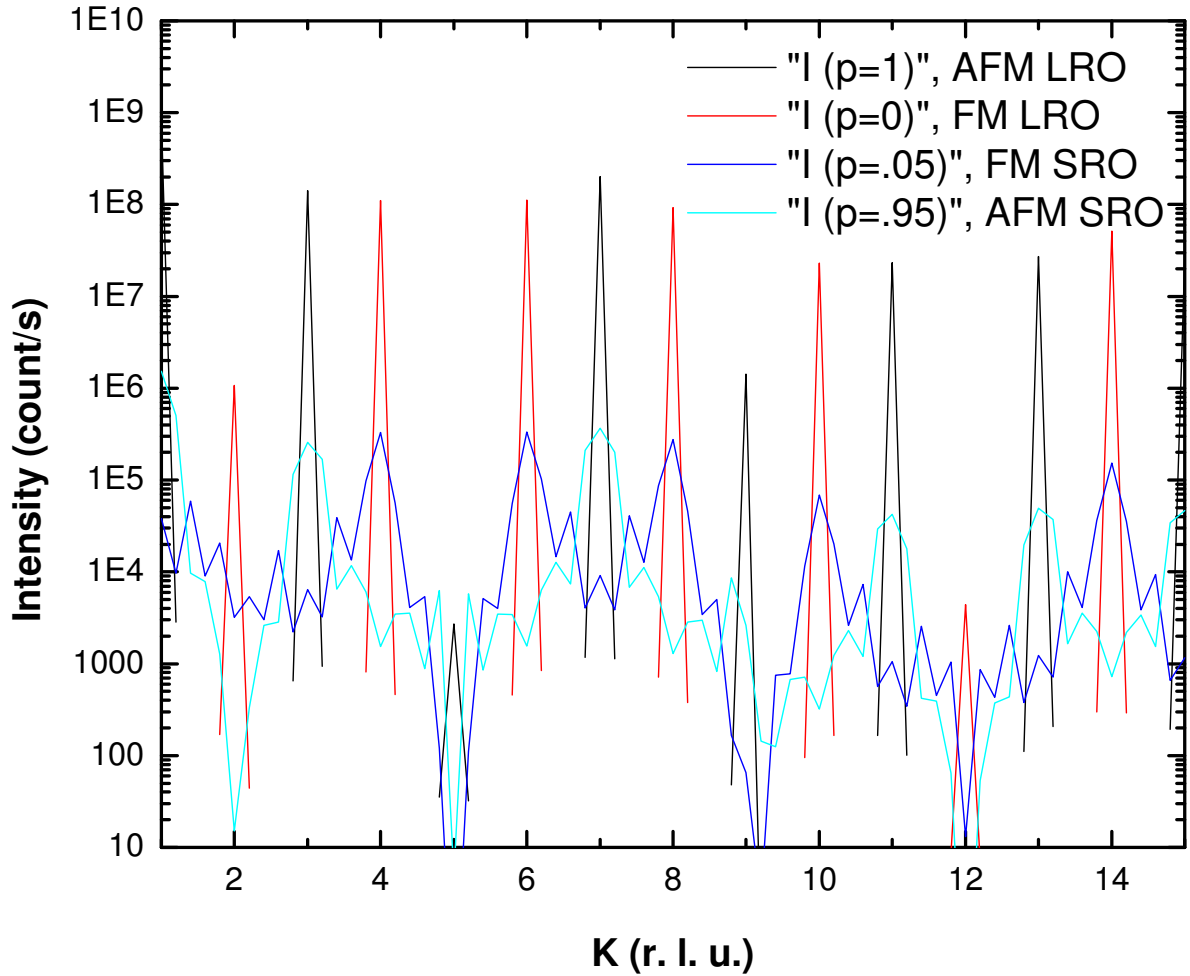


Figure 6.3 The intensity,  $I = f(q)^2$  v.s. the scattering vector,  $q = (0k0)$  generated from 400 layers stacking along  $\mathbf{b}$  axis based on the Hendricks-Teller partial order model [HT42]. The model is described in the text. The step size is  $k = 0.2$  for data point generation. The colors represent different probabilities:  $p = 1$  (black), 0 (red), 0.05 (blue), and 0.95 (light blue). AFM is antiferromagnetic. FM is ferromagnetic. LRO is long-range order. SRO is short-range order.

configuration, the resonant magnetic scattering arising from electric dipole transitions (E1, from the 2p-to-5d states) changes the plane of linear polarization into the scattering plane ( $\pi$ -polarization). In contrast, charge scattering does not change the polarization of the scattered photons ( $\sigma$ - $\sigma$  scattering). Pyrolytic graphite PG (0 0 6) was used as a polarization analyzer to suppress the charge background relative to the magnetic scattering signal. The mosaic spread of the analyzer is about  $0.5^\circ$ .

The  $\text{Gd}_5\text{Ge}_4$  sample was prepared with a polished surface perpendicular to the  $\mathbf{b}$  axis of approximately  $2 \times 2 \text{ mm}^2$ . The sample was mounted on the end of the cold-finger of a dispex cryogenic refrigerator with the crystallographic  $\mathbf{b}$ -axis parallel to the axis of the dispex and set in the scattering plane. This configuration allows the sample to be rotated around the scattering vector  $\mathbf{Q}$  (parallel to the  $\mathbf{b}$ -axis) while keeping  $Q$  constant.

## XRMS Results

If a significant magnetic diffuse scattering signal is detected at 130 K above  $T_N = 125 \text{ K}$ , a difference between the count rates at 130 K and at 240 K should be observed. At the latter temperature,  $\text{Gd}_5\text{Ge}_4$  is a paramagnet. Both transverse and longitudinal scans at 130 K and 240 K, respectively, show no significant difference. The PG (0 0 6) analyzer has a relatively large energy acceptance. It is possible that the weak magnetic diffuse signal is overwhelmed by fluorescence, which might be a dominant one over other possible backgrounds.

By making an appropriate choice of analyzer crystal, which is oriented to diffract the beam perpendicular to the scattering plane for the sample, the charge scattering background can be effectively suppressed by roughly a factor of  $\cos^2(2\theta_{\text{analyzer}})$  relative to the dipole resonant magnetic scattering. In order to get a better signal to background ratio, a different polarization analyzer was tested. A Ge(3 3 3) analyzer was chosen for this purpose since  $2\theta_{(333)} = 91.73^\circ$  is close to  $90^\circ$  for the Gd  $L_2$  edge. In addition, the relatively tight energy resolution of the Ge(3 3 3) analyzer, tuned for elastic scattering at

Table 6.2 Estimated intensity for magnetic short-range order using a Ge analyzer. We take  $p = 0.5$ .  $I_1^{\text{Max}}$  is the magnetic diffuse scattering intensity from the model with magnetic long-range order along two dimensions and short-range order along the other dimension.  $I_2^{\text{Max}}$  is the intensity from the model with magnetic long-range order along one dimension and short-range order along the other two dimensions.  $I_3^{\text{Max}}$  is the intensity from the model with short-range order along all three dimensions.

	$I_1^{\text{Max}}$	$I_2^{\text{Max}}$	$I_3^{\text{Max}}$
Estimated intensity (counts/s)	100	0.1	$10^{-4}$

$E = 7.934$  keV, does not pass the fluorescence radiation at lower energy, thereby reducing this contribution to the background. However, on the other hand, the tight resolution also narrows the angular acceptance for the magnetic diffuse and Bragg reflection signal. In order to estimate the intensity from measurements, we note here that the FWHM of the (3 3 3) Bragg diffraction from the Ge analyzer is about  $0.007^\circ$ , which is much smaller than the FWHMs of Bragg diffractions and the broad diffuse peak from the sample. Therefore, both the measured intensity of the (0 7 0) reflection at the Bragg condition and the measured diffuse intensity from the sample are determined by the FWHM of the rocking scans from the Ge analyzer. Both measured intensities are proportional to the integrated intensity from the characteristic of the Ge analyzer. Hence, the ratio of both measured intensities would be:

$$I_{p=0.5}^{\text{measure}}(\text{SRO})/I_{p=1}^{\text{measure}}(0\ 7\ 0) = \frac{I_{p=0.5}^{\text{Max}}(\text{SRO})}{I_{p=1}^{\text{Max}}(0\ 7\ 0)} = 10^{-3}$$

The intensity of (0 7 0) magnetic reflection is experimentally about  $10^5$  counts/s with the Ge analyzer. Therefore, the count rate should be about 100 counts/s for the magnetic short-range order model as described above. We can do a similar estimation of the intensity for the magnetic short-range order with different dimensionality as we did before. The estimations are list in Table 6.2.

In Fig. 6.4, the reciprocal K scan started from (0 2 -0.2) to (0 9 -0.2), which is

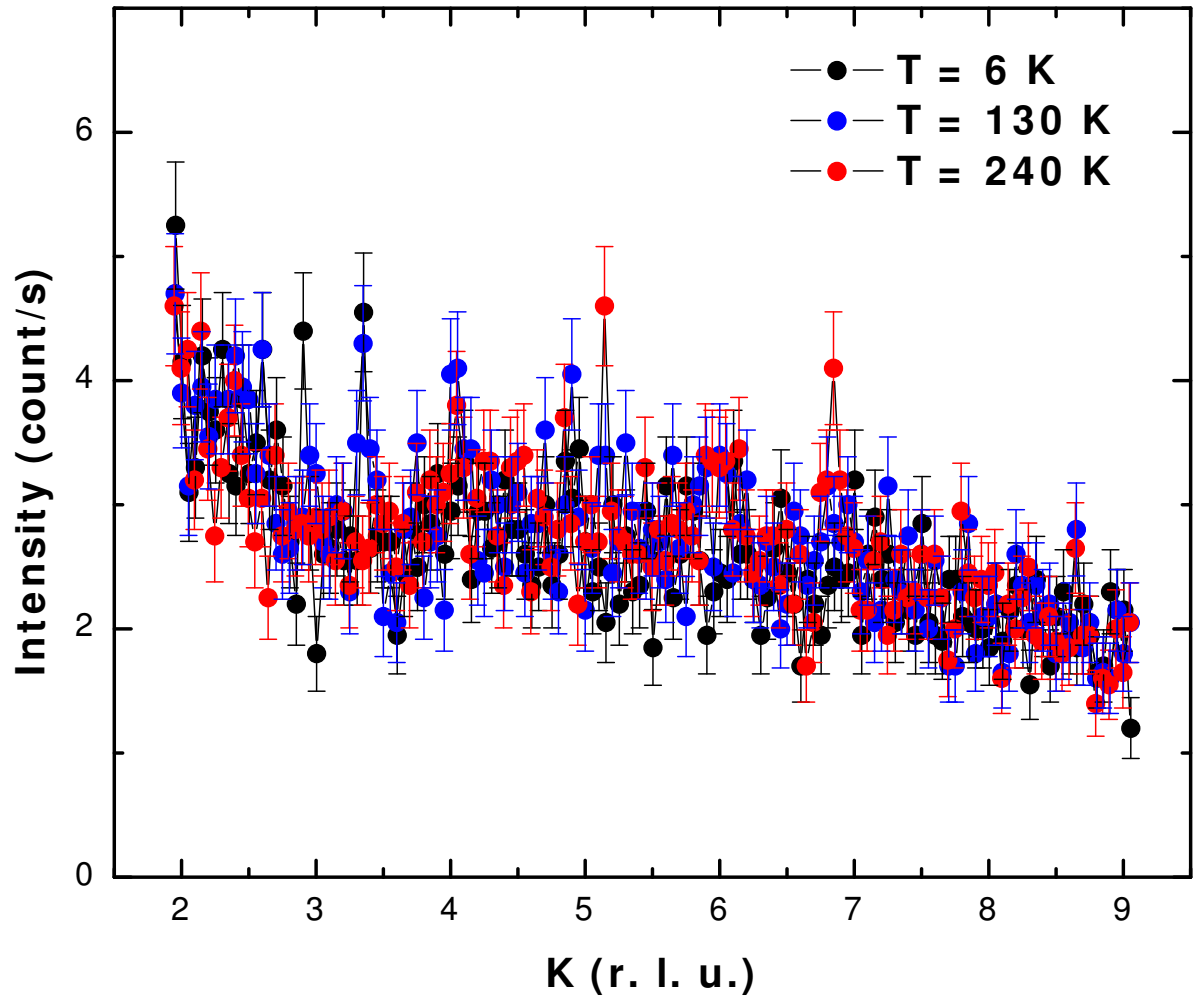


Figure 6.4 The longitudinal K scans, ( $0 \text{ K} - 0.2$ ), of  $\text{Gd}_5\text{Ge}_4$  at three different temperatures 6 K (black), 130 K (blue) and 240 K (red) using the analyzer  $\text{Ge}(3 \ 3 \ 3)$ . The counting time for each data point is 20 seconds.

far away from charge tails. The counting time is 20 seconds for each data point. No significant difference was found between 6 K, 130 K and 240 K with small mosaic analyzer Ge (3 3 3). In Fig. 6.5, the reciprocal L scan started from (0 7.35 -0.5) to (0 7.35 0.5). Again, there is no significant difference was found between 130 K and 240 K. The count rates of the background at temperatures above  $T_N$  are about 0.5 counts/s. The error bars for the count rates are about 0.15 counts/s, which is our sensitivity limit with a counting time of 20 seconds for the detection of a magnetic diffuse signal. The count rate for magnetic diffuse scattering then, is lower than 0.15 counts/s, if any. The reciprocal L scan started from (0 8.65 -0.5) to (0 8.65 0.5) was also performed. The results are shown in Fig. 6.6. No magnetic diffuse scattering signal was found in all measurements performed. Though no detailed information about the magnetic SRO can be concluded, the simple model with magnetic short-range order along **b**-axis and long-range order along **a** and **c** axes, which we proposed earlier for the magnetic SRO in  $\text{Gd}_5\text{Ge}_4$ , is excluded.

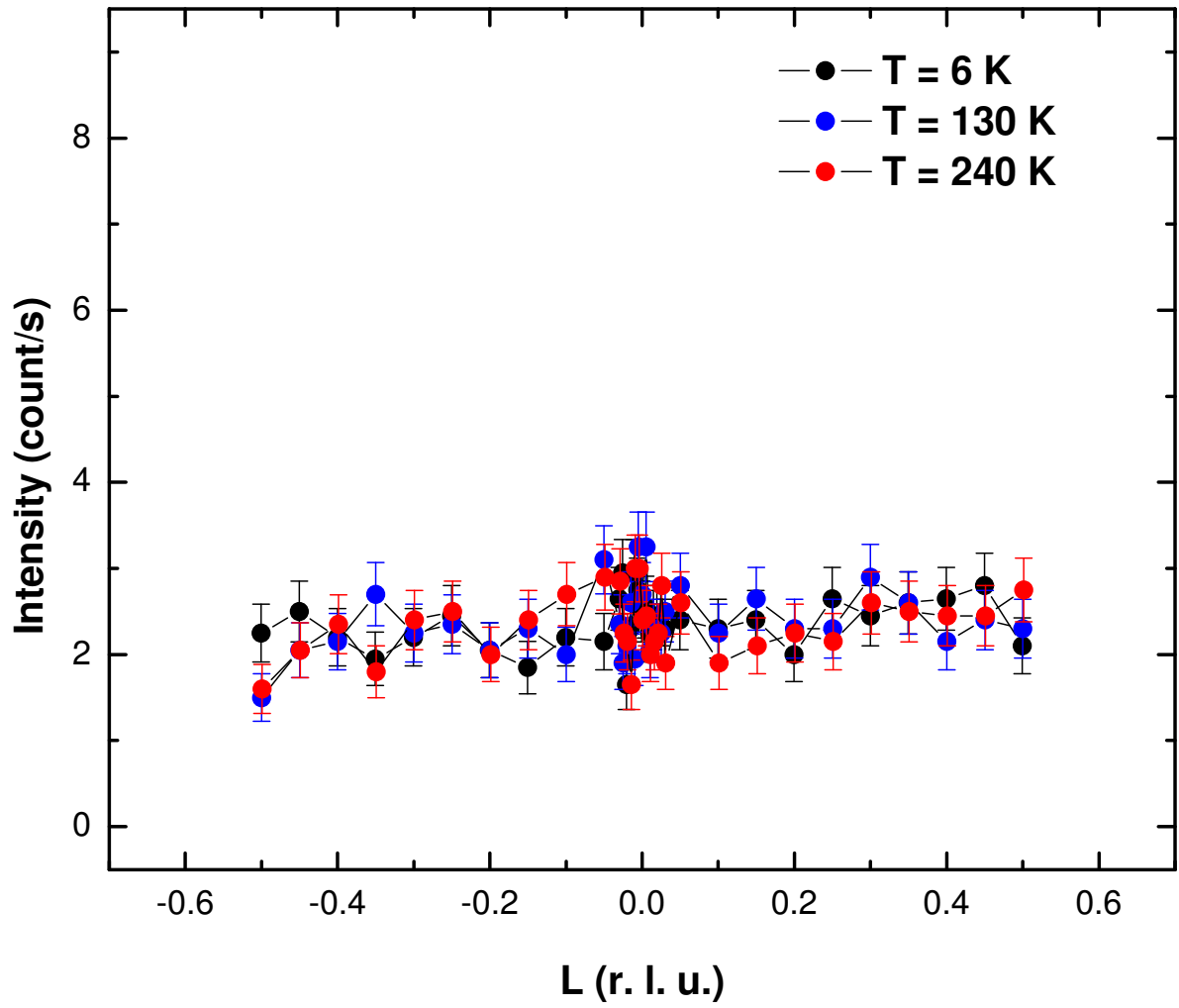


Figure 6.5 The transverse L scans,  $(0 \ 7.35 \ L)$ , of  $Gd_5Ge_4$  at three different temperatures 6 K (black), 130 K (blue) and 240 K (red) using analyzer  $Ge(3 \ 3 \ 3)$

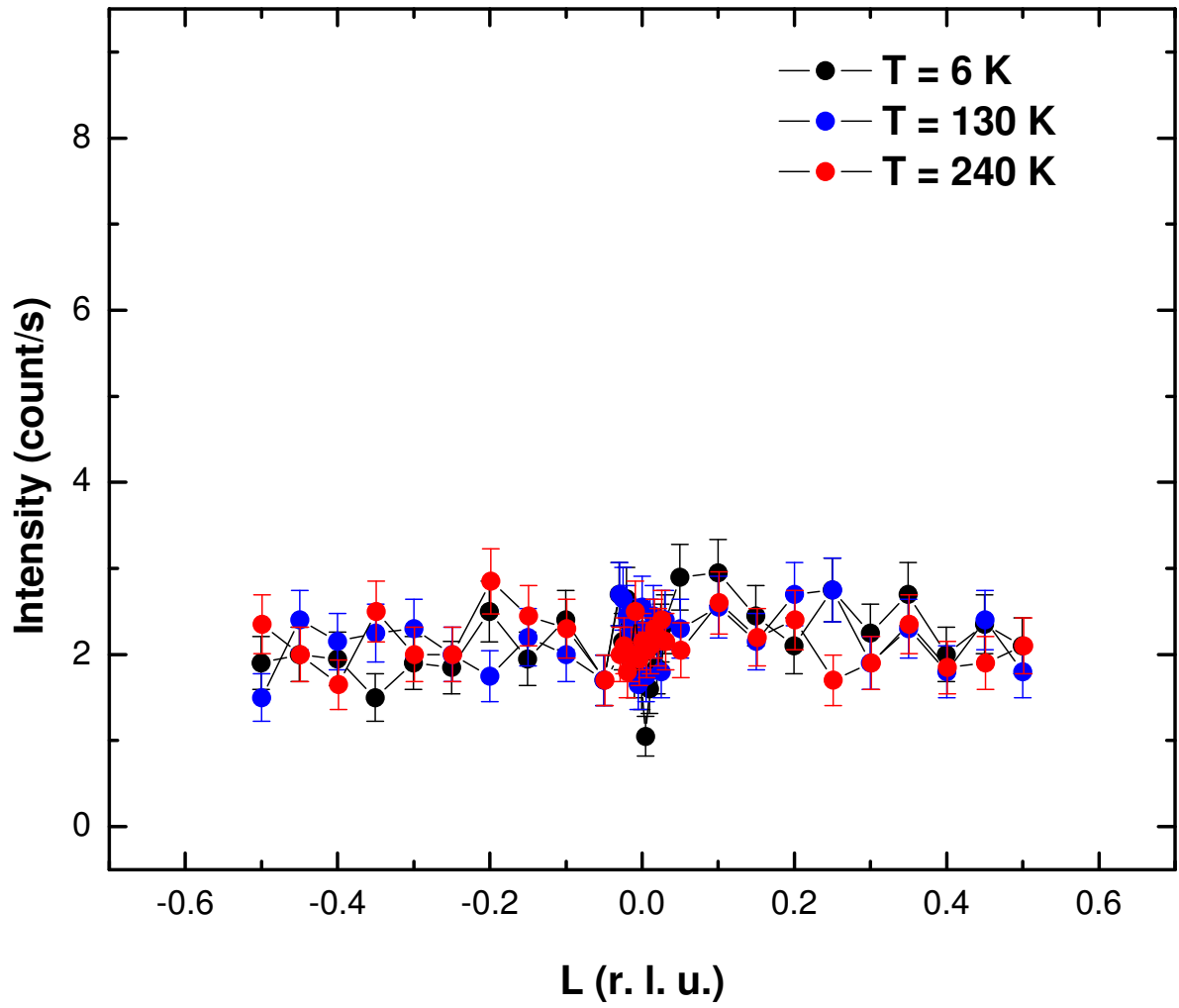


Figure 6.6 The transverse L scans,  $(0\ 8.65\ L)$ , of  $Gd_5Ge_4$  at three different temperatures 6 K (black), 130 K (blue) and 240 K (red) using analyzer  $Ge(3\ 3\ 3)$

## CHAPTER 7. Summary

The XRMS experiment on the  $\text{Gd}_5\text{Ge}_4$  system has shown that, below the Néel temperature,  $T_N = 127$  K, the magnetic unit cell is the same as the chemical unit cell. From azimuth scans and the  $\mathbf{Q}$  dependence of the magnetic scattering, all three Gd sites in the structure were determined to be in the same magnetic space group  $Pnm'a$ . The magnetic moments are aligned along the  $\mathbf{c}$ -axis and the  $\mathbf{c}$ -components of the magnetic moments at the three different sites are equal. The ferromagnetic slabs are stacked antiferromagnetically along the  $\mathbf{b}$ -direction.

We found an unusual order parameter curve in  $\text{Gd}_5\text{Ge}_4$ . A spin-reorientation transition is a possibility in  $\text{Gd}_5\text{Ge}_4$ , which is similar to the  $\text{Tb}_5\text{Ge}_4$  case.  $\text{Tb}_5\text{Ge}_4$  possesses the same  $\text{Sm}_5\text{Ge}_4$ -type crystallographic structure and the same magnetic space group as  $\text{Gd}_5\text{Ge}_4$  does. The difference in magnetic structure is that  $\text{Tb}_5\text{Ge}_4$  has a canted one but  $\text{Gd}_5\text{Ge}_4$  has nearly a collinear one in the low temperature antiferromagnetic phase. The competition between the magneto-crystalline anisotropy and the nearest-neighbor magnetic exchange interactions may allow a 3-dimensional canted antiferromagnetic structure in  $\text{Tb}_5\text{Ge}_4$ . The spin-reorientation transition in both  $\text{Gd}_5\text{Ge}_4$  and  $\text{Tb}_5\text{Ge}_4$  may arise from the competition between the magnetic anisotropy from the spin-orbit coupling of the conduction electrons and the dipolar interactions anisotropy.

The XRMS experiments on  $\text{Gd}_5\text{Ge}_4$  with external field applied have shown that the antiferromagnetically aligned moments at the three Gd sites flop from the  $\mathbf{c}$  axis to  $\mathbf{a}$  axis at  $T = 10$  K with a critical field,  $H_{\text{sf}} = 9$  kOe, along the  $\mathbf{c}$ -axis. The magnetic space group changes from  $Pnm'a$  to  $Pn'm'a'$  at all three sublattices. Both phases have

intraslab FM correlations and interslab AFM correlations. The magnetic correlation is unchanged in both phases below  $T_N = 125$  K. We conclude that this field induced transition is a pure spin-flop transition, since the antiferromagnetically ordered moments at the three Gd sites flop from the **c** direction to the **a** direction. A small ferromagnetic component along **c** axis is induced by the applied field at the transition. The metastable region where both phases coexist on the phase diagram, and the nucleation phenomena in the phase transition were found. No significant magnetostriction effects were observed at the spin-flop transition. Though  $\text{Gd}^{3+}$  ions have negligible single ion anisotropy, the easy plane anisotropy of the ordered state in  $\text{Gd}_5\text{Ge}_4$  originates from the dipolar interactions, with the SO coupling of the conduction electrons providing a weak orthorhombic anisotropy.

$\text{Gd}_5\text{Si}_{0.33}\text{Ge}_{3.67}$  changes from paramagnetic state to antiferromagnetic state at  $T_N = 127$  K and from antiferromagnetic state to ferromagnetic state at  $T_c = 66$  K in zero field on cooling. The magnetic structure of  $\text{Gd}_5\text{Si}_{0.33}\text{Ge}_{3.67}$  in the AFM phase is very similar to that of  $\text{Gd}_5\text{Ge}_4$ . The first order transition from AFM  $\rightarrow$  FM in doped Si compound, which is induced by temperature in zero field, is similar to that in  $\text{Gd}_5\text{Ge}_4$ , which is induced by an applied magnetic field of 18 kOe at  $T = 4.5$  K.[LGP02] In both cases, strong magneto-elastic coupling is present. The Gd rich slabs shift relative to one another in the **a** direction at the transition,[PG97c, PHGR03] breaking the Ge(Si) bonds that connect the slabs in the **b** direction with the concomitant destruction of FM ordering. The breaking of Ge(Si) bonds between the sheared slabs weakens the magnetic interslab coupling.[TPS<sup>+</sup>04] A large hybridization between Ge 4p orbitals and spin-polarized 5d orbitals on Gd leads to a small net magnetization on Ge and a long-range Ruderman-Kittel-Kasuya-Yosida (RKKY) indirect FM exchange coupling between 4f Gd moments in adjacent Gd slabs.[HLH<sup>+</sup>07] This coupling is significantly weakened when the slabs shear at the bond-breaking transition, resulting in destruction of FM order.

Studies of the magnetization of  $\text{Gd}_5\text{Ge}_4$  indicate that magnetic short-range order

(SRO) is retained above Néel temperature. However, our XRMS study could not find any significant evidence of SRO. The reason could be that the magnetic diffuse signal is below our sensitivity limit. Though no detailed information about the magnetic SRO can be concluded, the simple model with magnetic short-range order along **b**-axis and long-range order along **a** and **c** axes, which we proposed for the magnetic SRO in  $\text{Gd}_5\text{Ge}_4$ , is excluded.

## ACKNOWLEDGEMENTS

As the end of this thesis, I'd like to give words of gratitude to all those who helped to make this thesis possible. First of all, It is difficult to overstate my gratitude to my Ph.D. supervisor, Dr. Alan I. Goldman. With his enthusiasm, his inspiration, and his great efforts to explain things clearly and simply, I have developed my profile as an experimental physicist. I also have to express my great gratitude to my co-major advisor, Dr. Robert J. McQueeney. Throughout my thesis-writing period, he provided encouragement, sound advice, good teaching, good company, and lots of good ideas. I would also like to thank professor Bruce N. Harmon and Yongbin Lee for theoretical support and tons of fruitful discussions. I appreciate the contributions to this work from my committee members: Dr. Patricia A. Thiel and Dr. Soeren A. Prell. I would like to thank Jong-woo Kim and Brad Sieve for helping me getting used to x-ray laboratory. I also would like to Shibabrata Nandi for collaboration in experiments. I am deeply indebted to Andreas Kreyssig for stimulating me to improve my thinking of physics and guiding me toward a better way to do the experiment.

Finally, I am very grateful for my wife for taking care of the whole family when I was out of town for experiments and always being there but never asking why it was taking so long. My love and gratefulness are also giving to my father, mother, two daughters and all my family members, who gave me the felicity in the life.

**BIBLIOGRAPHY**

- [And72] P. W. Anderson. More Is Different. *Science*, 177(4047):393–396, 1972.
- [BA75] Alastair D. Bruce and Amnon Aharony. Coupled order parameters, symmetry-breaking irrelevant scaling fields, and tetracritical points. *Phys. Rev. B*, 11(1):478–499, Jan 1975.
- [Ber68] E. F. Bertaut. Representation analysis of magnetic structures. *Acta Cryst. A*, 24:217–231, Jan 1968.
- [Blu85] M. Blume. Magnetic scattering of x rays (invited). *J. Appl. Phys.*, 57(8):3615–3618, 1985.
- [BSM<sup>+</sup>01] P. Blaha, K. Schwarz, G. K. H. Madsen, D. Kvasnicka, and J. Luitz. *in WIEN2k, An Augmented Plane Wave + Local Orbitals Program for Calculating Crystal Properties*. edited by K. Schwarz, TU Wien, Austria, 2001.
- [BZR07] A. N. Bogdanov, A. V. Zhuravlev, and U. K. Rößler. Spin-flop transition in uniaxial antiferromagnets: Magnetic phases, reorientation effects, and multidomain states. *Phys. Rev. B*, 75(9):094425, 2007.
- [CALB05] F. Casanova, A. Labarta, and X. Batlle. Giant heat dissipation at the low-temperature reversible-irreversible transition in Gd<sub>5</sub>Ge<sub>4</sub>. *Phys. Rev. B*, 72:172402, 2005.

- [Cha84] Shih-Lin Chang. *Multiple Diffraction of X-Rays in Crystals*. Springer-Verlag, 1984.
- [CL00] P. M. Chaikin and T. C. Lubensky. *Principles of Condensed Matter Physics*. Cambridge University Press, 1st edition, October 2000.
- [CLB<sup>+</sup>04] F. Casanova, A. Labarta, X. Batlle, J. Marcos, L. Maosa, A. Planes, and S. deBrion. Effect of a magnetic field on the magnetostructural phase transition in  $Gd_5(Ge_{1-x}Si_x)_4$ . *Phys. Rev. B*, 69:104416, 2004.
- [CPP<sup>+</sup>00] W. Choe, V. K. Pecharsky, A. O. Pecharsky, K. A. Gschneidner, V. G. Young, and G. J. Miller. Making and Breaking Covalent Bonds across the Magnetic Transition in the Giant Magnetocaloric Material  $Gd_5(Si_2Ge_2)$ . *Phys. Rev. Lett.*, 84(20):4617–4620, May 2000.
- [CTBE<sup>+</sup>05] Massimiliano Colarieti-Tosti, Till Burkert, Olle Eriksson, Lars Nordstrom, and Michael S. S. Brooks. Theory of the temperature dependence of the easy axis of magnetization in hcp Gd. *Phys. Rev. B*, 72:094423, 2005.
- [CTSA<sup>+</sup>03] M. Colarieti-Tosti, S. I. Simak, R. Ahuja, L. Nordström, O. Eriksson, D. Åberg, S. Edvardsson, and M. S. S. Brooks. Origin of Magnetic Anisotropy of Gd Metal. *Phys. Rev. Lett.*, 91(15):157201, 2003.
- [dB72] F. de Bergevin and M. Brunel. Observation of magnetic superlattice peaks by X-ray diffraction on an antiferromagnetic NiO crystal. *Phys. Lett. A*, 39:141–142, April 1972.
- [DIG<sup>+</sup>97] C. Detlefs, A. H. M. Z. Islam, A. I. Goldman, C. Stassis, P. C. Canfield, J. P. Hill, and D. Gibbs. Determination of magnetic-moment directions

- using x-ray resonant exchange scattering . *Phys. Rev. B*, 55(2):R680–R683, Jan 1997.
- [EZO<sup>+</sup>91] J. M. Elbicki, L. Y. Zhang, R. T. Obermyer, W. E. Wallace, and S. G. Sankar. Magnetic studies of  $(Gd_{1-x}M_x)_5Si_4$  alloys (M=La or Y). volume 69, pages 5571–5573. AIP, 1991.
- [FDG87] N. M. Fujiki, K. De’Bell, and D. J. W. Geldart. Lattice sums for dipolar systems. *Phys. Rev. B*, 36(16):8512–8516, Dec 1987.
- [FH91] W. Fulton and J. Harris. *Representation Theory: A First Course*. Springer, 1991.
- [FN74] Michael E. Fisher and David R. Nelson. Spin Flop, Supersolids, and Bicritical and Tetracritical Points. *Phys. Rev. Lett.*, 32(24):1350–1353, Jun 1974.
- [FSS92] K. D. Finkelstein, Qun Shen, and S. Shastri. Resonant x-ray diffraction near the iron K edge in hematite ( $\alpha\text{-Fe}_2\text{O}_3$ ). *Phys. Rev. Lett.*, 69(10):1612–1615, Sep 1992.
- [GGH<sup>+</sup>91] Doon Gibbs, G. Grübel, D. R. Harshman, E. D. Isaacs, D. B. McWhan, D. Mills, and C. Vettier. Polarization and resonance studies of x-ray magnetic scattering in holmium. *Phys. Rev. B*, 43(7):5663–5681, Mar 1991.
- [GHFD89] D. J. W. Geldart, P. Hargraves, N. M. Fujiki, and R. A. Dunlap. Anisotropy of the critical magnetic susceptibility of gadolinium. *Phys. Rev. Lett.*, 62(23):2728–2731, Jun 1989.

- [GHI<sup>+</sup>88] Doon Gibbs, D. R. Harshman, E. D. Isaacs, D. B. McWhan, D. Mills, and C. Vettier. Polarization and Resonance Properties of Magnetic X-Ray Scattering in Holmium. *Phys. Rev. Lett.*, 61:1241, 1988.
- [GKG<sup>+</sup>05] W. Good, J. Kim, A. I. Goldman, D. Wermeille, P. C. Canfield, C. Cunningham, Z. Islam, J. C. Lang, G. Srajer, and I. R. Fisher. Magnetic structure of  $\text{GdCo}_2\text{Ge}_2$ . *Phys. Rev. B*, 71(22):224427, 2005.
- [Gri69] Robert B. Griffiths. Nonanalytic Behavior Above the Critical Point in a Random Ising Ferromagnet. *Phys. Rev. Lett.*, 23(1):17–19, Jul 1969.
- [HGM67] F. Holtzberg, R. J. Gambino, and T. R. McGuire. New ferromagnetic 5 : 4 compounds in the rare earth silicon and germanium systems. *J. Phys. Chem. Solids.*, 28:2283–2289, November 1967.
- [HJS<sup>+</sup>04] M. Han, D. C. Jiles, J. E. Snyder, T. A. Lograsso, and D. L. Schlagel. Giant magnetostriction behavior at the Curie temperature of single crystal  $\text{Gd}_5(\text{Si}_{0.5}\text{Ge}_{0.5})_4$ . *J. Appl. Phys.*, 95(11):6945–6947, 2004.
- [HLH<sup>+</sup>07] D. Haskel, Y. B. Lee, B. N. Harmon, Z. Islam, J. C. Lang, G. Srajer, Ya. Mudryk, Jr. Gschneidner, and V. K. Pecharsky. Role of Ge in Bridging Ferromagnetism in the Giant Magnetocaloric  $\text{Gd}_5(\text{Ge}_{1-x}\text{Si}_x)_4$  Alloys. *Phys. Rev. Lett.*, 98:247205, June 2007.
- [HM96] J. P. Hill and D. F. McMorrow. X-ray resonant exchange scattering: Polarization dependence and correlation function. *Acta Cryst. A*, 52(2):236, 1996.
- [HMC<sup>+</sup>04] V. Hardy, S. Majumdar, S. J. Crowe, M. R. Lees, D. McK. Paul, L. Hervé, A. Maignan, S. Hbert, C. Martin, C. Yaicle, M. Hervieu, and B. Raveau.

Field induced magnetization steps in intermetallic compounds and manganese oxides: A martensitic scenario. *Phys. Rev. B*, 69:020407/1–020407/4, 2004.

- [HPS<sup>+</sup>02] M. Han, J. Paulsen, J. E. Snyder, D. C. Jiles, T. A. Lograsso, and D. L. Schlagel. Thermal expansion of single-crystal  $\text{Gd}_5\text{Ge}_{1.95}\text{Si}_{2.05}$  showing unusual first-order transformation. *IEEE Transactions on Magnetism*, 38:3252–3254, 2002.
- [HT42] Sterling Hendricks and Edward Teller. X-ray interference in partially ordered layer lattices. *The Journal of Chemical Physics*, 10(3):147–167, 1942.
- [HTBG88] J. P. Hannon, G. T. Trammell, M. Blume, and Doon Gibbs. X-Ray Resonance Exchange Scattering. *Phys. Rev. Lett.*, 61(10):1245–1248, Sep 1988.
- [JM91] J. Jensen and A. R. Mackintosh. *Rare Earth Magnetism*. Clarendon Press, Oxford, 1991.
- [KH77] D D Koelling and B N Harmon. A technique for relativistic spin-polarised calculations. *J. Phys. C: Solid State Phys.*, 10(16):3107–3114, 1977.
- [KNF76] J. M. Kosterlitz, David R. Nelson, and Michael E. Fisher. Bicritical and tetracritical points in anisotropic antiferromagnetic systems. *Phys. Rev. B*, 13(1):412–432, Jan 1976.
- [KPD04] A. Yu. Kozlov, V. V. Pavlyuk, and V. M. Davydov. The crystal structure of the new ternary compounds  $\text{RE}_5\text{Sb}_2\text{X}_2$  (RE–Y, Tb, Dy, Ho, Er, Tm; X–Si or Ge). *Intermetallics*, 12:151–155, February 2004.

- [KS00] S. N. Kaul and S. Srinath. Gadolinium: A helical antiferromagnet or a collinear ferromagnet. *Phys. Rev. B*, 62(2):1114–1117, Jul 2000.
- [LC96] S. W. Lovesey and S. P. Collins. *X-ray Scattering and Absorption by Magnetic Materials*. Oxford University Press, 1996.
- [LGL<sup>+</sup>04] E. M. Levin, K. A. Gschneidner, Jr., T. A. Lograsso, D. L. Schlager, and V. K. Pecharsky. Reversible spin-flop and irreversible metamagnetic transitions induced by magnetic field in the layered  $Gd_5Ge_4$  antiferromagnet. *Phys. Rev. B*, 69:144428, 2004.
- [LGP02] E. M. Levin, K. A. Gschneidner, Jr., and V. K. Pecharsky. Magnetic correlations induced by magnetic field and temperature in  $Gd_5Ge_4$ . *Phys. Rev. B*, 65(21):214427, Jun 2002.
- [LLP80] L. D. Landau, E. M. Lifshitz, and L. P. Pitaevskii. *Statistical Physics*. Butterworth-Heinemann, 1980.
- [LPG99] E. M. Levin, V. K. Pecharsky, and K. A. Gschneidner, Jr. Magnetic-field and temperature dependencies of the electrical resistance near the magnetic and crystallographic first-order phase transition of  $Gd_5(Si_2Ge_2)$ . *Phys. Rev. B*, 60(11):7993–7997, Sep 1999.
- [LPG00] E. M. Levin, V. K. Pecharsky, and K. A. Gschneidner. Unusual magnetic behavior in  $Gd_5(Si_{1.5}Ge_{2.5})$  and  $Gd_5(Si_2Ge_2)$ . *Phys. Rev. B*, 62(22):R14625–R14628, Dec 2000.
- [LPG01] E. M. Levin, V. K. Pecharsky, and K. A. Gschneidner, Jr. Spontaneous generation of voltage in  $Gd_5(Si_xGe_{1-x})_4$  during a first-order phase transition induced by temperature or magnetic field. *Phys. Rev. B*, 63:174110/1–174110/7, 2001.

- [LPGM01] E. M. Levin, V. K. Pecharsky, K. A. Gschneidner, Jr., and G. J. Miller. Electrical resistivity and electronic heat capacity and electronic structure of  $\text{Gd}_5\text{Ge}_4$ . *Phys. Rev. B*, 64(23):235103, Nov 2001.
- [LPGT00] E. M. Levin, V. K. Pecharsky, K. A. Gschneidner, Jr., and P. Tomlinson. Magnetic field and temperature-induced first-order transition in  $\text{Gd}_5(\text{Si}_{0.5}\text{Ge}_{1.5})$ : a study of the electrical resistance behavior. *J. Magn. Magn. Mater.*, 210:181–188, February 2000.
- [LR02] A. Lindbaum and M. Rotter. Spontaneous Magnetoelastic Effects in Gadolinium Compounds. In K. H. J. Buschow, editor, *Handbook of Magnetic Materials*, volume 14, chapter 4, page 307. Elsevier Science, New York, 2002.
- [MAI<sup>+</sup>98] L. Morellon, P. A. Algarabel, M. R. Ibarra, J. Blasco, B. García-Landa, Z. Arnold, and F. Albertini. Magnetic-field-induced structural phase transition in  $\text{Gd}_5(\text{Si}_{1.8}\text{Ge}_{2.2})$ . *Phys. Rev. B*, 58(22):R14721–R14724, Dec 1998.
- [MAM<sup>+</sup>03] C. Magen, Z. Arnold, L. Morellon, Y. Skorokhod, P. A. Algarabel, M. R. Ibarra, and J. Kamarad. Pressure-Induced three-dimensional ferromagnetic correlations in the giant magnetocaloric compound  $\text{Gd}_5\text{Ge}_4$ . *Phys. Rev. Lett.*, 91:207202/1–207202/4, 2003.
- [MAM<sup>+</sup>06] C. Magen, P. A. Algarabel, L. Morellon, J. P. Araujo, C. Ritter, M. R. Ibarra, A. M. Pereira, and J. B. Sousa. Observation of a Griffiths-like Phase in the Magnetocaloric Compound  $\text{Tb}_5\text{Si}_2\text{Ge}_2$ . *Phys. Rev. Lett.*, 96:167201, April 2006.

- [MAMI01] L. Morellon, P. A. Algarabel, C. Magen, and M. R. Ibarra. Giant magnetoresistance in the Ge-rich magnetocaloric compound,  $\text{Gd}_5(\text{Si}_{0.1}\text{Ge}_{0.9})_4$ . *J. Magn. Magn. Mater.*, 237:119–123, December 2001.
- [Mar88] G. Margaritondo. *Introduction to Synchrotron Radiation*. New York: Oxford University Press, 1988.
- [MBAI00] L. Morellon, J. Blasco, P. A. Algarabel, and M. R. Ibarra. Nature of the first-order antiferromagnetic-ferromagnetic transition in the Ge-rich magnetocaloric compounds  $\text{Gd}_5(\text{Ge}_{1-x}\text{Si}_x)_4$ . *Phys. Rev. B*, 62:1022, 2000.
- [MHKAGP05] Ya. Mudryk, A. P. Holm, Jr. K. A. Gschneidner, and V. K. Pecharsky. Crystal structure-magnetic property relationships of  $\text{Gd}_5\text{Ge}_4$  examined by in situ x-ray powder diffraction. *Phys. Rev. B*, 72(6):064442, 2005.
- [Mil06] G. J. Miller. Complex rare-earth tetrelides  $\text{RE}_5(\text{Ge}_{1-x}\text{Si}_x)_4$ : New materials for magnetic refrigeration and superb playground for solid state chemistry. *Chem. Soc. Rev.*, 35:799–813, 2006.
- [MM06] Sumohan Misra and Gordon J. Miller. On the distribution of tetrelide atoms (Si, Ge) in  $\text{Gd}_5(\text{Si}_x\text{Ge}_{1-x})_4$ . *J. Solid State Chem.*, 179:2290–2297, August 2006.
- [MMA<sup>+</sup>03] C. Magen, L. Morellon, P. A. Algarabel, C. Marquina, and M. R. Ibarra. Magnetoelastic behavior of  $\text{Gd}_5\text{Ge}_4$ . *J. Phys.: Condens. Matter*, 15:2389–2397, 2003.
- [MSG<sup>+</sup>L<sup>+</sup>98] L. Morellon, J. Stankiewicz, B. García-Landa, P. A. Algarabel, and M. R. Ibarra. Giant magnetoresistance near the magnetostructural transition in  $\text{Gd}_5(\text{Si}_{1.8}\text{Ge}_{2.2})$ . *Appl. Phys. Lett.*, 73(23):3462–3464, 1998.

- [MVI<sup>+</sup>90] D. B. McWhan, C. Vettier, E. D. Isaacs, G. E. Ice, D. P. Siddons, J. B. Hastings, C. Peters, and O. Vogt. Magnetic x-ray-scattering study of uranium arsenide. *Phys. Rev. B*, 42(10):6007–6017, Oct 1990.
- [N36] L. Néel. Magnetic properties of the metallic state and energy of interaction between magnetic atoms. *Annales de Physique*, 5:232, 1936.
- [NdVZ<sup>+</sup>03] M. Nazih, A. de Visser, L. Zhang, O. Tegus, and E. Brck. Thermal expansion of the magnetorefrigerant  $Gd_5(Si,Ge)_4$ . *Solid State Communications*, 126:255–259, 2003.
- [OG65] W. Opechowski and R. Guccione. Magnetic symmetry. *Magnetism (GT Rado and H. Shull, eds.)*, 2, 1965.
- [OPG<sup>+</sup>06] Z. W. Ouyang, V. K. Pecharsky, K. A. Gschneidner, Jr., D. L. Schlagel, and T. A. Lograsso. Magnetic anisotropy and magnetic phase diagram of  $Gd_5Ge_4$ . *Phys. Rev. B.*, 74(2):024401, 2006.
- [OPKAG<sup>+</sup>06] Z. W. Ouyang, V. K. Pecharsky, Jr. K. A. Gschneidner, D. L. Schlagel, and T. A. Lograsso. Short-range anisotropic ferromagnetic correlations in the paramagnetic and antiferromagnetic phases of  $Gd_5Ge_4$ . *Phys. Rev. B*, 74(9):094404, 2006.
- [PG] V. K. Pecharsky and K. A. Gschneidner, Jr. Structure, magnetism and thermodynamics of the novel rare earth based  $R_5T_4$  intermetallics. unpublished.
- [PG97a] V. K. Pecharsky and K. A. Gschneidner, Jr. Effect of Alloying on the Giant Magnetocaloric Effect of  $Gd_5Si_2Ge_2$ . *J. Magn. Magn. Mater.*, 167:L179 – L184, 1997.

- [PG97b] V. K. Pecharsky and K. A. Gschneidner, Jr. Giant Magnetocaloric Effect in  $\text{Gd}_5\text{Si}_2\text{Ge}_2$ . *Phys. Rev. Lett.*, 78:4494–4497, 1997.
- [PG97c] V. K. Pecharsky and K. A. Gschneidner, Jr. Phase relationships and crystallography in the pseudobinary system  $\text{Gd}_5\text{Si}_4\text{-Gd}_5\text{Ge}_4$ . *J. Alloys Compd.*, 260(1):98–106, 1997.
- [PG97d] V. K. Pecharsky and K. A. Gschneidner, Jr. Tunable Magnetic Regenerator Alloys with a Giant Magnetocaloric Effect for Magnetic Refrigeration from 20 K to 290 K. *Appl. Phys. Lett.*, 70:3299–3301, 1997.
- [PG98] V. K. Pecharsky and K. A. Gschneidner, Jr. The Giant Magnetocaloric Effect in  $\text{Gd}_5(\text{Ge}_{1-x}\text{Si}_x)_4$  Materials for Magnetic Refrigeration. *Advances in Cryogenic Engineering*, 43:1729–1736, 1998.
- [PHGR03] V. K. Pecharsky, A. P. Holm, K. A. Gschneidner, Jr., and R. Rink. Massive Magnetic-Field-Induced Structural Transformation in  $\text{Gd}_5\text{Ge}_4$  and the Nature of the Giant Magnetocaloric Effect. *Phys. Rev. Lett.*, 91(19):197204, Nov 2003.
- [PPGH07] Durga Paudyal, V. K. Pecharsky, K. A. Gschneidner, Jr., and B. N. Harmon. Magnetism of  $\text{Gd}_5\text{Ge}_4$  from first principles. *Phys. Rev. B*, 75(9):094427, 2007.
- [PSA<sup>+</sup>03] V. K. Pecharsky, G. D. Samolyuk, V. P. Antropov, A. O. Pecharsky, and K. A. Gschneidner. The effect of varying the crystal structure on the magnetism, electronic structure and thermodynamics in the  $\text{Gd}_5(\text{Si}_x\text{Ge}_{1-x})_4$ . *J. Solid State Chem.*, 171:57–68, February 2003.

- [PW92] John P. Perdew and Yue Wang. Accurate and simple analytic representation of the electron-gas correlation energy. *Phys. Rev. B*, 45(23):13244–13249, Jun 1992.
- [RCC<sup>+</sup>06] S. B. Roy, M. K. Chattopadhyay, P. Chaddah, J. D. Moore, G. K. Perkins, L. F. Cohen, Jr. K. A. Gschneidner, and V. K. Pecharsky. Evidence of a magnetic glass state in the magnetocaloric material  $\text{Gd}_5\text{Ge}_4$ . *Physical Review B (Condensed Matter and Materials Physics)*, 74(1):012403, 2006.
- [RLD<sup>+</sup>03] M. Rotter, M. Loewenhaupt, M. Doerr, A. Lindbaum, H. Sassik, K. Ziebeck, and B. Beuneu. Dipole interaction and magnetic anisotropy in gadolinium compounds. *Phys. Rev. B*, 68(14):144418, Oct 2003.
- [RMA<sup>+</sup>02] C. Ritter, L. Morellon, P. A. Algarabel, C. Magen, and M. R. Ibarra. Magnetic and structural phase diagram of  $\text{Tb}_5(\text{Si}_x\text{Ge}_{1-x})_4$ . *Phys. Rev. B*, 65(9):094405, Feb 2002.
- [SBC<sup>+</sup>02] J. B. Sousa, M. E. Braga, F. C. Correia, F. Carpinteiro, L. Morellon, P. A. Algarabel, and M. R. Ibarra. Thermopower behavior in the  $\text{Gd}_5(\text{Si}_{0.1}\text{Ge}_{0.9})_4$  magnetocaloric compound from 4 to 300 K. *J. Appl. Phys.*, 91:4457–4460, 2002.
- [SBC<sup>+</sup>03] J. B. Sousa, M. E. Braga, F. C. Correia, F. Carpinteiro, L. Morellon, P. A. Algarabel, and M. R. Ibarra. Anomalous behavior of the electrical resistivity in the giant magnetocaloric compound  $\text{Gd}_5(\text{Si}_{0.1}\text{Ge}_{0.9})_4$ . *Phys. Rev. B*, 67:134416, 2003.
- [She04] Sergey Sheludko. Polarization factors in the symmetrical case of three-wave diffraction. *Acta Crystallographica Section A*, 60(3):281–282, May 2004.

- [She05] Sergey Sheludko. Polarization factors in the general case of three-wave diffraction. *Acta Crystallographica Section A*, 61(5):528–530, Sep 2005.
- [SJ89] George H. Stout and Lyle H. Jensen. *X-Ray Structure Determination: A Practical Guide, 2nd Edition*. Wiley-Interscience, 2 edition, April 1989.
- [SJT67] G. S. Smith, Q. Johnson, and A. G. Tharp. Crystal structure of  $Sm_5Ge_4$ . *Acta Cryst.*, 22:269–272, 1967.
- [SLP99] A. B. Shick, A. I. Liechtenstein, and W. E. Pickett. Implementation of the LDA+U method using the full-potential linearized augmented plane-wave basis. *Phys. Rev. B*, 60(15):10763–10769, Oct 1999.
- [SLPS05] D. L. Schlagel, T. A. Lograsso, A. O. Pecharsky, and J. A. Sampaio. Crystal growth of re-si-ge magnetocaloric materials. In H. Kvande, editor, *Light Metals 2005*, page 1177. The Minerals, Metals and Materials Society, TMS, Warrendale, PA, 2005.
- [SMAI00] J. Stankiewicz, L. Morellon, P. A. Algarabel, and M. R. Ibarra. Hall effect in  $Gd_5Si_{1.8}Ge_{2.2}$ . *Phys. Rev. B*, 61:12651–12653, 2000.
- [SP78] Penelope Schobinger-Papamantellos. On the magnetic structure and magnetic phase transitions of  $Tb_5Ge_4$ . A Neutron diffraction study. *J. Phys. Chem. Solids.*, 39:197–205, 1978.
- [SS99] J. Szade and G. Skorek. Electronic structure and magnetism of  $Gd_5(Si,Ge)_4$  compounds. *J. Magn. Magn. Mater.*, 196-197:699–700, 1999.
- [STJ66] G. S. Smith, A. G. Tharp, and Q. Johnson. Crystallographic data on new rare earth – germanium and silicon compounds. *Nature (London)*, 210:1148–1149, 1966.

- [STJ67] G. S. Smith, A. G. Tharp, and Q. Johnson. Rare earth-germanium and -silicon compounds at 5:4 and 5:3 compositions. *Acta Cryst.*, 22:940–943, 1967.
- [SW72] H. Eugene Stanley and Victor K. Wong. Introduction to Phase Transitions and Critical Phenomena. *American Journal of Physics*, 40(6):927–928, 1972.
- [TBBdB02] O. Tegus, E. Bruck, K. H. J. Buschow, and F. R. de Boer. Transition-metal-based magnetic refrigerants for room-temperature applications. *Nature*, 415:150–152, 2002.
- [THH<sup>+</sup>94] T. R. Thurston, G. Helgesen, J. P. Hill, Doon Gibbs, B. D. Gaulin, and P. J. Simpson. X-ray- and neutron-scattering measurements of two length scales in the magnetic critical fluctuations of holmium. *Phys. Rev. B*, 49:15730, June 1994.
- [TJEW95] J. Trygg, B. Johansson, O. Eriksson, and J. M. Wills. Total Energy Calculation of the Magnetocrystalline Anisotropy Energy in the Ferromagnetic 3d Metals. *Phys. Rev. Lett.*, 75(15):2871–2874, Oct 1995.
- [TKK<sup>+</sup>05] L. Tan, A. Kreyssig, J. W. Kim, A. I. Goldman, R. J. McQueeney, D. Wermeille, B. Sieve, T. A. Lograsso, D. L. Schlagel, S. L. Budko, V. K. Pecharsky, and K. A. Gschneidner, Jr. Magnetic structure of Gd<sub>5</sub>Ge<sub>4</sub>. *Phys. Rev. B*, 71:214408, June 2005.
- [TPGP04] H. Tang, V. K. Pecharsky, K. A. Gschneidner, Jr., and A. O. Pecharsky. Interplay between reversible and irreversible magnetic phase transitions in polycrystalline Gd<sub>5</sub>Ge<sub>4</sub>. *Phys. Rev. B*, 69:064410, 2004.

- [TPS<sup>+</sup>04] H. Tang, V. K. Pecharsky, G. D. Samolyuk, M. Zou, K. A. Gschneidner, Jr., V. P. Antropov, D. L. Schlagel, and T. A. Lograsso. Anisotropic giant magnetoresistance in  $\text{Gd}_5\text{Ge}_2\text{Si}_2$ . *Phys. Rev. Lett.*, 93:237203/1–237203/1, 2004.
- [TSL<sup>+</sup>92] C. C. Tang, W. G. Stirling, G. H. Lander, Doon Gibbs, W. Herzog, Paolo Carra, B. T. Thole, K. Mattenberger, and O. Vogt. Resonant magnetic x-ray scattering in a series of uranium compounds. *Phys. Rev. B*, 46(9):5287–5297, Sep 1992.
- [TSP00] Luc Thomas, Mahesh G. Samant, and Stuart S. P. Parkin. Domain-Wall Induced Coupling between Ferromagnetic Layers. *Phys. Rev. Lett.*, 84(8):1816–1819, Feb 2000.
- [TT94] David H. Templeton and Lieselotte K. Templeton. Tetrahedral anisotropy of x-ray anomalous scattering. *Phys. Rev. B*, 49(21):14850–14853, Jun 1994.